

4-2024

## GRAPHENE 2D HETEROSTRUCTURES FOR THZ APPLICATIONS

Omnia Samy Shaaban

Follow this and additional works at: [https://scholarworks.uaeu.ac.ae/all\\_dissertations](https://scholarworks.uaeu.ac.ae/all_dissertations)



Part of the [Systems and Communications Commons](#)

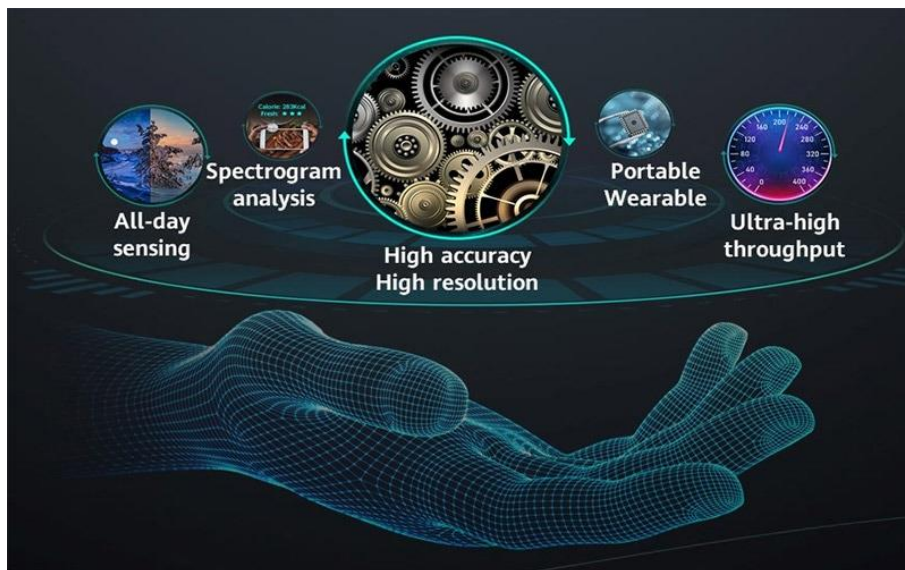
---

DOCTORATE DISSERTATION NO. 2024: 28

College of Engineering

GRAPHENE 2D HETEROSTRUCTURES FOR THZ APPLICATIONS

*Omnia Samy Shaaban Aly Darwish*



*April 2024*

United Arab Emirates University

College of Engineering

GRAPHENE 2D HETEROSTRUCTURES FOR THZ  
APPLICATIONS

Omnia Samy Shaaban Aly Darwish

This dissertation is submitted in partial fulfilment of the requirements for the degree of  
Doctor of Philosophy in Electrical Engineering

April 2024

**United Arab Emirates University Doctorate Dissertation**  
**2024: 28**

THz technology for life

Cover: Image related to THz technology used in the research

(Photo: <https://www.huawei.com/en/huaweitech/future-technologies/terahertz-sensing-communication>)


© 2024 Omnia Samy Shaaban Aly Darwish, Al Ain, UAE

All Rights Reserved

Print: University Print Service, UAEU 2024

## Declaration of Original Work

I, Omnia Smay Shaaban Aly Darwish, the undersigned, a graduate student at the United Arab Emirates University (UAEU), and the author of this dissertation entitled “*Graphene 2D Heterostructures for THz Applications*”, hereby, solemnly declare that this is the original research work done by me under the supervision of Dr. Amine El Moutaouakil, in the College of Engineering at UAEU. This work has not previously formed the basis for the award of any academic degree, diploma or a similar title at this or any other university. Any materials borrowed from other sources (whether published or unpublished) and relied upon or included in my dissertation have been properly cited and acknowledged in accordance with appropriate academic conventions. I further declare that there is no potential conflict of interest with respect to the research, data collection, authorship, presentation and/or publication of this dissertation.

Student's Signature: 

Date: 29 / 1 / 2024

## **Advisory Committee**

1) Advisor: Amine El Moutaouakil

Title: Associate Professor

Department of Electrical and Communication Engineering

College of Engineering

2) Co-advisor: Adel Najar

Title: Associate Professor

Department of Physics

College of Science

## Approval of the Doctorate Dissertation


This Doctorate Dissertation is approved by the following Examining Committee Members:

- 1) Advisor (Committee Chair): Amine El Moutaouakil

Title: Associate Professor

Department of Electrical and Communication Engineering

College of Engineering

Signature 

Date May 9<sup>th</sup>, 2024

- 2) Member: Mahmoud F Al Ahmad

Title: Professor

Department of Electrical and Communication Engineering

College of Engineering

Signature 

Date May 9<sup>th</sup>, 2024

- 3) Member: Nouredine Amrane

Title: Professor

Department of Physics

College of Science

Signature 

Date 9<sup>th</sup> May 2024

- 4) Member (External Examiner): Baker Mohammad

Title: Professor

Department of Computer and Communication Engineering

Institution: Khalifa University (KU), UAE

Signature For Prof. Baker Date 13/5/2024



This Doctorate Dissertation is accepted by:

Dean of the College of Engineering: Professor Mohamed Al-Marzouqi

Signature Mohamed AlMarzouqi

Date July 04, 2024

Dean of the College of Graduate Studies: Professor Ali Al-Marzouqi

Signature Ali Hassan

Date July 5, 2024



## Abstract

THz technology is a promising field that has various applications in communication, medical imaging and diseases' detection, scanning, and the food industry. Since THz technology is still in its early stages, there is a lot of work to be done to obtain devices that work efficiently in the THz range. One of these devices is THz absorbers that are the basic building blocks for the next generation THz systems whether in communication systems, imaging or shielding. THz absorbers are structures that can absorb electromagnetic waves in the THz range (0.1-10 THz). THz absorbers can be wideband (absorb a wide range of THz frequencies) or selective frequency absorbers (absorb a specified THz frequency). The aim of this study is to reach a nearly perfect selective THz absorber with near unity absorption based on 2D materials. 2D materials are known to have low cost, and they are abundant, and easy to fabricate through typical techniques like chemical vapor deposition (CVD) and dry transfer. The focus of the work is to study the characteristics of recently reviewed materials like MoS<sub>2</sub> and phosphorene and their heterostructures characteristics with graphene then utilizing these properties to design an absorber. This study is a theoretical based one, where the finite element method (FEM) is used to simulate the final design that was based on the previous experimental and theoretical calculations. The simulation was verified by applying the transmission circuit theory that verifies the high absorption of the structure. The proposed structure is the first to have a high absorption above 90% and that reaches 95% for some frequencies that is based on 2D materials without including noble materials like gold and silver to increase its absorption. The device is electrically tunable through most of the THz spectrum (1.3 THz -10 THz) that surpasses previous metamaterial absorbers which have limited range tunability. These characteristics enable easy fabrication and low-cost preparation that is considered an advancement in the THz absorbers.

**Keywords:** MoS<sub>2</sub>/graphene heterostructure, phosphorene/graphene heterostructure, THz applications, THz absorbers, transmission line circuit theory, graphene nanoribbons.

## Title and Abstract (in Arabic)

### تطبيقات التيراهيرتز لبني الجرافين المتغيرة

#### الملخص

تعتبر تقنية التيراهيرتز أحد أهم التقنيات الواعدة ذات التطبيقات في مجالات مختلفة مثل أجهزة الاتصالات و المجال الطبي سواء في التصوير الطبي أو للكشف عن بعض الأمراض وكذا في الصناعات الغذائية. و بما أن تقنية التيراهيرتز مازلات تخطو خطواتها الأولى فأمامنا العديد من الجهود حتى نتمكن من الحصول على نبائط تعمل بكفاءة في هذا الطيف من الترددات. و تعد ماصات التيراهيرتز أحد المكونات الأساسية لأنظمة التيراهيرتز المستقبلية حيث تتواجد في أنظمة الاتصالات و الفحص الطبي و التصوير بوجه عام وكذا حجب الأشعة الغير مرغوب فيها. إن ماصات التيراهيرتز هي أجهزة قادرة على امتصاص موجات التيراهيرتز و قد تكون واسعة النطاق بحيث تمتص حيز ترددات تيراهيرتز كبير أو صغيرة المدى بحيث تمتص تردد محدد بعينه. إن هدف هذه الدراسة هو تصميم ماص شبه مثالي ذو قدرة على الامتصاص تقرب من ال 100% لأشعة التيراهيرتز و يعتمد على المواد ثنائية الأبعاد التي تعد قليلة التكلفة و متوفرة و سهلة التحضير من خلال الطرق التقليدية مثل الترسيب الكيميائي. إن هذا البحث يناقش خصائص المواد الرائجة مؤخرا مثل ثاني كبريتيد الموليبدينوم  $MoS_2$  و الفسفورين و خصائص هذه المواد في البنى الغير متجانسة للجرافين و توظيف هذه الخصائص لعمل الماص المثالي. إن هذا البحث هو دراسة نظرية تم فيها استخدام " طريقة العناصر المحدودة" لمحاكاة التصميم المقترح معتمدين في ذلك على الأبحاث التجريبية و النظرية السابقة. و قد تم التحقق من النتائج بتطبيق " نظرية دوائر النقل" التي أكدت القدرة العالية لهذا التصميم على امتصاص أشعة التيراهيرتز. إن التصميم المقترح هو الأول من نوعه الذي له القدرة على امتصاص أكثر من 90% من الأشعة الساقطة عليه و التي تصل إلى 95% أو أكثر عند بعض الترددات و الذي في نفس الوقت لا يستخدم أي من المعادن النفيسة مثل الذهب أو الفضة للوصول لهذا الامتصاص العالي. كما يمكننا ضبط التردد المراد امتصاصه إلكترونيا عن طريق تحديد قيمة فرق الجهد المطبق عليه والذي بدوره يمكنه مسح أغلب ترددات التيراهيرتز (1.3-10 تيراهيرتز) و هكذا تفوق الماصات السابقة التي تتميز بقدرتها العالية للامتصاص لترددات محددة فقط. إن هذه الخصائص تتيح سهولة التصنيع بتكلفة منخفضة و الذي يعد سبقا في هذا المجال.

**مفاهيم البحث الرئيسية:** البنى الغير متجانسة للجرافين مع ثاني كبريتيد الموليبدينوم  $MoS_2$  ، البنى الغير متجانسة للجرافين مع الفسفورين، تطبيقات التيراهيرتز، ماصات التيراهيرتز، الشرائط النانوية للجرافين، نظرية دوائر النقل.

## **Author's Contribution**

The contribution of Omnia Samy to the dissertation was as follows:

- I. Participated in planning of the work, had main responsibility for interpreting previous literature, the theoretical analysis, simulation, and evaluation of results.
- II. Sole responsibility for the analysis and simulation results.

## **Author Profile**

Omnia Samy Shaaban Aly Darwish received her bachelor's and master's degrees from Ain Shams University in Egypt. During her master's degree she worked on modeling and simulation of nanoscale semiconductor devices. She introduced a compact model for double gate MOSFETs that are ready to be used in CAD tools for circuit simulation like SPICE simulation tools. She solved 2D mathematical problems that consider transistor aging. She was able to publish her work in Microelectronics journal in Elsevier and also was the co-author of another one in Silicon. Besides sharing her work in IEEE international conference.

Her PhD work is related to 2D materials and their applications in the THz region. Through her PhD she gets a solid background of 2D materials like graphene, MoS<sub>2</sub>, and phosphorene. She learnt about their properties and plasmonics. She wrote two review papers on MoS<sub>2</sub>, where one of them is published in Q1 journal. She used density functional theory to simulate material structures and unveil their properties. She also designed a perfect absorber based on 2D materials and simulated her work using finite element method simulation. She was able to publish part of her work in impacted journal and the rest of her work is still under publication. She participated in local and international conferences where the work is published in IEEE Xplore. She had the opportunity to visit Mohammed IV Polytechnic University (UM6P) where she got training on how to operate the chemical vapor deposition (CVD) device. She is willing to pursue her research work on projects where she can utilize her theoretical and experimental knowledge to help have a better world.

## **Acknowledgements**

All Praise to Allah, the Almighty, who has bestowed upon me the strength, knowledge, and blessings needed to complete this work.

I would like to express my deepest gratitude to my advisor, Dr. Amine El Moutaouakil for his continuous support, guidance, and invaluable insights throughout the research process. His expertise and encouragement played a pivotal role in shaping this thesis. I also extend my appreciation to my colleagues and professors in the department who created a welcoming and friendly atmosphere. Furthermore, I'd like to thank Dr. Abdelouahed El Fatimy, the head of institute of applied physics (IAP) at Mohammed IV Polytechnic University and his team particularly Vivek Chaudhary for giving me the opportunity to experience chemical vapor deposition (CVD) process at the university lab and completing part of the experimental work of this thesis.

I am thankful to my family for their constant encouragement and understanding during the ups and downs of this academic journey.

Finally, I acknowledge the financial support from the UAEU that made this research possible.

## Dedication

*To my family, friends, and professors*

## Table of Contents

Title .....	i
Declaration of Original Work .....	iii
Advisory Committee .....	iv
Approval of the Doctorate Dissertation .....	v
Abstract .....	vii
Title and Abstract (in Arabic) .....	viii
Author's Contribution .....	ix
Author Profile .....	x
Acknowledgements .....	xi
Dedication .....	xii
Table of Contents .....	xiii
List of Tables .....	xv
List of Figures .....	xvi
List of Abbreviations .....	xviii
Chapter 1 : Introduction .....	1
1.1 Overview .....	1
1.2 Statement of the Problem .....	3
1.3 Research Objectives .....	3
1.4 Relevant Literature .....	4
1.4.1 Plasma Oscillations .....	4
1.4.2 2D Materials Properties, and Plasmonic Oscillations .....	6
1.4.3 MoS <sub>2</sub> /Graphene Heterostructures.....	12
1.4.4 In-Plane Graphene/Phosphorene Heterostructure .....	13
1.4.5 Opening the Band Gap of Graphene .....	14
1.4.6 Hall and Edge Effects .....	15
1.4.7 Two-Dimensional (2D) Materials Synthesis.....	17
1.4.8 Previous THz Absorbers .....	20
Chapter 2 : Methods.....	24
2.1 Theoretical Approach.....	24
2.1.1 The Dielectric Function of Plasma (Free Electron Gas) .....	24
2.1.2 Intra-band and Inter-band Transitions.....	27

2.1.3 Optical Conductivity of Graphene (Kubo Formula) .....	28
2.1.4 Optical Conductivity of MoS <sub>2</sub> and Phosphorene (Drude Model) .....	30
2.1.5 The Operating Point of Phosphorene .....	37
2.1 Modeling and Simulation .....	38
2.2.1 Structure and Design .....	40
2.2.2 Graphene and MoS <sub>2</sub> Heterostructure .....	41
Chapter 3 : Results .....	44
3.1 MoS <sub>2</sub> Nanoribbons on SiO <sub>2</sub> .....	44
3.2 Graphene Nanoribbons on SiO <sub>2</sub> .....	46
3.3 MoS <sub>2</sub> /Graphene nanoribbons Heterostructure on SiO <sub>2</sub> .....	51
3.4 Phosphorene Nanoribbons on SiO <sub>2</sub> .....	57
3.5 The Proposed Structure (MoS <sub>2</sub> /Graphene-Phosphorene- MoS <sub>2</sub> /Graphene).....	61
Chapter 4 : Discussion .....	65
4.1 Validating the Novelty of the Structure.....	65
4.2 Interpreting Results using the Transmission Line Circuit Theory .....	67
Chapter 5 : Conclusion and Future Work .....	72
5.1 Conclusion.....	72
5.2 Future Work (Synthesis) .....	73
5.2.1 Cleaning Process before Synthesis .....	74
5.2.2 MoS <sub>2</sub> Synthesis .....	77
5.2.3 Experimental Results .....	78
References.....	80
List of Publications .....	98
Appendix.....	99



## List of Tables

Table 1: 2D materials Synthesizing Techniques.....	22
Table 2: List of previous THz Absorbers .....	66

## List of Figures

Figure 1: Frequency spectrum .....	1
Figure 2: The four main applications of THz waves in communication systems.....	2
Figure 3: MoS <sub>2</sub> structure.....	8
Figure 4: The real and imaginary parts of complex permittivity of MoS <sub>2</sub> with different numbers of layers .....	9
Figure 5: Monolayer MoS <sub>2</sub> Photoluminescence, absorption, and Differential reflectivity (R) spectra.....	10
Figure 6: Black phosphorus structure .....	11
Figure 7: Hexagonal Boron Nitride (h-BN) structure.....	12
Figure 8: Band gap alignment of graphene and MoS <sub>2</sub> heterostructure.....	13
Figure 9: In plane Monolayer phosphorene/ graphene heterostructure .....	14
Figure 10: E <sub>g</sub> versus the nanoribbon width for different devices with different orientations.....	16
Figure 11: The edge structure for MoS <sub>2</sub> and graphene edges.....	17
Figure 12: 2D materials synthesizing techniques. ....	18
Figure 13: The real part of optical conductivity of BP in the AC direction in case of doped and undoped BP. ....	31
Figure 14: The effect of applying a vertical electric field on monolayer BP .....	33
Figure 15: The effect of a vertical applied field on four layers BP. ....	35
Figure 16: The effect of increasing the dopant density on the band gap of four- layer BP.....	36
Figure 17: The band gap (eV) versus the external electric field E <sub>ext</sub> (V/Å) for BP. ....	37
Figure 18: The effect of applied voltage on the band gap of monolayer phosphorene .....	37
Figure 19: The variation of the band gap of MLBP under the effect of electric field .....	38
Figure 20: A 2D schematic of a unit cell of the array of infinite nanoribbons.....	41
Figure 21: The schematic of the infinite nanoribbon structure.....	42
Figure 22: The proposed Structure of graphene, MoS <sub>2</sub> , and MLBP.....	43
Figure 23: A 2D schematic of monolayer nanoribbon MoS <sub>2</sub> on SiO <sub>2</sub> .....	44
Figure 24: The absorptance and transmittance of MoS <sub>2</sub> nanoribbons .....	45
Figure 25: The electric field distribution across the MoS <sub>2</sub> nanoribbon at different frequencies (f) .....	45
Figure 26: The effect of the structure dimensions on the absorption frequency of MoS <sub>2</sub> nanoribbons.....	46
Figure 27: The absorptance of graphene when considering the Drude model only .....	47
Figure 28: Graphene nanoribbons over SiO <sub>2</sub> .....	49

Figure 29: The electric field distribution across graphene nanoribbon at different frequencies (f) .....	50
Figure 30: The effect of gate voltage on the absorptance and transmittance of graphene nanoribbons. ....	50
Figure 31: The effect of the structure dimensions on the absorption frequency of graphene nanoribbons. ....	51
Figure 32: The absorptance of MoS <sub>2</sub> /graphene heterostructure at different gate voltages .....	53
Figure 33: Comparison between the absorption of graphene only and MoS <sub>2</sub> /graphene heterostructure .....	54
Figure 34: The Electric field amplitude across one nanoribbon .....	54
Figure 35: The effect of the nanoribbon width $W_n$ on the absorptance frequency .....	55
Figure 36: The effect of the substrate thickness $d_{sub}$ of SiO <sub>2</sub> on the absorptance .....	56
Figure 37: The effect of temperature on the absorptance of the nanoribbon structure .....	56
Figure 38: The effect of temperature on the absorptance of the nanoribbon structure .....	57
Figure 39 : Phosphorene nanoribbons on SiO <sub>2</sub> .....	58
Figure 40: The electric field distribution of phosphorene nanoribbon at different frequencies .....	59
Figure 41: The effect of the structure dimensions on the absorption frequency of phosphorene nanoribbons.....	60
Figure 42: The effect of varying the vertical voltage $V_{BP}$ on the absorption frequency .....	61
Figure 43: The surface electric field of a unit cell of the proposed structure .....	63
Figure 44: The nanoribbon width effect on sweeping the absorption frequency .....	63
Figure 45: The effect of voltage applied on MoS <sub>2</sub> /Gr heterostructure on shifting the absorptance frequency .....	64
Figure 46: The effect of the substrate thickness $d_{sub}$ on the absorptance, reflectance (R), transmittance (T) of the structure .....	64
Figure 48 The transmission line model for a unit cell of the proposed structure .....	68
Figure 48: The normalized input impedance $Z_{in}$ for the proposed structure.....	71
Figure 49: Cleaning process steps .....	76
Figure 50: The Sulphur and the MoO <sub>3</sub> on chip .....	77
Figure 51: The positions of the boats carrying Sulfur and Silicon wafer in the CVD tube. ....	78
Figure 52: The temperature settings of the CVD middle zone furnace. ....	78
Figure 53: Different parts of the chip after growing MoS <sub>2</sub> using CVD .....	79
Figure 54: Different parts of the chip after cleaning with Toluene .....	79

## List of Abbreviations

AC	Armchair Direction
ALD	Atomic Layer Deposition
BP	Black Phosphorous
CBM	Conduction Band Minimum
CVD	Chemical Vapor Deposition
DFT	Density Functional Theory
DI	Deionized Water
DOS	Density of States
EEM	Effective Electron Mass
FEM	Finite Element Method
h-BN	Hexagonal Boron Nitride
IR	Infrared
LDA	Local Density Approximation
MLBP	Monolayer Black Phosphorous
M-MoS <sub>2</sub>	Metallic-Phase Molybdenum Disulfide
MSA	Metasurface Absorber
PLD	Physical Layer Deposition
SCCM	Standard Cubic Centimeters Per Minute
SPPs	Surface Plasmons Polaritons
SPs	Surface Plasmons
THz	Terahertz
VBM	Valence Band Maximum
ZZ	Zigzag Direction

# Chapter 1 : Introduction

## 1.1 Overview

Terahertz (THz) frequency, the frequency range that covers from 0.1 THz to 10 THz or sometimes defined as the frequency range from 0.3 THz to 10 THz, or the submillimeter wavelength spectrum (30  $\mu\text{m}$ -3 mm) is found to be a promising frequency for a wide range of medical applications, and communication systems Figure 1. It lies between the infrared (IR) and the microwave frequencies and sometimes referred to as far IR that covers from (15  $\mu\text{m}$  – 1 mm) and sometimes it is called the THz gap as it is the undiscovered frequency range between the microwave and the IF frequencies. This frequency spectrum has low energy and low frequency compared to x and  $\gamma$  rays and is a non-ionizing frequency that enabled it to invade the medical field vigorously as it is considered safe and non-devastating for humans. THz radiation is considered near to human bodies radiations or thermal radiations that are in the infrared spectrum. THz radiation is used to detect and cure cancer and as a biomarker for DNA. Their high penetration enabled them to be used in detection and imaging whether in food industry or security scanning.

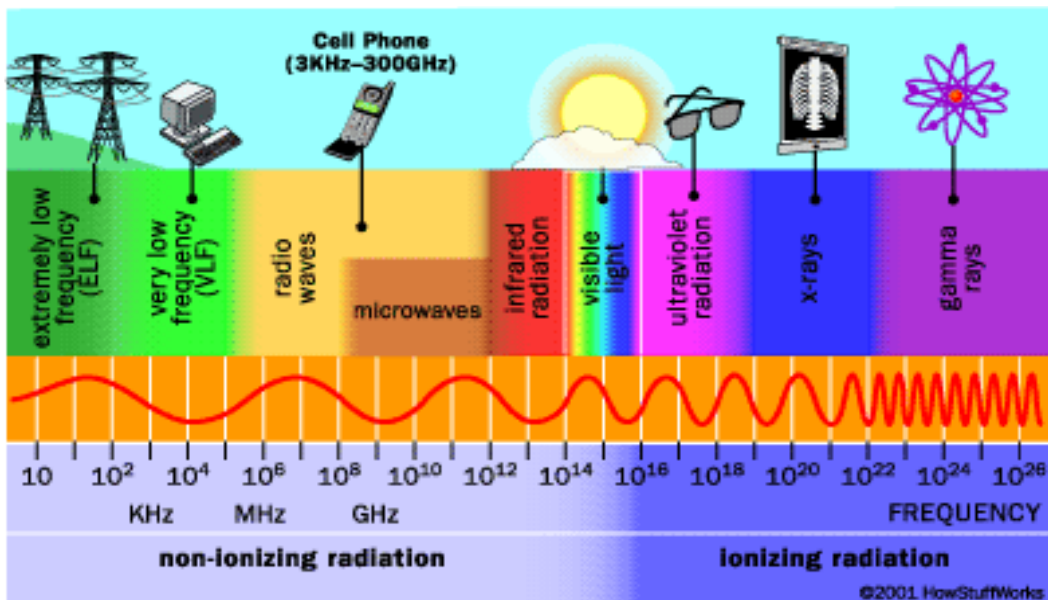


Figure 1: Frequency spectrum (Ouda, 2007)

THz frequency has promising applications in different aspects of life. The most appealing are in communication, sensing, and scanning. THz frequency is promising for 6G wireless communications that can have up to 100 Gbps (Chaccour et al., 2022). Due to its high frequency and short wavelength, it is promising for faster communication and larger bandwidths when compared to 5G communication that are in the range of microwave frequencies (speed up to 10 Gbps). However, THz frequencies are prone to molecular absorption and dissipation where they travel for short distances only because of its short wavelength. Figure 2 illustrates the four prospected main applications of THz frequency in communication where all of these completely automated systems require Ultra-high-speed communication in range of tera bits per second (Tbps), high fidelity, large amount of data transfer and near-zero latency. The use of the THz waves in medical applications isn't restricted to scanning and detecting cells and diseases like detecting cancer but it has potential towards cancer treatment at high-power frequency radiation (El-Shenawee et al., 2019; Gezimati & Singh, 2023; Yu et al., 2019). THz technology is a new era of communication that will revolutionize our way of life. However, typical semiconductor devices fail to work as transceivers in the THz region or to effectively convert electrical energy into electromagnetic energy. We are in need of developing new devices, antennas and sensors that are compatible with the THz range. Graphene showed better optical properties that allow transceivers to be tunable, compact, high-speed, and energy efficient. This is due to its plasmonic resonance that occurs at electromagnetic excitations.

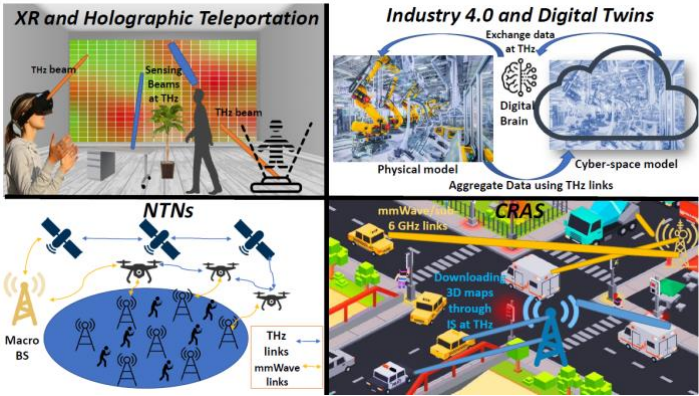


Figure 2: The four main applications of THz waves in communication systems.

From top left to right holographic teleportation, and extended reality (XR), digital twins, Non-Terrestrial Networks (NTNs), and connected robotics and autonomous systems (CRAS). IEEE communications surveys & tutorials 2022 (Chaccour et al., 2022)

## 1.2 Statement of the Problem

Communication is one of the eminent applications of the THz technology where the progress in developing electronic components that align with this emerging technology is still in its early stages. We are in need of developing new electronic devices that can work efficiently in the THz band. There are lots of electronic components that are used in transceivers and sensors and in this work, we focus on THz absorbers that are crucial components in communication systems. Previous THz absorbers are bulky (tenth to hundreds of micrometers), have complicated design which means complex and expensive fabrication techniques, and mostly includes gold or noble metals (Ag, Pt) to achieve high absorptivity. Besides, most of the previous work focused on broadband absorbers which of course have an important role in THz shielding but very little work discussed narrow band absorbers or selective frequency absorbers that are used in sensing and enhancement of electric and magnetic field. The previously developed broadband absorbers have limitations with the frequency range they operate at. They have high absorptivity over a specific range but can't be tuned over the whole THz spectrum. In this work, we focused on selective frequency absorbers with relatively low bandwidth. We aimed at developing a THz absorber with high absorptivity, low cost, simple design and easy fabrication that can be tuned over the whole THz range.

## 1.3 Research Objectives

The aim of this research is to develop a high absorptivity THz absorber based on 2D materials including graphene. The objective was to choose abundant and low-cost materials that could increase the absorptivity of graphene and include them in a simple design, while considering the tunability of the absorber almost all over the THz band. Graphene is on top of optical materials that has plasmonic resonance in the THz range, beside its optical tunability. At first, the absorptivity of the simplest structure of graphene nanoribbons absorptance was checked and it didn't exceed 50%. Molybdenum disulfide ( $\text{MoS}_2$ ) and Monolayer black phosphorous (MLBP), which is also called phosphorene, are the subsequent intensively studied materials. The absorptivity of the heterostructures and combinations of these materials with graphene was studied. The structure dimensions and structure were modulated to achieve the required absorptance.

After that, an absorber structure was proposed including those three materials to have high absorptivity ( $>90\%$ ). The proposed structure is analyzed through the finite element method (FEM) simulation and then verified analytically through the transmission line circuit theory that confirmed the high absorptivity of the design through and beyond the THz range.

## **1.4 Relevant Literature**

In this section, we will present the basic physics and material properties that opened the way for 2D materials to be used in optical and electronic applications. Plasmonic oscillations of 2D materials are one of the main characteristics that enabled their use in ultra-thin absorbers. The band gap of these materials can change with the material thickness (number of layers) and the vertical applied voltage. We will discuss these properties in detail in the next sections.

### *1.4.1 Plasma Oscillations*

Plasmonic oscillations in metals date back to the Roman empire, 4th century AD, where the inclusion of gold nanoparticles in glass was used to make the most spectacular glass the Lycurgus cup that brighten green from one side (reflecting) and red from the other one (transmitting). This was also used in church windows. The free electrons in metals behave as a sea of electronic oscillations that absorb certain frequencies and emit them resulting in different colors. Free electrons and holes in semiconductors can exhibit plasmonic oscillations under some conditions. The plasma oscillations in semiconductors were first mentioned in (Dyakonov & Shur, 1993, 1996). In those studies, it was proposed that in short channel semiconductors, ballistic transport is supported because there is no collisions with phonons and/or impurities during the transit time. However, due to very short channel electrons-electrons collisions exist and they can't be considered ballistic particles. They are in need of another definition to describe their state. The electrons behave as a plasma that obeys hydrodynamic equations. The electrons induce a plasma wave that is magnified due to reflections from the device boundaries. These plasma waves were said to be in the THz range. A gate voltage and an electromagnetic radiation can induce a constant drain to source current that depends on



the plasma oscillations. In general, there are three main conditions for an ionized gas to have plasma oscillations (Ancker-Johnson, 1966; Ghosh, 2014; Maier, 2007):

1.  $L \gg \lambda_D$

The linear dimension or the channel length  $L$  must be greater than the “Debye length”  $\lambda_D$  that is defined as:

$$\lambda_D = \frac{1}{\sqrt{2}} \sqrt{\frac{\epsilon_0 K_B T}{n_0 q^2}} \quad (1.1)$$

Where  $\epsilon_0$  is the free space permittivity,  $K_B$  is the Boltzmann constant and  $T$  is the temperature in Kelvin, and  $q$  is the electronic charge.  $n_0$  is the density of both electrons and ions  $n_0 = n_e \cdot n_i$

2.  $N_D > 1$

The number of particles in a ‘Debye sphere’ (which is a sphere with radius  $\lambda_D$ ) must be very much greater than unity.

$$N_D = \frac{4}{3} \pi \lambda_D^3 n_0 \text{ OR } \lambda_D \gg \frac{1}{\sqrt[3]{n_0}} \quad (1.2)$$

In other words, the Debye length must be greater than the interparticle distance.

3.  $\omega_p \tau > 1$

The period of typical plasma oscillation must be much smaller than the mean time  $\tau$  between collisions with atoms. In other words, the mean free path of electron-electron collisions doesn’t exceed the channel length and the mean free path of electron-phonon and electron-impurities scattering (Dyakonov & Shur, 1993).  $\omega_p$  is the plasma oscillation frequency.

From the above conditions for plasmonic oscillations (condition 2), it is clear that increasing the carrier concentrations decreases the Debye length and facilitates the occurrence of plasma resonance. That’s why 2D surfaces are said to have better plasmonic resonance, due to the strong coupling of the surface charges (Dyakonov & Shur, 1993). We are using monolayers of graphene, MoS<sub>2</sub>, and BP so beside their outstanding properties for monolayer structure, they also have better plasmonic resonance. When the above conditions are satisfied, surface plasmons exist. They can be localized surface plasmons that don’t propagate (localized) on the surface or propagating surface plasmons (PSPs) that are sometimes called surface plasmons polaritons (SPPs)

that propagates on the surface. Those SPPs have electric field that decays exponentially as we go into the dielectric substrate depth, defined by the penetration depth ( $L_{PD}$ ), which depends only on optical properties of both material and substrate at a given wavelength (Jatschka et al., 2016). When materials are excited with a frequency near their plasmon oscillations, we have to include the complex permittivity function as a function in the angular frequency  $\omega$  as  $\epsilon(\omega) = \epsilon_{real}(\omega) + i\epsilon_{imag}(\omega)$ , where  $\epsilon_{real}(\omega)$  is the real part of permittivity and  $\epsilon_{imag}(\omega)$  is the imaginary part. The complex dielectric permittivity and refractive index are related through the equation:

$$\tilde{n}(\omega) = n(\omega) + i\kappa(\omega) \quad (1.3)$$

$n$  is the real part of the refractive index and  $\kappa$  is the extinction coefficient or the attenuation coefficient that represent the amount of absorbed light, while  $n$  represents the dispersion in the medium (reflection and transmission). The relation between the refractive index and permittivity is  $\tilde{n}(\omega) = \sqrt{\epsilon(\omega)}$  from which we get the relations of the real and imaginary parts of refractive index as follows: (see the Appendix)

$$\epsilon_{real} = n^2 - \kappa^2 \quad (1.4)$$

$$\epsilon_{imag} = 2n\kappa \quad (1.5)$$

$$n^2 = \frac{\epsilon_{real}}{2} + \frac{1}{2}\sqrt{\epsilon_{real}^2 + \epsilon_{imag}^2} \quad (1.6)$$

$$\kappa = \frac{\epsilon_{imag}}{2n} \quad (1.7)$$

The absorption coefficient  $\alpha$  defined in Beer's law as  $I(x) = I_0 e^{-\alpha x}$  where  $I$  is the intensity of the propagating beam and  $I_0$  is the initial intensity of incident wave, can be related to the extinction coefficient through the relation (1.8) (Maier, 2007).

$$\alpha(\omega) = \frac{2\kappa(\omega)\omega}{c} \quad (1.8)$$

$c$  is the velocity of light described by  $c = \frac{1}{\sqrt{\mu_0\epsilon_0}}$ , where  $\mu_0$  is the free space permeability.

#### 1.4.2 2D Materials Properties, and Plasmonic Oscillations

In this section, we will discuss the three mostly studied and reputable materials that are known for their outstanding properties, which we adopted in our structure. They are graphene, MoS<sub>2</sub>, and phosphorene.

### 1.4.2.1 Graphene

Graphene the 2D allotrope of carbon and or the monolayer of graphite was first synthesized by (Novoselov et al., 2004). It is considered the thinnest material known with 0.334 nm thickness (a human hair is 50  $\mu\text{m}$ ). It has a large specific surface area ( $\sim 2600 \text{ m}^2/\text{g}$ ), and high electron mobility ( $200,000 \text{ cm}^2/\text{Vs}$ ) where the mobility of Si is  $<1400 \text{ cm}^2/\text{Vs}$ . It has a thermal conductivity of (3000–5000  $\text{Wm/K}$ ), extremely high optical transparency (97.4%) and exceptional mechanical strength, besides its biocompatibility (Urade et al., 2022). Graphene optical and electronic properties enabled its use in electronic devices that needs fast time response, as well as photonic devices. It has many applications in wearable devices, sensors, solar panels, DNA sequencing and drug delivery.

Graphene has a hexagonal honeycomb structure where each carbon atom is attached to three neighboring ones. Graphene has 4 valence electrons where 3 of them are distributed in the hybridized  $\text{SP}^2$  structure (formulated from  $2\text{S}$ ,  $2\text{P}_x$ ,  $2\text{P}_y$ ) making a strong sigma bond that is responsible for its mechanical strength. The fourth free electron in  $\text{P}_z$  orbital forms a delocalized pi bond with the surrounding atoms in a plane perpendicular to graphene. This free electron gives graphene its unique optoelectronic properties (Cui et al., 2021). Graphene is a zero-band gap semiconductor, so it can't be utilized in electronics without modifications as it will have a bad on/off ratio. Stripping graphene into nanoribbons or applying electric field or developing graphene heterostructures help in opening its band gap (Han et al., 2007). The band gap scales inversely with the nanoribbon width due to the 1D carrier confinement that occurs when stripping graphene into nanoribbons.

Graphene surface plasmons was monitored using a near field optical microscope (Cui et al., 2021), and it was demonstrated that the frequency and amplitude of the SPs can be tuned through applying a gate voltage, which is the most interesting about graphene (the optical tunability). SPs in graphene are propagating ones (SPPs) and are concentrated near the ends of nanoribbons and they are stronger for smaller ribbon widths (Cui et al., 2021).

### 1.4.2.2 MoS<sub>2</sub>

MoS<sub>2</sub> has an indirect band gap of 1.3 eV in the bulk state and a 1.9 eV direct band gap in monolayer. This band gap lies in the visible range that gives MoS<sub>2</sub> unique photoluminescence properties to be used in many optical applications and as a biomarker for cancer and DNA based sensors (Samy et al., 2021). MoS<sub>2</sub> has a hexagonal structure similar to graphene which facilitates its integration with it Figure 3. Stripping MoS<sub>2</sub> into nanoribbons extremely alters its properties. As the nanoribbon width decreases, the density of states (DOS) increases and the bandgap decreases until it reaches zero at one-dimensional (1D) ribbons, where metallic states are localized at the edges of the nanoparticles (Davelou et al., 2014). This is because increasing the width, decreases the fraction of edge metallic states (their number is constant), while the number of bulk nonmetallic states increases with the width. This can greatly affect the optical properties of MoS<sub>2</sub>. Time dependent density functional theory (TDDFT) was used to detect localized plasmons at the edge of a zigzag MoS<sub>2</sub> nanoribbon (Andersen et al., 2014). Another study for triangular MoS<sub>2</sub> monolayer flakes showed that there is a collective plasmon-like excitations at the edges that couple to optical field and causes significant absorption peaks below the onset of inter-band transitions (Rossi et al., 2017). Due to the edge metallic states, MoS<sub>2</sub> behaves as a n-type semiconductor with absorption in the THz region which only becomes significant at high carrier concentration of MoS<sub>2</sub>.

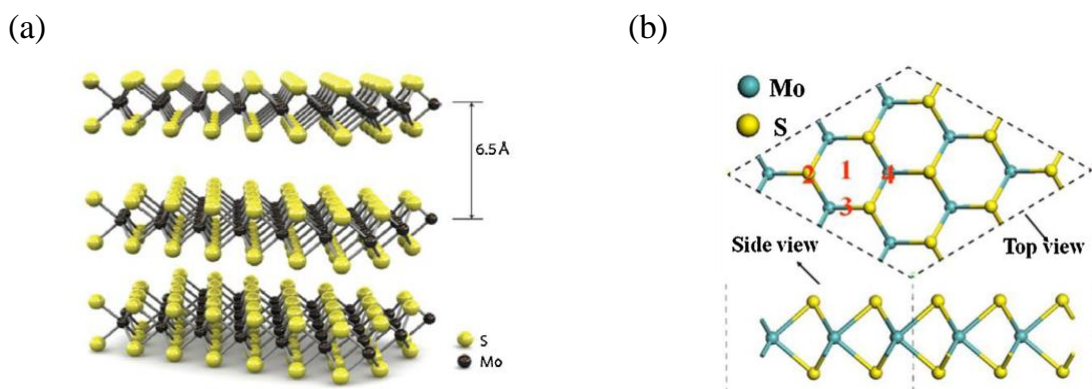


Figure 3: MoS<sub>2</sub> structure.

(a) 3D representation of MoS<sub>2</sub> layers with spacings 6.5 Å (b) Side view showing different sites; (1) hollow site, (2) top site of the S atom, (3) Mo-S bridge site, and (4) top site of the Mo atom. Reproduced from (He & Que, 2016). Applied Materials Today (2016), Elsevier.

The absorption of MoS<sub>2</sub> occurs at high frequencies and very low absorption could occur in the THz region by modulating the number of layers (Song et al., 2019). The low imaginary part of permittivity Figure 4, means low extinction and absorption coefficients as described in Equations (1.4)-(1.8). In our structure we want MoS<sub>2</sub> to act as a perfect transmitter, while making use of its heterostructure with graphene which has a notable effect on the carrier concentration and band gap of graphene as will be discussed later. The effect of varying the gate voltage on MoS<sub>2</sub> was checked in (Newaz et al., 2013) Figure 5, by applying gate voltage ranging from -50 V to 50 V, where it affects the absorption and photoluminescence at ~1.85 eV. The behavior at low frequencies wasn't discussed in this research, however, our band gap calculations using DFT theory (Quantum espresso) showed a possible decrease in the band gap of MoS<sub>2</sub> monolayer especially at high voltages (see Appendix) which also matches the study in (Liu et al., 2012).

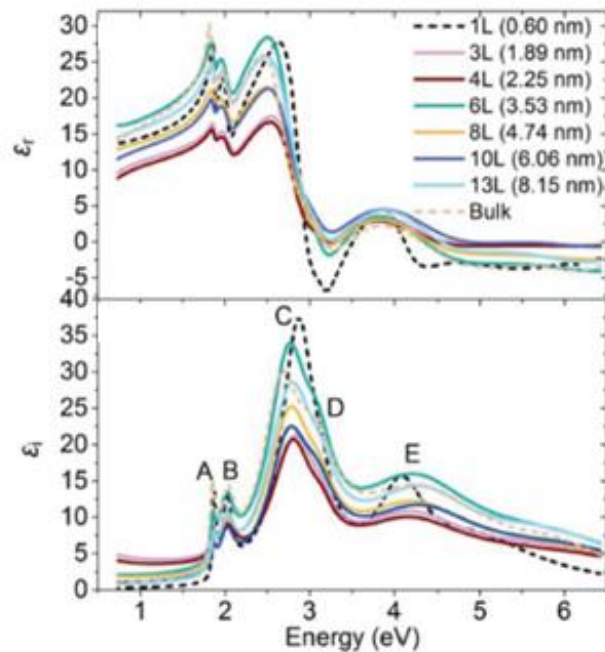


Figure 4: The real and imaginary parts of complex permittivity of MoS<sub>2</sub> with different numbers of layers. Reproduced from (Song et al., 2019). *Advanced optical materials*, 2019.

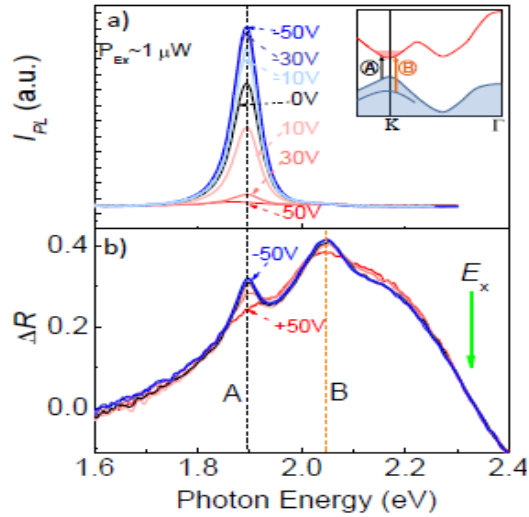


Figure 5: Monolayer MoS<sub>2</sub> Photoluminescence, absorption, and Differential reflectivity (R) spectra (a) Photoluminescence and absorption spectra in monolayer MoS<sub>2</sub>, (b) Differential reflectivity (R) spectra. Reproduced from (Newaz et al., 2013). Solid State Communications 2013, Elsevier.

#### 1.4.2.3 Phosphorene

Black phosphorous (BP) has gained popularity as a graphene substitute due to its favorable properties, including an electron mobility up to 1000 cm<sup>2</sup>/V.s and a hole mobility up to 10,000 cm<sup>2</sup>/V.s in monolayer, an excellent ON-OFF current ratio up to 10<sup>4</sup>, and potential biocompatibility (Anju et al., 2019). It is the most stable allotrope of phosphorous. Its band gap changes from 0.3 eV in bulk (multilayer) to 1.9 eV in monolayer which is known as Phosphorene. Like graphene, its band gap can be modified through applying electric field. BP exhibits high anisotropy where its optical conductivity varies according to the direction of light propagation whether zigzag or armchair Figure 6.

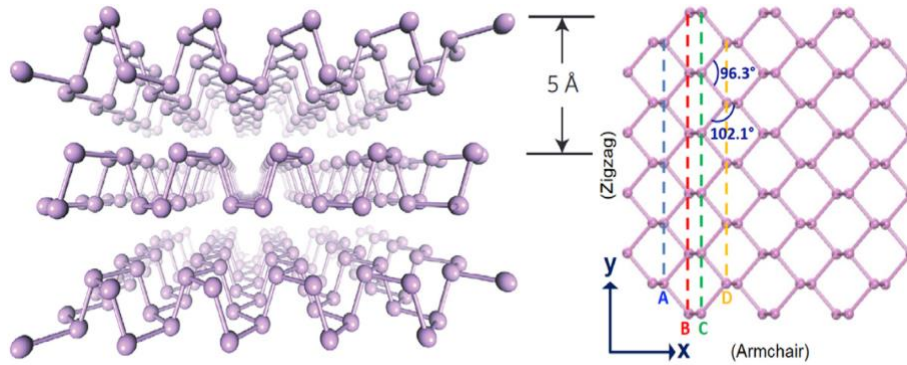


Figure 6: Black phosphorus structure. Adapted from (Mu et al., 2019). *Materials Today Physics*, Elsevier 2019

#### 1.4.2.4 Hexagonal Boron Nitride *h-BN*

Hexagonal Boron Nitride (*h-BN*) is a wide indirect bandgap semiconductor (considered as an insulator) with a fundamental gap ranging of  $4.9 \pm 1$  eV. It has a hexagonal honey comb structure resembling that of graphene that facilitates its integration with its (Cassabois et al., 2016; Satawara et al., 2021). The large band gap makes it a good absorber in the Ultra-violet (UV) frequency range with no absorption in the visible and the THz spectrum. Its good electronic, optical properties and stability facilitate its use in electronic devices. Its hexagonal crystalline shape enables its integration with other 2D materials like graphene,  $\text{MoS}_2$ , and phosphorene. *h-BN* is a promising insulator and coating for 2D devices. *h-BN* is known to have a phonon polarization with dispersion characteristics similar to graphene, this phonon polarization is called hyperbolic phonon polarization (HP2). In graphene/*h-BN* a kind of hybridization occurs between HP2 in *h-BN* and the surface plasmons (SP2) in graphene known as SP3 resulting in a longer propagation length than SP2 in graphene (Cui et al., 2021), where the propagation length is the distance travelled by the SPPs before its intensity decay by a factor of  $1/q$  where  $q$  is the electronic charge.

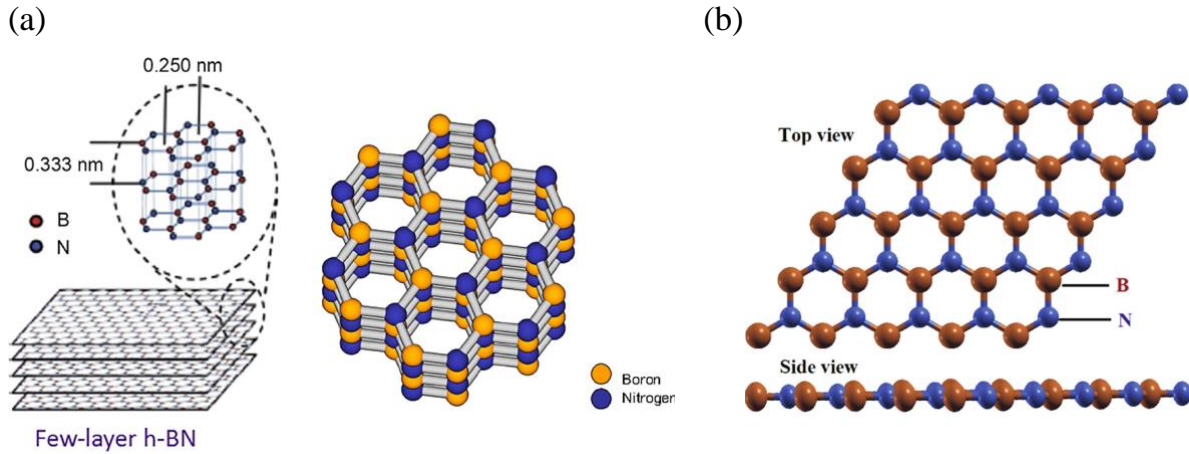


Figure 7: Hexagonal Boron Nitride (h-BN) structure

(a) Few layers; (b) Top and side views (Molaei et al., 2021; Satawara et al., 2021). Adapted from Materials today and Applied electronic materials, Elsevier, ACS 2021.

#### 1.4.3 MoS<sub>2</sub>/Graphene Heterostructures

MoS<sub>2</sub> and graphene heterostructures were intensively studied in previous work (Halim et al., 2022; Muñoz et al., 2022; Pham et al., 2019; Pierucci et al., 2016; Yu et al., 2020). Since graphene has no dangling bonds or impurities, it can make an abrupt interface with MoS<sub>2</sub> with approximately no depletion region. The band alignment of monolayer MoS<sub>2</sub>/graphene was studied in (Pierucci et al., 2016), where charge transfer from MoS<sub>2</sub> to graphene was not obvious, but possible charge transfer can't be neglected. The work estimated no depletion region between the two structures and deduced a band alignment between monolayers of MoS<sub>2</sub> and graphene without band bending as in Figure 8 (obtained from X-ray photoemission spectroscopy (XPS) measurement), where MoS<sub>2</sub> behaves as an n-type semiconductor and the  $\pi$  bands of graphene exhibited an n-doped concentration of  $9 \times 10^{12} \text{cm}^{-2}$ . Minibands in graphene were observed at higher binding energies. The experimental work in Gupta et al. (2022), showed that monolayer MoS<sub>2</sub>/graphene (where MoS<sub>2</sub> was placed over graphene) Van der Waals heterostructure induced surface electronic properties and electron transfer, in addition to increased photogenerated carriers. When biasing MoS<sub>2</sub> (n-type) with positive voltage, possible charge transfer occurs passing to graphene. However, for monolayer graphene on



monolayer MoS<sub>2</sub>, there was no hybridization in the electronic states of graphene and MoS<sub>2</sub>. The graphene structure does not change (Jin et al., 2015).

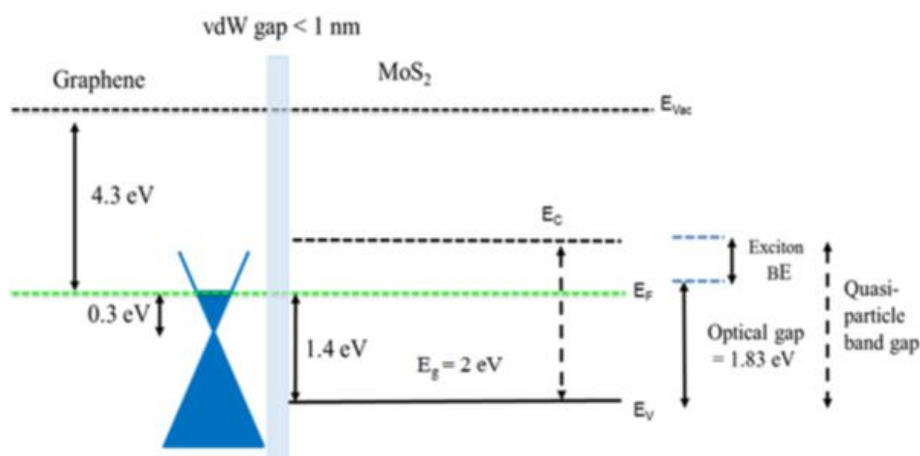
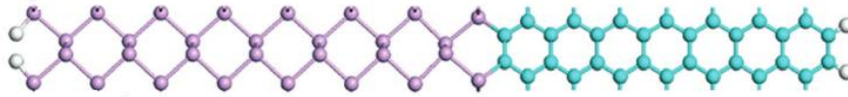


Figure 8: Band gap alignment of graphene and MoS<sub>2</sub> heterostructure. Reproduced from (Pierucci et al., 2016). ACS publications 2016.

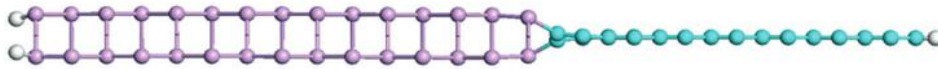
#### 1.4.4 In-Plane Graphene/Phosphorene Heterostructure

The tiny lattice mismatch of the armchair direction between graphene and phosphorene facilitates their in-plane heterostructure integration which result in an atomically sharp in-plane interface. The interlayer coupling can strongly influence the electronic properties. The band gap between the 2 interfaces can be detected through the differences in the on-site energies of two edges, and the hopping parameters for the intra- and inter-edge transitions, which are influenced by the hybridization of the  $\sigma$  bonds electronic states at the interface. As calculated in (Tian et al., 2015), the energy barrier at the interface blocks graphene electrons from migrating into phosphorene. The study also showed that a graphene/phosphorene/graphene structure results in tunnelling characteristics between graphene and phosphorene. The graphene and phosphorene are connected through strong chemical bond with length 1.86 Å, which is within that of C–C (1.42 Å) and P–P (2.17 Å) bonds. The work also illustrated that a vertical electric field effectively reduces the band gaps of the heterostructure and results in a semiconductor-to-metal transition.

(a)



(b)



(c)

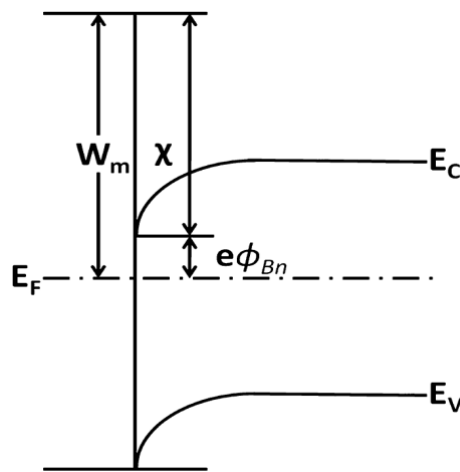


Figure 9: In plane Monolayer phosphorene/ graphene heterostructure.

(a) Top view; (b) Side view of a lateral phosphorene/graphene heterostructure; (c) The energy band diagram of the heterostructure interface, with Phosphorene on the right and graphene on the left.  $W_m$  is the work function of graphene,  $\chi$  is the electron affinity phosphorene,  $\phi_{BN}$  The Schottky barrier for the electron flow. Reproduced from (Tian et al., 2015). Published by Royal Society of chemistry 2015.

#### 1.4.5 Opening the Band Gap of Graphene

Graphene is a zero-band gap material which hinders its integration in electronic applications due to its low on/off ratio. Several techniques are used to open (increase) the band gap of graphene like developing graphene heterostructures or stripping it into nanoribbons or applying a vertical electric field. Both  $\text{MoS}_2$  and graphene have hexagonal structure which facilitates their vertical heterostructure formulation. The experimental work in Pierucci et al. (2016) showed the formation of minigaps in graphene when  $\text{MoS}_2$  is stacked over it. As discussed earlier, the authors attributed these band gaps due to the hybridization between the  $\pi$  band in graphene with the out of plane orbital in  $\text{MoS}_2$ . They confirmed no significant interaction between graphene and  $\text{MoS}_2$

interfaces with a possible charge transfer from MoS<sub>2</sub> to graphene. The angle of rotation between graphene and MoS<sub>2</sub> was shown to affect the band gap formulation in some studies and doesn't affect it in studies conducted by (Lin et al., 2023). It is to be noted that such band gap modulation wasn't found in graphene/MoS<sub>2</sub> structure (Jin et al., 2015).

Stripping graphene into nanoribbons induces a band gap, where the band gap increases with decreasing the width of the nanoribbons. The graphene orientation whether zigzag or armchair and the chemical termination affect the band gap scaling (Son et al., 2006). The work in Son et al. (2006) stated that graphene edges play an important role in the band gap opening. For the zigzag edges, the band gap  $\Delta$  can be estimated based on the nanoribbon width from  $\Delta = \frac{9.33}{W_{zz}+15}$  where  $W_{zz}$  is the nanoribbon width in Å. For a width of 90 nm (900 Å)  $\Delta = 10$  meV which is in the THz energy range based on  $E = h\nu$ . The experimental work in (Han et al., 2007) shows the band gap is less than 40 meV for widths from 20 nm to 90 nm. For widths > 90 nm we have band gaps down to 1 meV Figure 10. The band gap can then be swept to larger values by applying a gate voltage or an electric field on the nanoribbons.

#### *1.4.6 Hall and Edge Effects*

When a magnetic field is perpendicular to an electric current passing in a conductor, it causes the charges (electrons) to deflect to the edges of the conductor, away from the magnetic field, producing a potential difference across the conductor, this is known as the Hall effect that was named after Edwin Hall in 1879. A similar case is when we have a sea of electrons (plasma) on the surface of a monolayer-nanoribbon material (conductor), the plasmons deflect to the edges under the effect of magnetic field. The edge states could play a crucial role in the plasmonic oscillations especially for materials that are known for their chirality like BP, graphene and even MoS<sub>2</sub>. The study in Davelou et al. (2014) showed metallic edge states for MoS<sub>2</sub> nanoribbon under no external effect. The Density of states (DOS) at the edges increase as the nanoribbon width decreases. We have a 1D conducting states at the edge of 2D semiconductor (Bollinger et al., 2001). MoS<sub>2</sub> could have a zigzag (ZZ) or armchair (AC) edge where the ZZ direction was detected to have higher metallic states Figure 11a ;

(Thongrattanasiri et al., 2012; Xu et al., 2016). Graphene edges are also ZZ or AC, where in case of ZZ edges the plasmons at the edges can widen through the nanoribbon width Figure 11b. Phosphorene is highly anisotropic and have different characteristics in the ZZ and AC directions, with different effective electron masses in each direction, as will be discussed later in detail. The Hall effect in nanoscale monolayers open a big research field related to quantum and spin effects. Although we are not going to consider the magnetic effect in our calculations, we can't neglect its presence. As will be seen in the results section, the electric field is always concentrated at the edges of the nanoribbons with the highest electric field values at the edges.

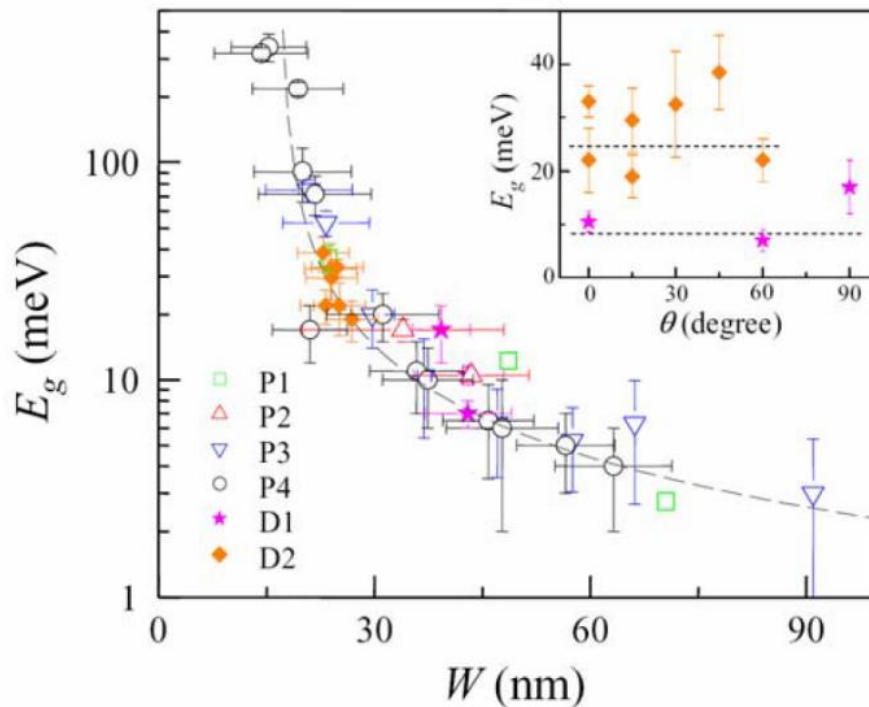
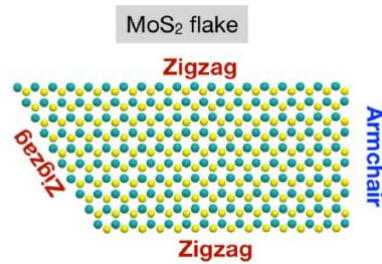


Figure 10:  $E_g$  versus the nanoribbon width for different devices with different orientations (Han et al., 2007)

Device P1-P4 have many ribbons of different widths set in parallel, and devices D1 and D2 have ribbons of the same width and different angles in between. Adapted from Physical Review letters 2007.

(a)



(b)

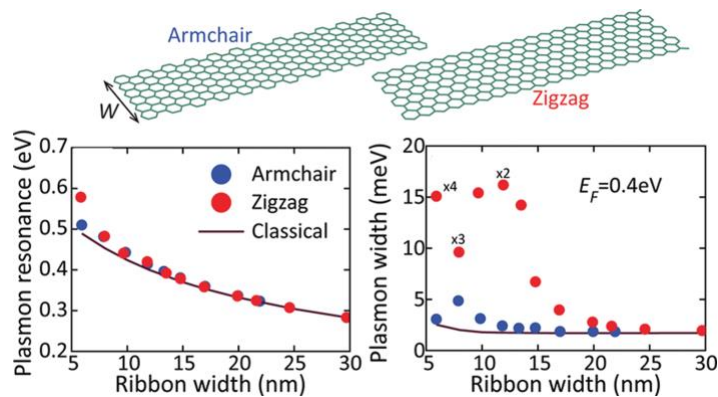


Figure 11: The edge structure for MoS<sub>2</sub> and graphene edges.

(a) MoS<sub>2</sub> flake with different edge orientations Adapted from (Tinoco et al., 2019). Nature 2019; (b) The AC and ZZ edges of graphene nanoribbons, having the same resonance frequency but wider plasmon width in case of ZZ (Thongrattanasiri et al., 2012). Adapted from ACS Nano, 2012.

#### 1.4.7 Two-Dimensional (2D) Materials Synthesis

Synthesizing 2D materials is an important aspect that can't be neglected when talking about 2D materials, since the easiness of their synthesis is one of the main advantages that directed research towards them. There are two main approaches for 2D material synthesis. Figure 12: The top-down approach and the bottom-up approach. In top-down approaches, external forces are applied to break the weak van der Waals forces in between the planes or layers of a bulk material without affecting the strong covalent bonds between atoms of a single layer (Yang et al., 2022).

Although this method is easy, simple and, doesn't require much technology, you can't control the exact number of layers you want, especially for a large area. This technique includes mechanical exfoliation using scotch tape, which is the easiest one, and chemical liquid exfoliation. The latter includes submerging the bulk material in a

solvent typically N-Methyl pyrrolidone (NMP) and dimethyl formamide (DMF) then put to sonication that will break the inter-planar van de Walls bonding. This results in well ultra-thin nanosheets (Samy et al., 2021).

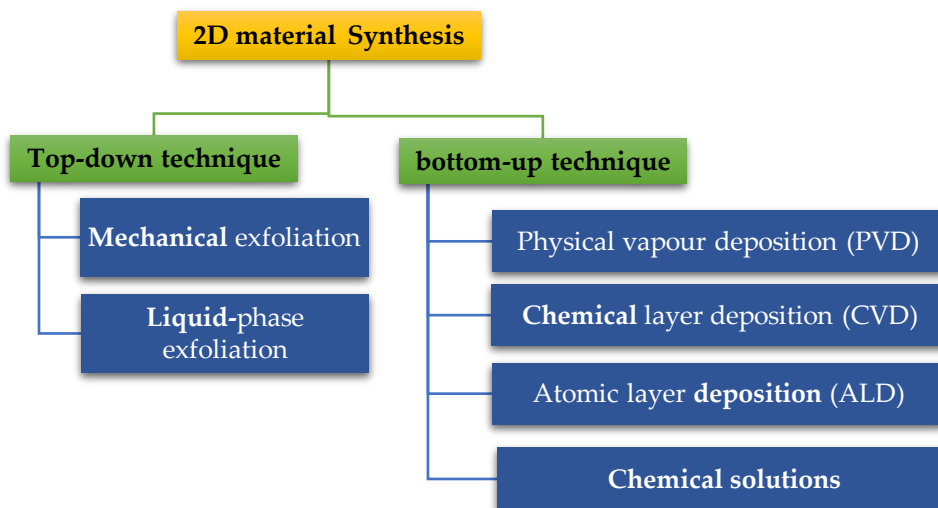


Figure 12: 2D materials synthesizing techniques.

The bottom-up approach depends on growing thin layers over a substrate. Deposition is a bottom-up technique where a thin layer of the material is grown over a substrate, and it could be achieved physically or chemically or through atomic deposition. Physical layer deposition (PVD) includes ion implantation like molecular beam epitaxy (MBE). It can produce thin-film coating of pure metals, metallic alloys and ceramics with a thickness usually in the range 1 to 10 $\mu$ m. In atomic layer deposition (ALD), pulses of precursors are used alternately, each pulse is separated by an inert gas to prevent gas reactions. ALD is an efficient technique, that produces layers with few impurities and uniform structure which are ready to be used in different applications, like electronics and sensors. The idea of chemical vapor deposition (CVD) is passing a gas over a solid material to obtain a sediment through a chemical reaction. The reactants are put in a gaseous state, where they react through chemical reactions forming solid objects that are then deposited over a substrate. Sol-gel is a chemical solution technique that uses a chemical solution (sol) to produce particles connected together (gel). The starting and

the host material are mixed through stirring, shaking or sonication, to form a gel. After that, filtration, sedimentation and centrifugation are done to recover the nanoparticles (Naikoo et al., 2022). Hydrothermal and solvothermal syntheses are also wet chemical synthesis methods, in which materials are dissolved in an aqueous solution then in an organic solvent under high temperature and pressure. The strength of these two methods lies in the controllability of the surface morphology, and the crystallite size, however, it may require few days, besides the high temperature and pressure could affect the used equipment. In general, bottom-up techniques are useful for synthesizing monolayers but with defects, and CVD is considered to produce a relatively high-quality 2D films at low pressure, with the ability to extend the film size. The synthesis of 2D materials like graphene, BP, and MoS<sub>2</sub>, which are the focus of our study is presented in Figure 12 (Garg et al., 2014; Korotcenkov, 2019; Samy et al., 2021; Samy & El Moutaouakil, 2021). Mechanical and thermal exfoliation of graphite are two major techniques for graphene synthesis but their yield is quite low, besides centrifugation is used to eliminate unexfoliated material (Cai et al., 2012). For large growth and better number of layer control CVD is used. In Liao et al. (2013), hexamethyldisilazane (HMDS) on a SiO<sub>2</sub>/Si substrate is used as a carbon source and the thermally evaporated alternating Ni/Cu/Ni layers are used as a catalyst. Although the graphene layer covered the entire substrate, we have single to tri-layer mixed growth. Mechanical and electrochemical exfoliations were used to obtain thin films (~ 1 layer) and thick film BP in (Dhanabalan et al., 2017; Erande et al., 2016) respectively. The developed layers in (Erande et al., 2016) were checked for field effect transistors, where they have a hole mobility of ~7.3 cm<sup>2</sup>/(V s) and current ON/OFF ratio of ~10<sup>4</sup>. The sensors devices are more sensitive to water vapors and UV light. The grown layers have non-uniform thicknesses, with the majority of layer sizes in the range of 1.4 to 10 nm (3-15 layers). In Smith et al. (2016), researchers were able to obtain large scale (about >3 μm<sup>2</sup>) BP from red phosphorous (which is quite cheaper than BP), with nearly 4 number of layers that can be optimized to a larger scale or less number of layers. By using pulsed layer deposition and BP as a target material we could obtain layer thicknesses ranging from 2 to 8 nm. The method is used to develop a P-type FET with moderate on/off current ratio up to 10<sup>2</sup> and high field-effect mobility up to 14 cm<sup>2</sup> V<sup>-1</sup> s<sup>-1</sup> (Yang et al., 2015). Acoustic

cavitation was used for exfoliation of MoS<sub>2</sub> which resulted in less defective, large 2D nanosheets and 1D nanotubes (Han et al., 2015). A hydrothermal process was able to obtain a single layer of MoS<sub>2</sub> as a stable 2D Metallic-phase MoS<sub>2</sub> (M-MoS<sub>2</sub>) nanosheets in water (Geng et al., 2016). It is highly stable in water and super active for the hydrogen evolution reaction, with a current density of 10 mA cm<sup>-2</sup> at a low potential of -175 mV. A thin film of MoS<sub>2</sub> was grown using CVD with a liquid precursor made by dissolving Mo(CO)<sub>6</sub> in (CH<sub>3</sub>)<sub>2</sub>S<sub>2</sub> where a separate water bubbler is installed to remove the carbon impurities (Choi et al., 2017). Increasing the coverage of MoS<sub>2</sub> could be achieved by simply increasing the growth time. In Kim et al. (2016), a combination of CVD and ALD was used to obtain a thin film of MoS<sub>2</sub> on a large scale. The carrier density of the MoS<sub>2</sub> nanosheets was controlled through the thickness of the promoter layers, which allows the control of the conductivity of MoS<sub>2</sub>.

#### *1.4.8 Previous THz Absorbers*

THz perfect absorber is the focus of recent researches due to its wide applications in sensors, filters, switchers, scanners, energy harvesting, electromagnetic shielding and refractive index sensing (Fan et al., 2021; Viji & Anujan, 2023; Zheng et al., 2021). Narrowband (monochromatic), or multiband, or wideband each has its specific application (Cheng et al., 2016, 2021; El Moutaouakil et al., 2011; Hijazi & Moutaouakil, 2019; Moutaouakil et al., 2009; Moutaouakil, Komori, et al., 2010; Moutaouakil, Suemitsu, et al., 2010; Moutaouakil et al., 2012; Moutaouakil, 2018; Moutaouakil et al., 2020). Perfect absorbers or metamaterial absorbers are characterized by their high absorptivity that could reach 99.9% and are made of more than one material designed in such a way to achieve the highest absorption and the least reflection. They are known for their low cost, high absorptivity, and light weight. Metamaterial absorbers are based on compounds combined with noble metals like gold or silver used as a ground base to achieve high absorptance (Samy et al., 2023). The metallic ground should have a thickness larger than the skin depth to achieve zero transmission while assuring zero reflection by matching the impedance of the structure with the free space impedance (Choi et al., 2017). The basic structure of a metamaterial absorber consists of three layers. A metallic ground with a dielectric substrate on top and a resonator on top of the substrate. The asymmetric absorber based on square rings of Au and Si<sub>3</sub>N<sub>4</sub> has



absorptivity more than 90% (Gong et al., 2016) and a broadband absorption from 4.76 to 5.15 THz. III-V semiconductors are used with gold to achieve perfect metasurface absorber (MSA). A narrow-band perfect absorber based on micro-ring-shaped structure GaAs array and a gold base was proposed in (Cheng et al., 2023). The absorber has ~ 99.9% at 2.213 THz that can be shifted by varying the structure dimensions. InAs nanowires grown over Silicon and covered with gold was able to achieve a maximum absorption of 60% in the infrared range (Kim et al., 2021).

Using the circuit model and the transmission line circuit theory, an Ultra-broadband absorber based on periodic arrays of graphene ribbons has absorptivity of 70% and bandwidth of 5.8 THz (Mohsen Daraei et al., 2020). The bandwidth can be tuned by varying the chemical potential of graphene. Another design based on a frustum-shaped structure of graphene nanoribbons (GNRs), SiO<sub>2</sub>, Au achieved over 90% absorptivity between 0.6 THz and 1.2 THz and near 99% absorptivity between 0.72 THz and 0.9 THz (Dhriti et al., 2022). The absorptance bandwidth can be modulated by varying the spacer thickness of SiO<sub>2</sub>. A narrow band absorber based on graphene layers and gold has a near unity absorptance at 9.8 THz (Chen et al., 2017). The absorptance frequency can be shifted from 6 to 14 THz by varying the chemical potential of graphene while maintaining absorptance larger than 90%.

Black Phosphorous (BP) absorptance is studied in (Xiao et al., 2019) through BP/dielectric layer stacking on gold where the absorption was about 70% at 1 THz. Increasing the carrier concentration through varying the Fermi level causes a blue shift of the absorption frequency with a decrease in absorptance, that goes below 20%. Another design by Wang & Jiang, (2019) based on stacks of BP on gold has absorptivity greater than 90% for a wide band of 6.2 THz (from 3.2 to 9.6 THz) and a narrower bandwidth with absorptivity below 70% that can be tuned through varying the angle of incidence from 0° to 70° in the range of frequencies from 6 to 8 THz. The transmission line model was proposed in Maffucci & Miano, (2013) and Wen et al. (2009) to interpret the absorptivity of metamaterial absorbers. After that, the transmission line circuit theory was used to design perfect absorbers like that proposed for graphene in (Arsanjani et al., 2019; Khavasi, 2015a; Xu et al., 2013) where the Drude model was adopted for graphene nanoribbons and a RLC circuit is used to represent the nanoribbon impedance. Since

selective frequency or narrowband absorbers in the THz range didn't get much attention, they are the focus of this work. Besides, most of the presented work has complex metamaterial design, that results in high-cost fabrication techniques, in addition to the inclusion of gold and other materials that are used to decrease the reflectivity and attain the high absorptivity. Those metamaterial absorbers' dimensions are mostly in the  $\mu\text{m}$  range, and their high absorptivity is limited to a specific bandwidth (Cheng et al., 2023). This work proposes a selective absorber with more than 90% absorptivity through most of the THz spectrum (1.3 THz -10 THz). The bandwidth ranges from 0.9 THz to 1.3 THz which is relatively small when compared to the previous absorbers and could serve as a basis for narrowband absorbers that are required in sensing and enhancement of the electric and magnetic field (Farooq et al., 2022; Luo et al., 2016; Wu et al., 2017; Yong et al., 2016).

Table 1: 2D materials Synthesizing Techniques

Ref.	Material Synthesized	Method	Advantages	Challenges
(Cai et al., 2012)	Graphene	Mechanical Exfoliation	High quality, Low-cost, Time saving.	Poor yield Not for industry
(Liao et al., 2013)	Graphene	CVD	Commercial, High quality, Low cost, Time saving.	Transfer of graphene films to the substrate causes deformation
(Dhanabalan et al., 2017)	BP	Mechanical exfoliation	Low-cost, Time saving.	Non-uniform number of layers across the sample, Can't control the exact number of layers
(Erande et al., 2016)	BP	Electrochemical exfoliation	Few layer nanosheet thick film was used in humidity sensor, and FETs.	Enhance characteristics for field effect transistors mobility of $\sim 7.3 \text{ cm}^2/(\text{V s})$ and current ON/OFF ratio of $\sim 10^4$ Enhance the sensitivity of the developed sensors

Table 1: 2D materials Synthesizing Techniques (continued)

Ref.	Material Synthesized	Method	Advantages	- Challenges
(Smith et al., 2016)	BP	CVD	Used red phosphorous, Large area >3 $\mu\text{m}^2$ about 4 layers.	- Increase the area of growth - Obtain less number of layers
(Yang et al., 2015)	BP	Pulsed layer deposition	Obtained thickness 2 to 8 nm. Used to develop a P-type FET.	- Used bulk BP as a target (expensive) - Enhance the FET characteristics
(Han et al., 2015)	MoS <sub>2</sub>	Liquid exfoliation using Ultrasonic cavitation	less defective, large 2D nanosheets or 1D nanotubes	N/A
(Kim et al., 2016)	MoS <sub>2</sub>	ALD & CVD	Controlling the conductivity of MoS <sub>2</sub>	Complex methodology
(Geng et al., 2016)	MoS <sub>2</sub>	Hydrothermal	Pure and stable M-MoS <sub>2</sub> , stable in water, super active for HER.	Metallic phase MoS <sub>2</sub> has to be studied for more applications
(Choi et al., 2017)	MoS <sub>2</sub>	CVD	full-coverage of MoS <sub>2</sub> film for large area used liquid precursor	- Complex set up - Have impurities

## Chapter 2 : Methods

### 2.1 Theoretical Approach

This work aims to investigate some of the properties of graphene, phosphorene, and MoS<sub>2</sub>, mainly their absorption under THz excitation. According to their properties, we propose a structure with high absorptivity and simple design. We have to identify the refractive index of these materials in case of THz frequency excitation. As discussed in Chapter 1, Equations (1.4)-(1.8), the electric permittivity is directly related to the refractive index ( $n$ ) and the extinction coefficient ( $\kappa$ ). In this case, we are talking about a complex permittivity  $\epsilon(\omega)$  that has real and imaginary parts and depends on the angular frequency of the incident wave  $\omega$ . The equation of the complex permittivity is also related to the optical conductivity  $\sigma$  of materials. In the next sections, we are going to discuss the optical permittivity and conductivity of the materials used in our structure. There are two main transitions that affect the optical conductivity of a semiconductor material; the intra-band transitions which occur in the same energy band and inter-band transitions that occur between two different energy bands. The band gap of the material and the nature of the incident wave determines the kind of transitions that occurs in the material.

#### 2.1.1 The Dielectric Function of Plasma (Free Electron Gas)

The electromagnetic response of materials can be described through the macroscopic Maxwell Equations (2.1)-(2.4). When dealing with continuous media, such as materials composed of a vast number of atoms or molecules, the behavior of individual particles doesn't fully describe the electromagnetic properties of the whole material. Instead, we need a macroscopic description that takes into account the collective behavior of these particles (plasma). One more advantage of using Maxwell's equations is it can be easily simulated using the finite element method (FEM). The plasma oscillations (sea of electrons on the surface) in 2D materials like graphene, MoS<sub>2</sub>, and phosphorene govern the frequency response of these materials, that's why we needn't take into account the interactions between carriers in each atom.

$$\nabla \cdot D = \rho_{ext} \quad (2.1)$$

$$\nabla \cdot B = 0 \quad (2.2)$$

$$\nabla \times E = -\frac{\partial B}{\partial t} \quad (2.3)$$

$$\nabla \times H = J_{ext} + \frac{\partial D}{\partial t} \quad (2.4)$$

where  $D$  is the dielectric displacement,  $E$  is the electric field,  $H$  is the magnetic field, and  $B$  is the magnetic flux density,  $\rho_{ext}$  is the external charge and  $J_{ext}$  is the external current density. Equations (2.5), and (2.6) relate the four macroscopic fields  $E, D, H,$  and  $B$  through the polarization  $P$  and magnetization  $M$ . In our study, we will not consider the magnetic effects and we don't have a magnetic source, so we will neglect the effect  $M$  and only Equation (2.5) is considered.

$$D = \epsilon_0 E + P \quad (2.5)$$

$$H = \frac{1}{\mu_0} B - M \quad (2.6)$$

where  $\epsilon_0$  is the vacuum electric permittivity, taken as  $8.854 \times 10^{-12}$  F/m, and  $P$  is the electric dipole moment per unit volume inside the material, caused by the alignment of microscopic dipoles with the electric field. The current density  $J$  and the electric dipole moment per unit volume inside the material ( $P$ ) are related through:

$$J = \frac{\partial P}{\partial t} \quad (2.7)$$

$t$  is the time in seconds. Indeed, a proper definition of  $P$  makes Maxwell's equations safely applied in plasmonics (Solis et al., 2015; Mansuripur & Zakharian, 2009). The above assumption of polarization  $P$  assumed that  $\omega \gg \omega_p$  which is the natural frequency of a free oscillation of the electron sea or plasma. When the excitation frequency  $\omega$  is comparable to  $\omega_p$  or  $\omega > \omega_p$  intrer-band transitions occur, and the previous model needs to be modified. In this case, the response is dominated by free s electrons where the filled d band close to the Fermi surface causes an increase in polarization and a polarization  $P$  needs an additional term  $P_\infty$ . This extra polarization that is due to the positive background of the ion cores, can be described as

$$P_{\infty} = \epsilon_o(\epsilon_{\infty} - 1)E \quad (2.8)$$

And in this case, Equation (2.5) is re-written as:

$$D = \epsilon_o E + P + P_{\infty} \quad (2.9)$$

Which will transform to (2.10) after substituting (2.8) in (2.9)

$$D = \epsilon_o \epsilon_{\infty} E + P \quad (2.10)$$

$\epsilon_{\infty}$  is the dielectric constant or relative permittivity when  $\omega \rightarrow \infty$  or when  $\omega$  is well above  $\omega_p$ , (Matthaiakakis et al., 2016; Maier, 2007). Since the optical response depends on frequency, we have to account for both time and space through the following equations

$$D(K, \omega) = \epsilon_o \epsilon(K, \omega) E(K, \omega) \quad (2.11)$$

$$J(K, \omega) = \sigma(K, \omega) E(K, \omega) \quad (2.12)$$

where  $K$  is the wave vector. Also, the current density in (2.7) can also be represented in the frequency (Fourier) domain as

$$J(K, \omega) = -i\omega P(K, \omega) \quad (2.13)$$

Substituting (2.10) in (2.11) and (2.12) in (2.13) we get (2.14), and (2.15) that are easily transformed to (2.16) and (2.17) respectively as follows:

$$\epsilon_o \epsilon_{\infty} E(K, \omega) + P(K, \omega) = \epsilon_o \epsilon(K, \omega) E(K, \omega) \quad (2.14)$$

$$-i\omega P(K, \omega) = \sigma(K, \omega) E(K, \omega) \quad (2.15)$$

$$P(K, \omega) = \epsilon_o \epsilon(K, \omega) E(K, \omega) - \epsilon_o \epsilon_{\infty} E(K, \omega) = \epsilon_o E(K, \omega) (\epsilon(K, \omega) - \epsilon_{\infty}) \quad (2.16)$$

$$P(K, \omega) = \frac{\sigma(K, \omega) E(K, \omega)}{-i\omega} \quad (2.17)$$

By dividing (2.17)/(2.16) to get a relation between  $\epsilon(K, \omega)$  and  $\sigma(K, \omega)$  as in (2.20)

$$1 = \frac{\sigma(K, \omega) E(K, \omega)}{-i\omega} \times \frac{1}{\epsilon_o E(K, \omega) (\epsilon(K, \omega) - \epsilon_{\infty})} \quad (2.18)$$

Simplifying (2.18) we get

$$\epsilon(K, \omega) - \epsilon_\infty = \frac{\sigma(K, \omega)}{-i\omega\epsilon_o} \quad (2.19)$$

Then we have the complex permittivity equation as:

$$\epsilon(K, \omega) = \epsilon_\infty + \frac{i\sigma(K, \omega)}{\epsilon_o\omega} \quad (2.20)$$

The dielectric response  $\epsilon(K, \omega)$  can be represented by a spatially local response where  $\epsilon(K, \omega) = \epsilon(\omega)$ . This model is valid as long as the incident wave have a wavelength  $\lambda$  longer than the size of the unit cell or the mean free path of the electrons, then we can write the permittivity equation as:

$$\epsilon(\omega) = \epsilon_r + \frac{i\sigma(\omega)}{\epsilon_o\omega} \quad (2.21)$$

Where  $\epsilon_\infty$  can be substituted by  $\epsilon_r$ , the background or the static permittivity of the material as in (Matthaiakakis et al., 2016; Chi Kao, 2004).

### 2.1.2 Intra-band and Inter-band Transitions

The dielectric function  $\epsilon(\omega)$  of a plasma, is described through a plasma model where a gas of free electrons of number density  $N$  moves against a fixed background of positive ion cores. There are two approaches according to the kind of plasma transitions. The first one is when we have transitions in the same band only (intra-band transitions) and the second one is when we have a dominating band to band transitions (inter-band transitions). A simple equation of motion can describe the motion of an electron in the plasma with mass  $m$  and under the effect of external electric field  $E$ . In case of intra-band transitions the equation has the form (2.22).

$$m^*\ddot{x} + \frac{m^*\dot{x}}{\tau} = -qE \quad (2.22)$$

This is known as Drude model of the free electron gas, where  $x$  is the displacement of the electron with respect to its rest position ( $\dot{x}$  and  $\ddot{x}$  represent the first and second time derivatives, respectively),  $q$  is the electronic charge taken as  $1.6 \times 10^{-19} C$ ,  $m^*$  is its effective optical mass, and  $\tau$  is the relaxation time of the free electron gas in seconds.

Solving the above differential equation and after some substitutions we get an equation of  $\epsilon(\omega)$  (Maier, 2007), which is similar to Equation (2.21), from which we get the optical conductivity  $\sigma$  defined as:

$$\sigma = \frac{iq^2N}{m^*(\omega + i\tau^{-1})} \quad (2.23)$$

Where  $N$  is the number density of the free electron gas. Equation (2.23) represents the Drude model optical conductivity that we will use later in our model.

In case of higher frequencies, inter-band transitions take place, where we have transitions from lower bands to the conduction band, Drude model is no longer sufficient and the equation of motion has to be modified, where the inter-band transitions are described using the classical view of a bounded electron with resonance frequency  $\omega_o$ ,

$$m^*\ddot{x} + \frac{m^*\dot{x}}{\tau} + m^*\omega_o^2x = -qE \quad (2.24)$$

To solve the above equation for  $\epsilon(\omega)$ , we need to solve several of these equations, each equation yielding a separate polarization that translates into a Lorentz-oscillator term as in (2.25) and this term is to be added to the  $\epsilon(\omega)$  equation of the Drude model in (2.21).

$$\frac{A_i}{\omega_{0,i}^2 - \omega^2 + j\gamma_i\omega} \quad (2.25)$$

where  $\omega_{0,i}$  and  $\gamma_i$  are the plasma and the damping frequencies for the bound electrons, and  $A_i$  is a parameter that weights the contribution of the  $i$ -th inter-band transition to the dielectric function. Sometimes solving the Lorentz term could be a little complicated and we use other formulas to reach a solution like in case of Kubo formula that is used to solve for the optical conductivity of graphene.

### 2.1.3 Optical Conductivity of Graphene (Kubo Formula)

Graphene is a zero-band gap material that is mainly managed by intra-band transitions (Popov et al., 2010a). However, the proposed case in this study is different, since the band gap of graphene is opened by different means like stripping it into nanoribbons and applying a vertical gate voltage, beside using a heterostructure with MoS<sub>2</sub>. All these factors affects the band gap of graphene and opens a small band gap



which requires including inter-band transitions (Han et al., 2007), besides the inter-band transitions could not be neglected at low chemical potential in the THz range (Wang et al., 2020). The complex optical conductivity of graphene including both intra-band and inter-band transitions is represented by the Kubo formula represented by the Equations (2.26), and (2.27) (Hanson, 2008; Gollapalli et al., 2022).

$$\sigma_{intra}(\omega) = i \frac{q^2}{\pi \hbar^2 (\omega + i\tau^{-1})} \times \left( \mu_c + 2K_B T \times \ln \left( e^{-\frac{\mu_c}{K_B T_0}} + 1 \right) \right) \quad (2.26)$$

$$\sigma_{inter}(\omega) = i \frac{q^2}{4\pi \hbar} \ln \frac{2|\mu_c| - \hbar(\omega + i\tau^{-1})}{2|\mu_c| + \hbar(\omega + i\tau^{-1})} \quad (2.27)$$

$$\sigma_{total}(\omega) = \sigma_{intra}(\omega) + \sigma_{inter}(\omega) \quad (2.28)$$

The total conductivity is calculated as the sum of inter-band and intra-band conductivity.  $\hbar$  is the reduced Planck's constant ( $h/2\pi$ ),  $\omega$  is the angular frequency,  $K_B$  is Boltzmann constant,  $T$  is the temperature in Kelvin,  $\mu_c$  is the chemical potential, and  $\tau$  is the momentum relaxation time, defined as

$$\mu_c = \hbar v_f \sqrt{\pi n_g} \quad (2.29)$$

$$\tau = \frac{\mu_c m_u}{q v_f^2} \quad (2.30)$$

and  $v_f$  is the Fermi velocity taken as  $10^6$  m/s,  $m_u$  is the impurity-limited direct current mobility taken as  $1 \text{ m}^2 \cdot \text{s}/\text{V}$ , and  $n_g$  is the carrier concentration of graphene and is defined by a simple capacitor model as:

$$n_g = \frac{V_g \epsilon_o \epsilon_{r-sub}}{q d_{sub}} \quad (2.31)$$

Where  $\epsilon_{r-sub}$  is the relative substrate permittivity, and  $d_{sub}$  is the substrate thickness, and  $V_g$  is the vertical applied voltage. In case of a heterostructure of graphene and MoS<sub>2</sub>, we adopt a capacitor model for the charge concentration of graphene (2.32)

$$n_g = \frac{V_g \epsilon_0}{q \left( \frac{d_{MoS_2}}{\epsilon_{MoS_2}} + \frac{d_{Gr}}{\epsilon_{Gr}} \right)} \quad (2.32)$$

Where  $d_{MoS_2}$ ,  $d_{Gr}$  are the monolayer MoS<sub>2</sub> and graphene thicknesses taken as 0.65 nm and 0.34 nm respectively and  $\epsilon_{MoS_2}$ ,  $\epsilon_{Gr}$  are the static relative permittivities of MoS<sub>2</sub> and graphene taken as 3.7 and 5.6 respectively.

#### 2.1.4 Optical Conductivity of MoS<sub>2</sub> and Phosphorene (Drude Model)

Monolayer MoS<sub>2</sub> has a wide band gap of 1.9 eV with respect to THz waves (maximum energy  $\sim$  40 meV) that makes it hard for inter-band transitions to occur for such frequencies. Inter-band transitions occur when the incident field is in the visible spectrum region or higher frequencies (Dou et al., 2014; Li et al., 2016; Tao et al., 2019). In the THz range monolayer MoS<sub>2</sub> is dominated by the intra-band transitions that is represented by the Drude model (2.23), we modify it here for MoS<sub>2</sub> as (2.33)

$$\sigma_{MoS_2} = \frac{iq^2 n_{MoS_2}}{m_{MoS_2}^* (\omega + i\tau^{-1})} \quad (2.33)$$

Where  $n_{MoS_2} = 1.2 \times 10^{12} \text{ cm}^{-2}$  is the carrier concentration of undoped (intrinsic) monolayer MoS<sub>2</sub> and  $m_{MoS_2}^* = 0.53 \times m_e$  is the effective mass of MoS<sub>2</sub>,  $m_e$  is the electron mass taken as  $9.1 \times 10^{-31} \text{ Kg}$ ,  $\tau = 0.17 \times 10^{-12} \text{ s}$  is the carrier relaxation time (Chen et al., 2016; Dagan et al., 2019). The complex permittivity of MoS<sub>2</sub> ( $\epsilon'_{MoS_2}$ ) is then calculated according to equation

$$\epsilon'_{MoS_2} = \epsilon_{MoS_2} + \frac{i\sigma_{MoS_2}}{\epsilon_0 \omega d_{MoS_2}} = \epsilon_{real} + i\epsilon_{imag} \quad (2.34)$$

$\epsilon_{real}$  and  $\epsilon_{imag}$  are the real and imaginary parts of MoS<sub>2</sub> permittivity as defined in chapter 1 in Equations (1.4), and (1.5). The refractive index can then be extracted as in Equations (1.6), and (1.7).

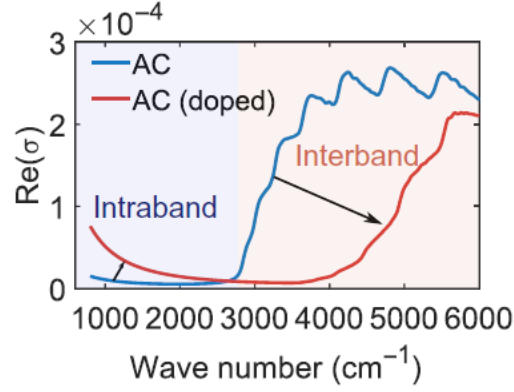


Figure 13: The real part of optical conductivity of BP in the AC direction in case of doped and undoped BP (Biswas et al., 2021). Reproduced with permission. Science advances 2021.

The optical conductivity of phosphorene can also be represented by the Drude model like MoS<sub>2</sub>, since for THz frequencies, only intra-band transitions are the dominating ones (Biswas et al., 2021; Phuong et al., 2020; Zhou et al., 2018) and inter-band transitions are taken into account in some specific cases like when considering the spin-splitting effects which is not considered in our study. The inter-band and intra-band transitions of BP were compared in Biswas et al. (2021) using the Kubo formula and the result showed the domination of the intra-band transitions in the THz range Figure 13. Below the wave number 3000  $cm^{-1}$  which is equivalent to frequencies less than 14 THz, intra-band is dominating inter-band transitions for undoped BP which is our case. In contrast to MoS<sub>2</sub>, Phosphorene is highly anisotropic and is greatly affected by a vertical applied electric field. The optical conductivity of MLBP  $\sigma_{BP}$  is represented according to the Drude model as:

$$\sigma_{BP} = \frac{iD}{\pi \left( \omega + \frac{i\eta}{\hbar} \right)} \quad (2.35)$$

$\sigma_{BP}$  is the optical conductivity of MLBP, D is the Drude weight in the armchair (AC) or zigzag (ZZ) direction, and  $\eta$  (eV) is a parameter related to the scattering rate and is taken as 10 meV in almost all previous literatures (Phuong et al., 2020; Biswas et al., 2021; Zhou et al., 2018). In case of MLBP the Drude weight (D) can't be considered as a constant value like MoS<sub>2</sub> because the carrier concentration is greatly affected by the vertical applied voltage.

$$D = \frac{\pi q^2 n_{AC/ZZ}}{m_{AC/ZZ}^*} \quad (2.36)$$

Where  $n_{AC/ZZ}$  and  $m_{AC/ZZ}$  are the carrier concentration and the effective mass of phosphorene in the armchair (AC) or zigzag (ZZ) directions respectively. The carrier concentration in MLBP is calculated according to (2.37)

$$n_{AC/ZZ} = m_{AC/ZZ}^* \frac{K_B T}{d_{BP} \pi \hbar^2} \ln \left( 1 + e^{\frac{\mu_{BP}}{K_B T}} \right) \quad (2.37)$$

$d_{BP}$  and  $\mu_{BP}$  are the phosphorene thickness and chemical potential, respectively. The effective mass is taken as  $0.15 \times m_e$ . Previous literature showed that the armchair direction has the lowest effective mass, usually taken as  $0.15 \times m_e$  (Debu et al., 2018; Qiao et al., 2014), but the band gap calculations in Cao et al. (2016), showed that a critical electric field can reverse the situation, where the zigzag direction is the one with the lowest effective mass Figure 14a. In MLBP we are in front of two interesting phenomena, and both are related to applying a vertical electric field. The first one is related to the anisotropy of BP and how the vertical electric field causes a kind of stress and deformation in the band gap structure and reverses the direction of lower effective mass (Cao et al., 2016) Figure 14a. So, BP is not only anisotropic when excited with an in-plane electric field (whether in the AC or the ZZ directions) but also a vertical electric field affects its conductivity. The second phenomena is the change of the band gap from a semiconductor to a Dirac semi-metal and finally an inverted (negative band gap) (where electrons are free to move from the valence band (VB) to the conduction band (CB)) (Kim et al., 2015; Lin et al., 2016). The puckered structure of MLBP uncovers some interesting properties. Its band structure has one valence band maximum (VBM) and two conduction band minimum (CBM1 and CBM2). The electron effective mass (EEM) in the ZZ direction is greater than the AC for CBM1 and vice versa for CBM2. A vertical electric field can also change the EEM. The study in (Cao et al., 2016) Figure 14b, c, and d showed how the conduction bands structure is changed under the effect of a vertical electric field that results in a complete reverse for the EEM to where the ZZ direction becomes the one with the least effective mass taken as  $0.15 \times m_e$ . So, BP is not only highly anisotropic by its nature, but also this anisotropy is affected by the electric field.

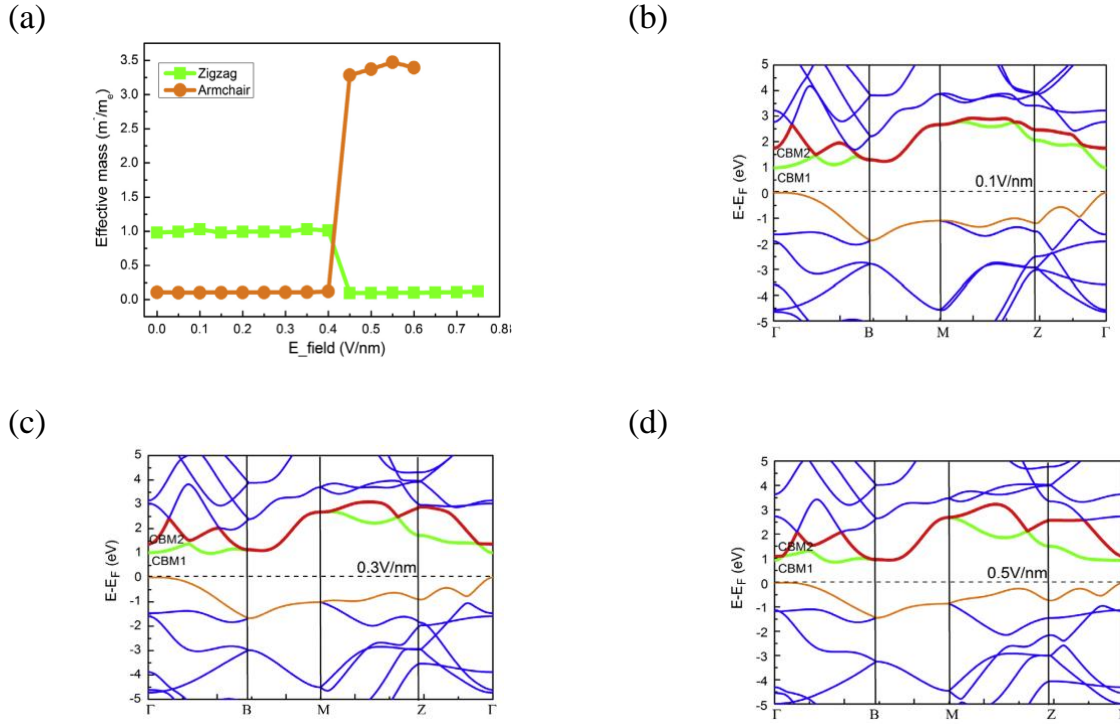


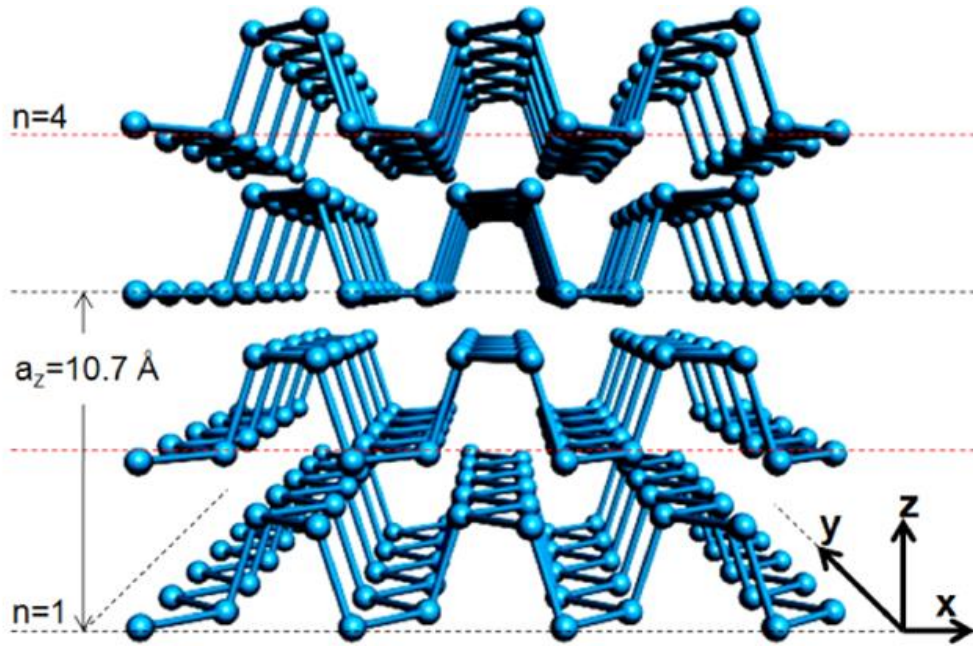
Figure 14: The effect of applying a vertical electric field on monolayer BP

(a) The effective mass versus the electric field (V/m); (b), (c), (d) The band gap ( $E - E_F$ ) at different electric field values 0.1, 0.3, 0.5 V/nm, showing the variations in CBM1 and CBM2. Adapted from (Cao et al., 2016). Computational Materials Science, Elsevier 2016.

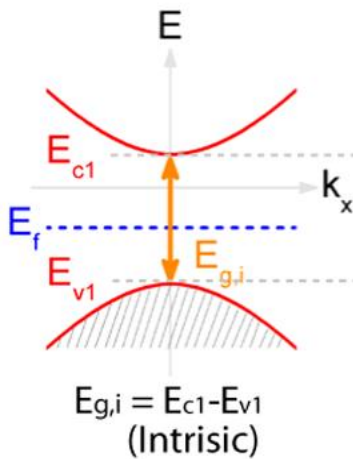
The second interesting property is the change of BP from a semiconductor to a Dirac semi-metal or to a material with a negative band gap (inverted band gap) under the effect of electric field. Two approaches discussed the band gap changes that happens to BP, one of them included the effect of an external vertical field (electrical doping) and the other presented a chemical doping (donor atoms), and both of them reached the same findings which is the decrease in the band gap of BP until it reaches zero then increases again in the form of a negative or inverted band gap. The research in (Lin et al., 2016) discussed the three material states for a four layer BP in details and related it to the vertical applied electric field and the carrier concentration Figure 15. When applying an electric field, the Fermi level shifts up and the conduction band shifts down, while the motion of the valence band ( $E_{v1}$ ) is nearly negligible Figure 15c, d, and e. The fermi level ( $E_f$ ) keeps shifting up while the conduction band ( $E_{c1}$ ) shifts down until BP reaches a zero-band gap ( $E_g = 0$ ) and then inversion occurs. The approach in (Lin et al., 2016), assumes the motion of the Fermi level upwards crossing the conduction band as

the inversion occurs. The same issue was discussed in Cao et al. (2016), stating that an electric field  $>0.45$  V/nm ( $\sim 0.32$  V for monolayer thickness of 0.7 nm) can decrease the band gap and that at an electric field of 0.8 V/nm, the material changes to a semi-metal and at an electric field  $> 0.8$  V/nm the band inversion occurs. The approach by Kim et al. (2015), manifests that this band gap variation occurs whether through chemical doping by adding donor atoms like potassium or electrical doping (applied negative voltage). The doping affects the bandgap on both the ZZ and the AC directions with a linear band dispersion in the AC direction and a quadratic dispersion in the ZZ Figure 16c. At very low doping level, the overall band structure shifts down, the conduction band minimum ( $\Gamma_4^-$ ) and the valence band maximum ( $\Gamma_2^+$ ) also shifts down with no significant change in the band gap. When increasing the doping (vertical electric field) below the critical value, the band gap decreases, the band calculations assumes that the Fermi level doesn't change its position Figure 16c and both conduction and valence bands moves in opposite directions. After the band gap reaches zero the conduction band shifts down the Fermi level resulting in the inversion band gap. This is interpreted as Stark effect where the energy bands splits allowing for more energy states up and down the energy band. The experimental approach by Kim et al. (2015) shows that actually all the energy levels (CB, VB, and Fermi level) are moving together which is probably more accepted.

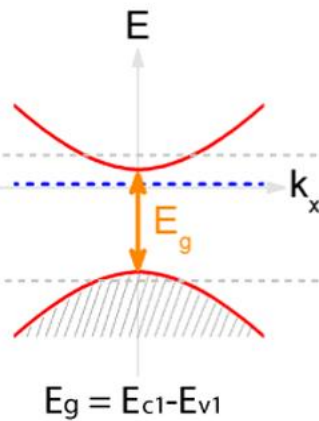
(a)



(b)



(c)



(d)

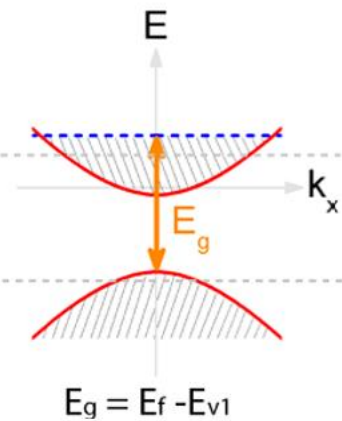


Figure 15: The effect of a vertical applied field on four layers BP.

(a) The four layer structure of BP that is used; (b) the band gap at no applied voltage with carrier concentration  $1.4 \times 10^{10} \text{ cm}^{-2}$ ; (c) The band gap when applying voltage (the band gap decreases, as  $E_{c1}$  gets down and  $E_{v1}$  gets up) with carrier concentration  $1 \times 10^{12} \text{ cm}^{-2}$  (d) The band gap after increasing the applied voltage (a case of band inversion) with carrier concentration  $5 \times 10^{12} \text{ cm}^{-2}$ . Adapted from (Lin et al., 2016). Nano letters, ACS 2016.

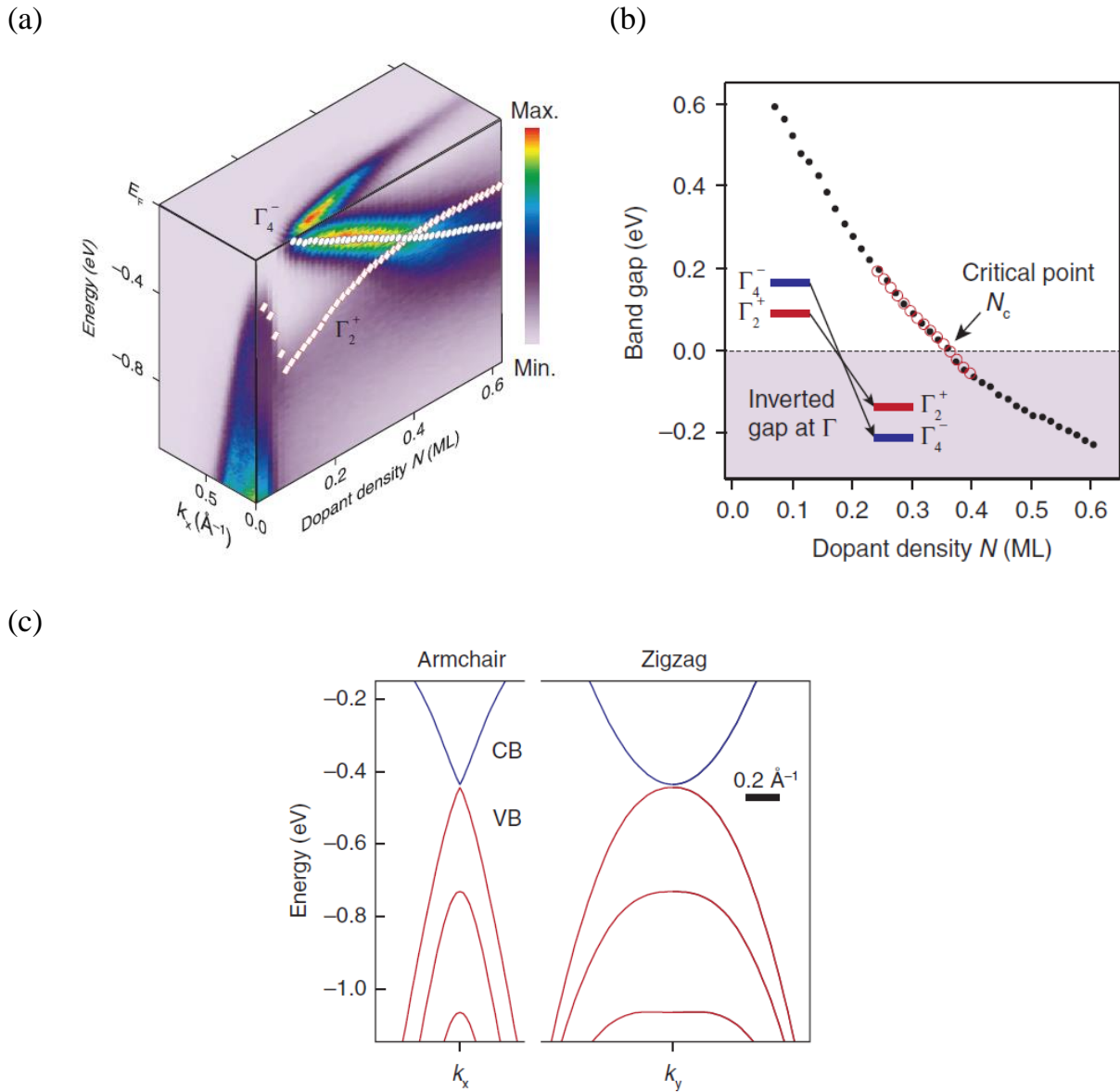


Figure 16: The effect of increasing the dopant density on the band gap of four-layer BP.

(a) A 3D evaluation of the band gap; (b) The band gap versus the dopant density showing the critical dopant density that causes a zero- band gap ( $\Gamma_2^+$  for the maximum of valence band and  $\Gamma_4^-$  for the minimum of the conduction band); (c) The energy gap in (eV) versus the wave number  $k_x$  for AC direction and  $k_y$  for the ZZ direction. Adapted from (Kim et al., 2015). 2D materials, Science 2015.

The band gap of BP is related to the number of layers, where the band gap increases with the decrease in the thickness of BP, and the highest band gap occurs for MLBP. The critical field or the critical dopant density that achieves a zero-band gap in BP is less for a greater number of layers of BP because the band gap decreases with increasing the number of layers Figure 17.



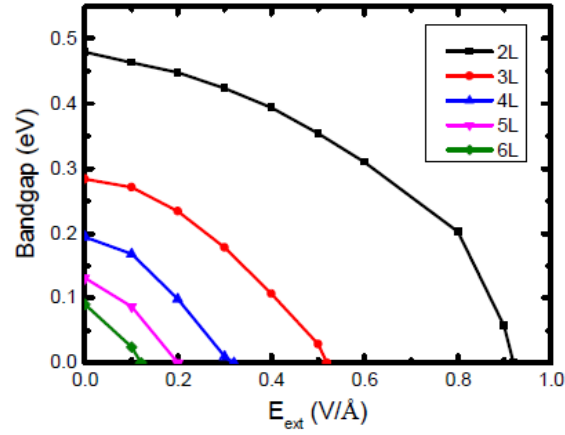


Figure 17: The band gap (eV) versus the external electric field  $E_{\text{ext}}$  (V/Å) for BP. Adapted from (Kumar et al., 2016). Physical review B 2016.

### 2.1.5 The Operating Point of Phosphorene

Based on the literature in the previous section we want to specify the required band gap of phosphorene that we will work at. According to the DFT calculations by Cao et al. (2016), an equation for the band gap is estimated and plotted in Figure 18.

$$E_g = -0.04233 e^{8.757|V_{BP}|} + 0.9782 e^{0.974|V_{BP}|} \quad (2.38)$$

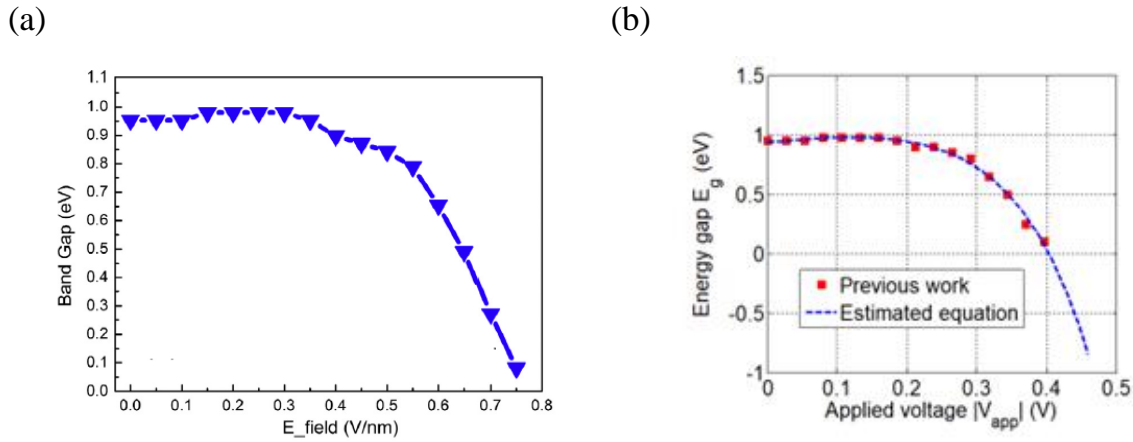


Figure 18: The effect of applied voltage on the band gap of monolayer phosphorene

(a) The band gap (eV) of MLBP versus the vertical applied field ( $E_{\text{Field}}$  (V/m)). Adapted from (Cao et al., 2016). Computational Materials Science, Elsevier 2016; (b) The band gap ( $E_g$ ) of MLBP versus the absolute voltage applied  $|V_{\text{app}}|$ . The square points are from the calculations by Cao et al. (2016) compared with the fitted Equation in (2.38) (dashed line).

There is a strong relation between the band gap and the chemical potential. Figure 19 shows the variation of the band gap of BP as discussed in the previous section. If we defined the chemical potential to be the difference between the Fermi level and the CBM  $\mu = E_F - E_c$  and we took  $E_F$  as the reference zero level we can easily relate the chemical potential to the energy of the band gap as in Figure 19a. Similar approaches were previously adopted in literature as in (Fang et al., 2007a; Low et al., 2014). In Figure 19b, the band gap decreases with increasing the applied electric field, a case of zero band gap occurs at the critical electric field letting  $E_c$ ,  $E_F$  and  $E_v$  coincide. After that, the band gap begins to increase again Figure 19c. We choose our operating point to be exactly after the inversion occurs where  $E_F$  migrate above the  $E_c$  and  $E_c$  is still very near to  $E_v$ . The chemical potential  $\mu$  can then be approximated to the value of the band gap. By knowing the applied voltage applied to BP we get the energy gap  $E_g$  from (2.38) which is the same as the chemical potential  $\mu_{BP}$  value, to be substituted in (2.37).

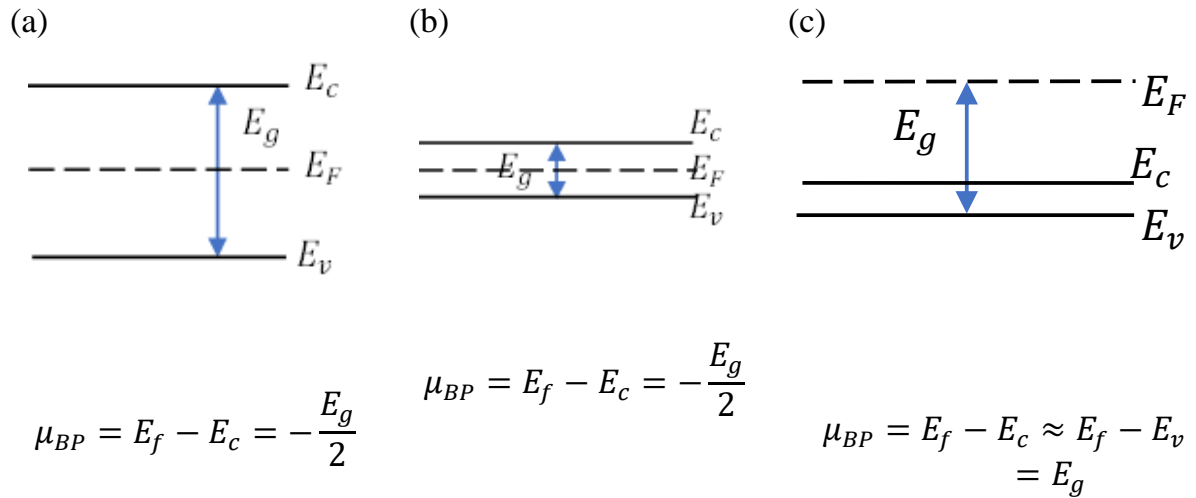


Figure 19: The variation of the band gap of MLBP under the effect of electric field (a) The intrinsic case, no electric field, (b) Energy gap decreases under an electric field less than the critical value (c) Energy gap starts to increase again after reaching zero (Lin et al., 2016).

## 2.1 Modeling and Simulation

In this section we will discuss the design of our proposed structure, the steps taken to reach the final design (model), and the simulation methods used. Simple structures were first proposed containing one or two materials only (like graphene only or phosphorene only). By investigating the simulation results of these simple structures

and the previous literature, we were able to modify the structure to the final one that contains graphene, MoS<sub>2</sub>, and phosphorene. One of the computational methods to solve for partial differential equations (PDEs) like the one from (2.1) to (2.4) for different structures is the FEM or the finite element analysis (FEA). The basis of the FEM is to simplify structures and problems, that require solving PDEs and are difficult to solve analytically. There has to be a kind of approximation, where the structure is segmented into small elements (discretized) and the PDEs can be approximated to numerical model equations, that are solved numerically. These numerical solutions are approximation of the real PDEs solution (Comsol, 2017; Liu, 2019). In order to find a traveling-wave solutions of Maxwell's equations in the absence of external effect, we combine the curl Equations (1.3), and (1.4) to get the wave Equations (2.39) and (2.40) in time and frequency domain, respectively.

$$\nabla \times \nabla \times E = -\mu_0 \frac{\partial^2 D}{\partial t^2} \quad (2.39)$$

$$K(K.E) - K^2 E = -\epsilon(K, \omega) \frac{\omega^2}{c^2} E \quad (2.40)$$

The electromagnetic wave module (frequency domain) in COMSOL Multiphysics is used, which solves Equation (2.39) using the FEM. The plasma waves and the external applied field are taken into consideration through the permittivity Equation in (2.21) for each material that accounts for intra-band and inter-band transitions through the Drude model and the Kubo formula of optical conductivity in Equations (2.33), and (2.35) for MoS<sub>2</sub> and BP and (2.28) for graphene. The values of the complex refractive index of graphene, MoS<sub>2</sub>, and MLBP are extracted from Equations (2.28), (2.33), and (2.35) respectively by first solving for  $\epsilon(\omega)$  for each as in (2.20) then solving for  $n$  and  $\kappa$  as in (1.6), and (1.7) respectively. For h-BN the built-in function in COMSOL for thin h-BN was used that is described by  $n^2 - 1 = \frac{3.263 \times \lambda^2}{\lambda^2 - 0.1644^2}$  where  $\lambda$  is the wavelength of the incident wave. The equation matches the results in (Laturia et al., 2018; Naftaly et al., 2011; Satawara et al., 2021). For SiO<sub>2</sub> a real refractive index is taken as an average value of 2.15 in the THz region as described in (Davies et al., 2018).

### 2.2.1 Structure and Design

Several structures were examined for their absorption until we reached our final structure that have graphene, MoS<sub>2</sub>, and phosphorene. Since we are considering the fabrication of the reached design. We focused to have the simplest structure that can achieve the highest absorption. According to the discussion in chapter 1, we chose a simple nanoribbon design that can open the band gap of graphene and allow for THz absorption. We also examined the absorption of MoS<sub>2</sub>, phosphorene nanoribbons solely. The nanoribbons are placed over SiO<sub>2</sub> and coated with h-BN. The wave excitation is in the vertical direction, normally incident to the nanoribbons with an electric field in the direction of the nanoribbon width. Figure 20, represents a 2D view for a unit cell of the base structure that was used to simulate nanoribbons of graphene, MoS<sub>2</sub>, and phosphorene each one separately. The structure is repeated to the left and the right to form an infinite array of nanoribbons. 2D structure simulation was used where the infinite extension of the nanoribbon is in the third dimension (inwards) and a Floquet periodic boundary condition is applied in the horizontal direction to guarantee the periodic infinite repetition of the whole structure horizontally so we have an infinite number of nanoribbons with the same boundary conditions (Hakoda et al., 2018) . We varied the structure parameters like the spacing between the nanoribbons  $d$ , the width of the nanoribbon  $W$  and the applied voltage  $V_{app}$  to reach a good absorption in the THz range. According to the dimensions and conditions reached for each standalone structure, a heterostructure of MoS<sub>2</sub>/graphene was proposed and examined where the absorption was still not more than 50%. We made use of the in-plane structure of graphene and phosphorene together with the heterostructure of MoS<sub>2</sub>/graphene and we obtained good results.

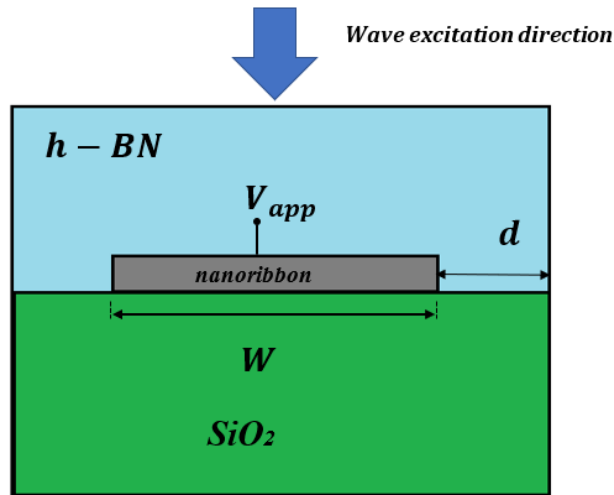


Figure 20: A 2D schematic of a unit cell of the array of infinite nanoribbons. The structure is used for graphene, MoS<sub>2</sub> and phosphorene nanoribbons.

### 2.2.2 Graphene and MoS<sub>2</sub> Heterostructure

The design is based on opening the band gap of graphene using different methods. We applied three factors that open the band gap which are stripping graphene into nanoribbons, developing a heterostructure with MoS<sub>2</sub> and applying a vertical gate voltage. The dimensions of the structure ( $W_n$ , and  $d$ ) are modulated to have absorptance in the THz region. The electromagnetic field excitation is in the vertical direction (-y) with a zero angle with the vertical plane (normal incidence) with an electric field  $E_x$  polarized in the x direction. Figure 21, shows the proposed structure with a nanoribbon width  $W_n$  and applied vertical gate voltage  $V_g$  and a spacing  $d$  between the nanoribbons.

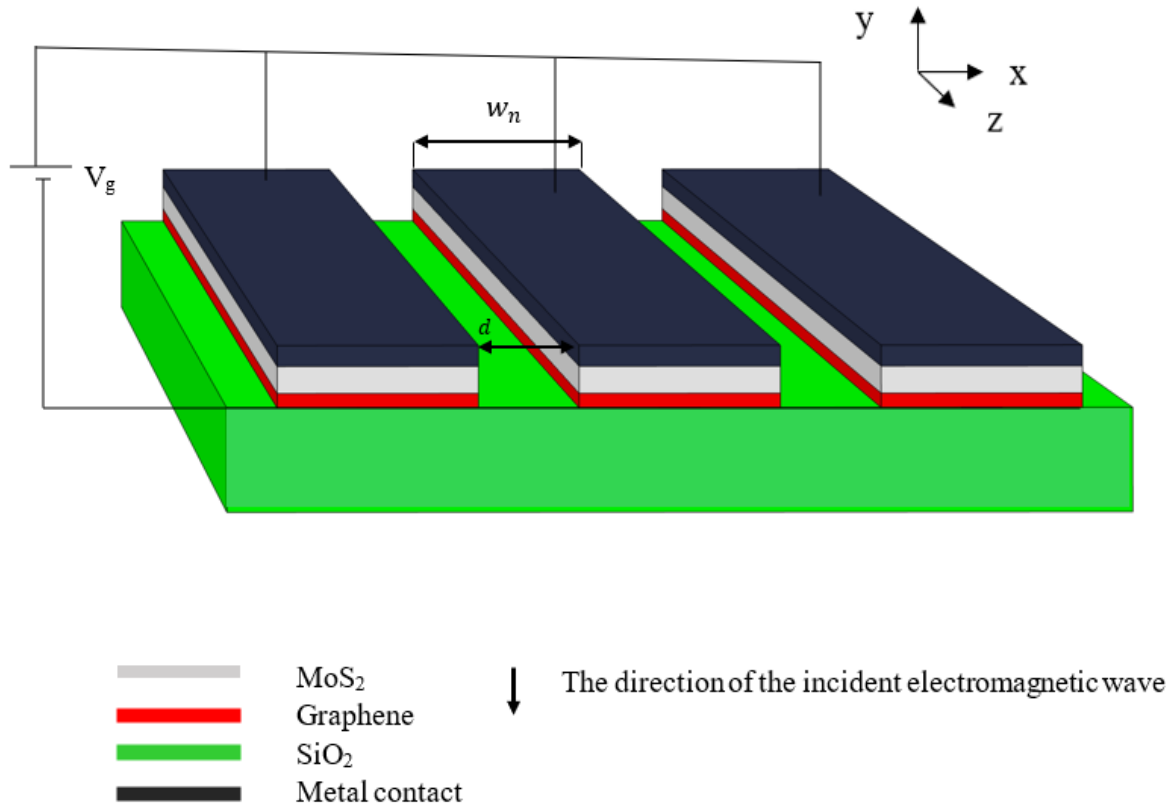
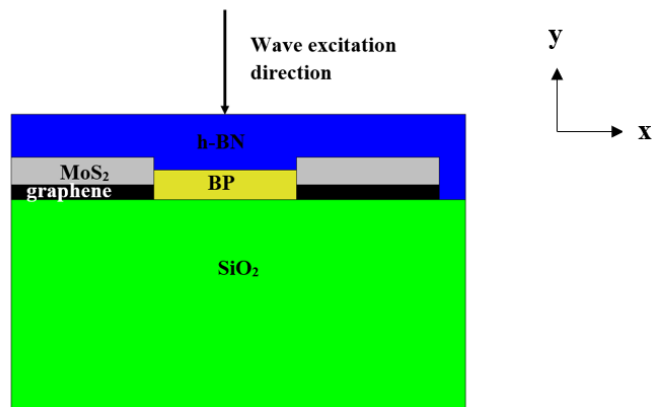


Figure 21: The schematic of the infinite nanoribbon structure with a SiO<sub>2</sub> substrate and nanoribbons of graphene and MoS<sub>2</sub> with applied gate voltage  $V_g$  and incident THz electromagnetic wave (not to scale for clarification).

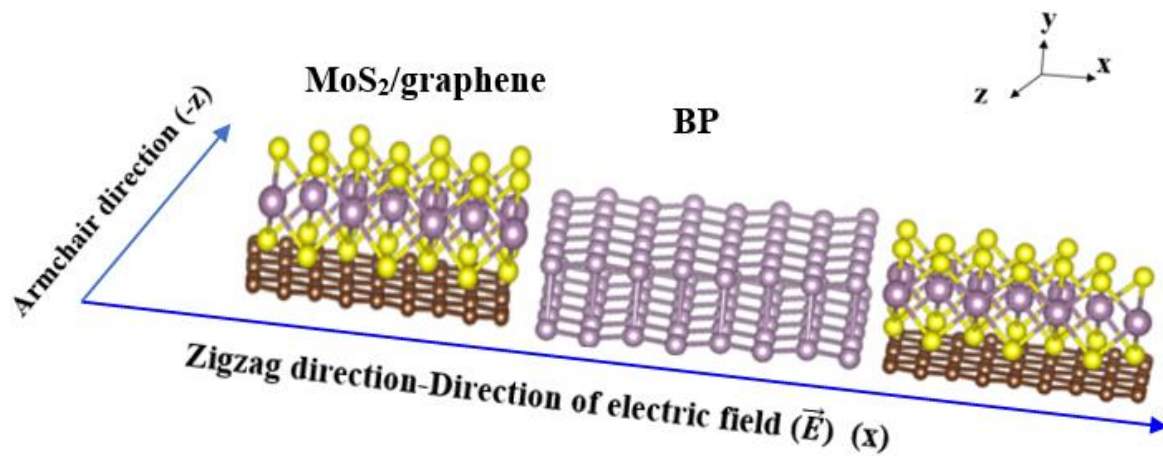
### 2.2.3 Graphene, Phosphorene and MoS<sub>2</sub> Structure

The MoS<sub>2</sub>/graphene heterostructure was not expected to have much absorptance, we need to modify the structure and increase the plasma oscillations that participates in the absorption. Making use of the in-plane graphene/phosphorene heterostructure, a new design could be reached including all of the three materials. Figure 22 is developed utilizing the easy integration of the in-plane armchair direction of graphene and phosphorene and the similar hexagonal structure of graphene and MoS<sub>2</sub>. The nanoribbon widths are  $W_n$ , and  $W_{BP}$  for graphene and phosphorene respectively with an applied voltage  $V_g$  on MoS<sub>2</sub>/graphene, and  $V_{BP}$  on MLBP.

(a)



(b)



(c)

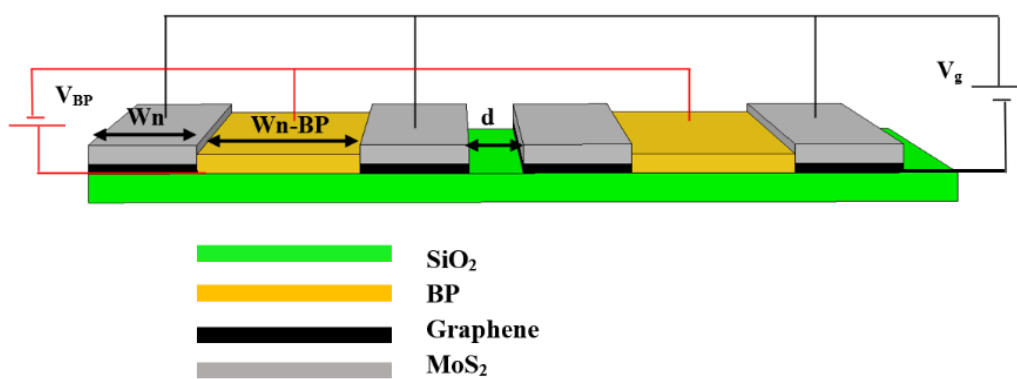


Figure 22: The proposed Structure of graphene, MoS<sub>2</sub>, and MLBP.

(a) The 2D representation of a unit cell (not to scale for clarification); (b) The orientation of the monolayers of one unit cell; (c) The 3D representation of an array of two cells.

## Chapter 3 : Results

### 3.1 MoS<sub>2</sub> Nanoribbons on SiO<sub>2</sub>

MoS<sub>2</sub> is known for its high transmittance in the THz region due to its large band gap which lies in the visible range ( $\sim 1.9$  eV), however there is some absorption due to the intra-band transitions. The absorptance and transmittance of monolayer MoS<sub>2</sub> nanoribbons on SiO<sub>2</sub> was first tested with nanoribbon width  $W_n = 40$  nm, spacing between the nanoribbons  $d = 10$  nm with a substrate thickness  $d_{sub} = 5$  nm, and h-BN thickness = 5 nm Figure 23. A small absorption peak is noticed at  $\sim 2.29$  THz, while the monolayer is still a good transmitter for THz waves Figure 24. The electric field distribution is shown at Figure 25. Since the absorptance is directly proportional to the electric field intensity  $E^2$ , the highest electric field is at 2.29 THz and is approximately  $2.5 \times 10^6$  V/m where it is concentrated at the edges, which manifests a plasmon oscillation, Figure 25b. The electric field is less ( $\sim 2 \times 10^5$ ) V/m at other frequencies and is distributed across the whole ribbon Figure 25(c, d). The effect of changing the structure dimensions is shown in Figure 26. Increasing the nanoribbon width redshifts the frequency of absorption where the maximum absorption in the THz region is 0.017. On the other side, increasing the substrate thickness  $d_{sub}$  very slightly blue shifts the absorption frequency. Increasing the spacings between the nanoribbons  $d$  decreases the absorption, so it is better to keep the least spacings between the nanoribbons. Increasing the h-BN coating thickness could increase the absorption. It is to be noted that varying the applied vertical voltage on MoS<sub>2</sub> doesn't affect the absorption frequency.

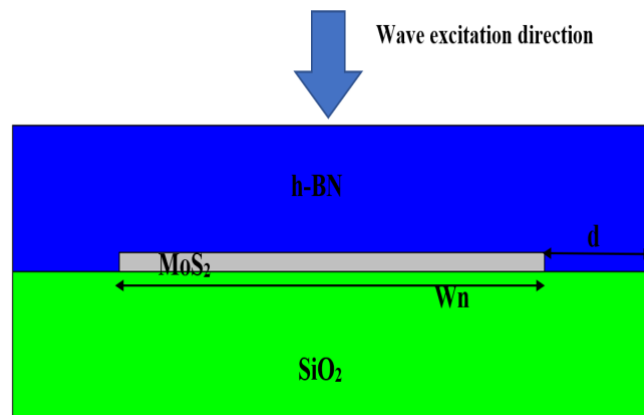


Figure 23: A 2D schematic of monolayer nanoribbon MoS<sub>2</sub> on SiO<sub>2</sub> (not to scale for clarification)



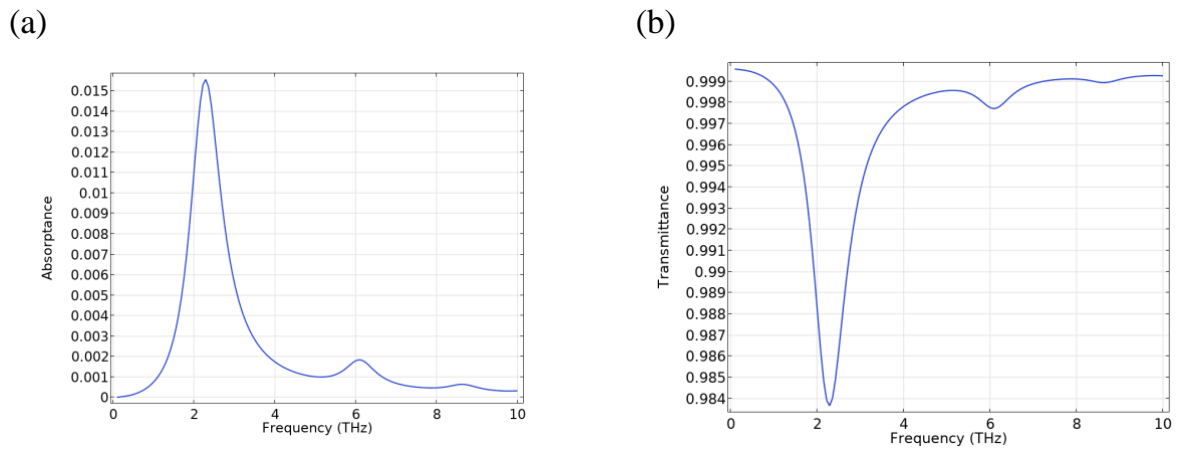


Figure 24: The absorptance and transmittance of MoS<sub>2</sub> nanoribbons: (a) The absorptance; (b) The transmittance.

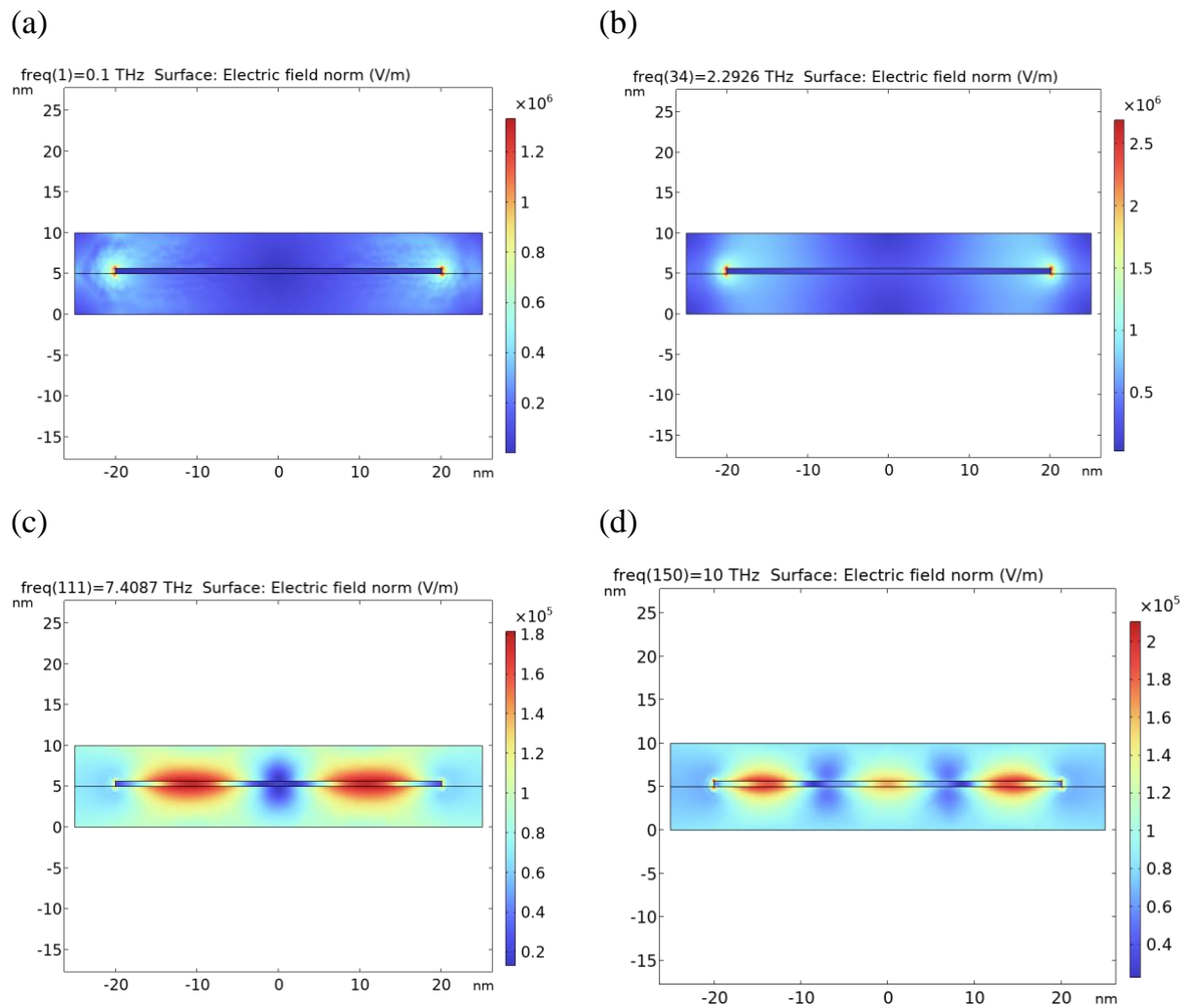


Figure 25: The electric field distribution across the MoS<sub>2</sub> nanoribbon at different frequencies (f): (a) f=0.1 THz; (b) f=2.29 THz; (c) f=7.4 THz; (d) f=10 THz.

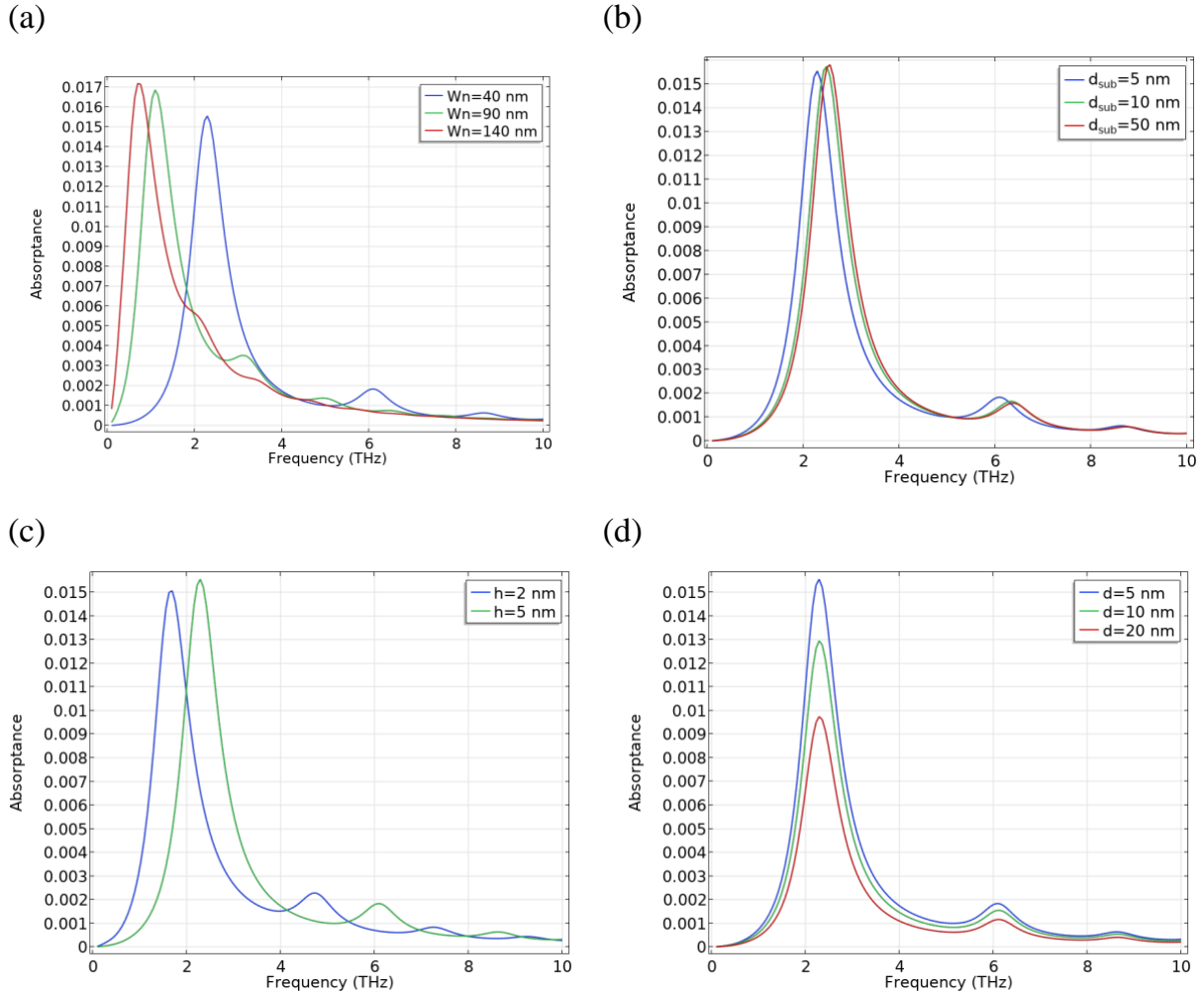


Figure 26: The effect of the structure dimensions on the absorption frequency of MoS<sub>2</sub> nanoribbons.

(a) The nanoribbon width effect  $W_n = 40, 90, 140 \text{ nm}$ ; (b) The effect of the substrate thickness  $d_{sub} = 5, 10, 50 \text{ nm}$ ; (c) The effect of the h-BN thickness  $h = 2, 5 \text{ nm}$ ; (d) The effect of the spacings between nanoribbons  $d = 5, 10, 20 \text{ nm}$ .

### 3.2 Graphene Nanoribbons on SiO<sub>2</sub>

The absorptance of graphene nanoribbons was first tested using the Drude model only in Figure 27. As shown, the absorptance decreases when gate voltage increases which means that the intra-band transitions are no longer responsible for absorption and the absorption is dominated by the inter-band transitions. The electric field distribution shows the reflection of most of the electric field and very little absorption is detected. The transmittance and reflectance curves in Figure 27(c, and d) assures the tiny absorptance. The inter-band and intra-band transitions are then included using the Kubo formula and the results of graphene nanoribbons represented in Figure 28. The structure

is tested for a nanoribbon width  $W_n = 120$  nm, spacing between the nanoribbons  $d = 10$  nm with a substrate thickness  $d_{sub} = 5$  nm, and h-BN thickness  $h = 5$  nm and  $V_g = 0.5$  V. A graphene nanoribbon could achieve a maximum absorption at 0.5 V slightly greater than 30%, while most of the remaining waves are transmitted. The electric field distribution is plotted in Figure 29, where the electric field has the highest value at the absorption frequency 5.28 THz and most of the electric field is concentrated at the edges (edge plasmon absorption). The electric field distribution was also plotted at  $f = 10$  THz where the absorption is minimum where there is no noticeable absorption and no edge plasmons. Figure 30 shows the effect of varying vertical applied voltage  $V_g$  on the absorption and transmittance of the graphene nanoribbon, where there is a kind of saturation in the absorptance at  $V_g > 0.7$  V. The effect of varying the dimensions on shifting the absorption frequency is shown in Figure 31. Increasing the nanoribbon width  $W_n$  red shifts the absorption frequency, the same as in case of MoS<sub>2</sub>. The shift in the absorption frequency due to increasing the substrate thickness  $d_{sub}$  is more obvious than in case of MoS<sub>2</sub> and is accompanied by a decrease in the absorption. The effect of the spacings  $d$  is very small and can be neglected. The height of the h-BN has a greater effect on shifting the absorption frequency than MoS<sub>2</sub>.

(a)

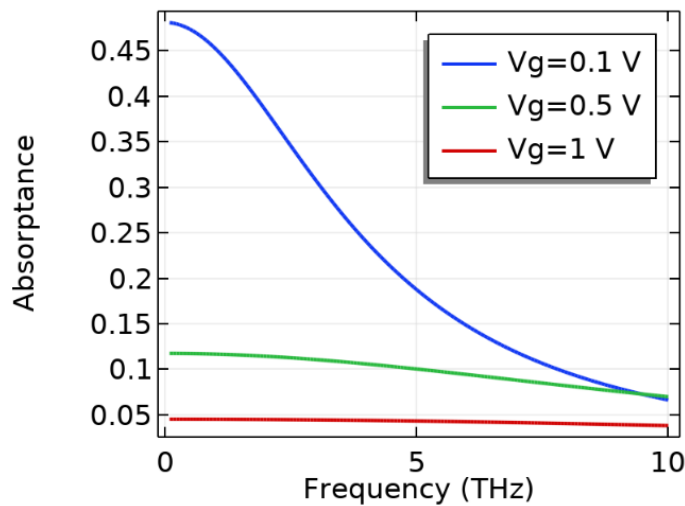
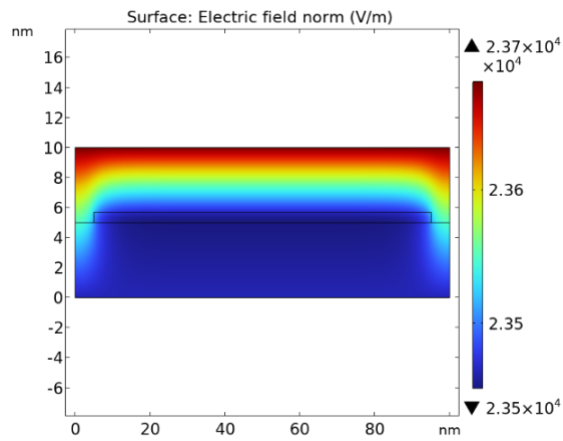


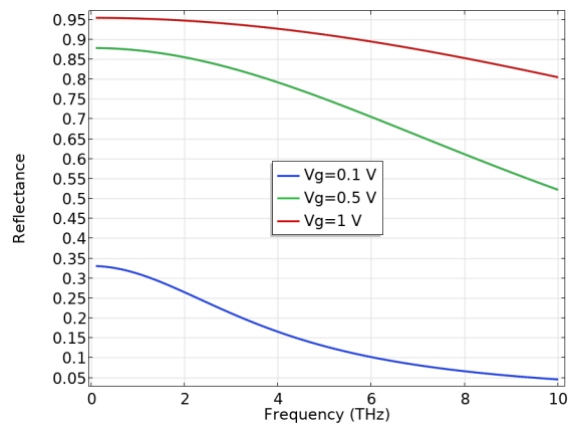
Figure 27: The absorptance of graphene when considering the Drude model only.

(a) the absorptance versus frequency (THz); (b) The electric field norm (V/m) distribution at  $V_g = 1$  V and  $f = 10$  THz; (c) The reflectance; (d) the transmittance.

(b)



(c)



(d)

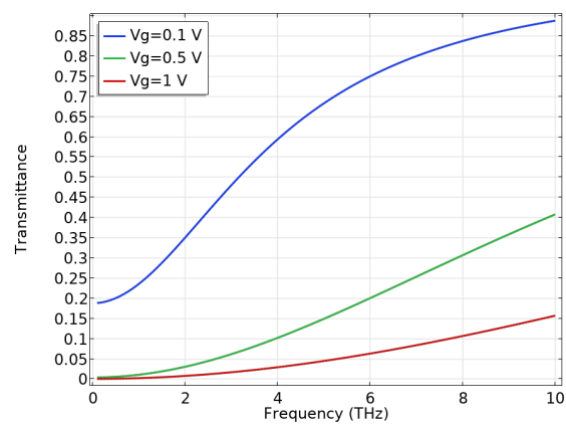
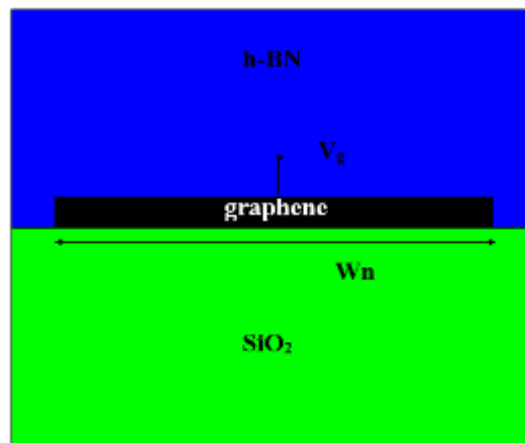


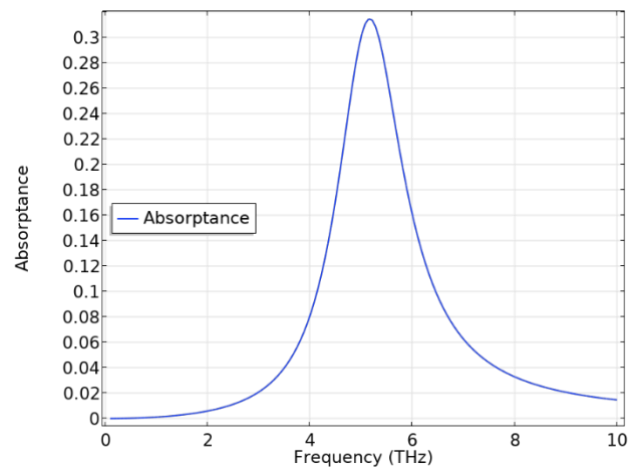
Figure 27: The absorptance of graphene when considering the Drude model only (Continued).

(a) the absorptance versus frequency (THz); (b) The electric field norm (V/m) distribution at  $V_g = 1V$  and  $f=10$  THz; (c) The reflectance; (d) the transmittance.

(a)



(b)



(c)

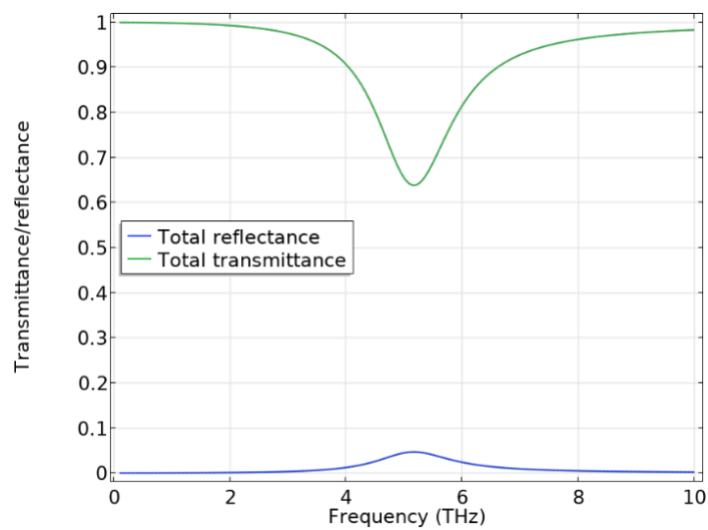
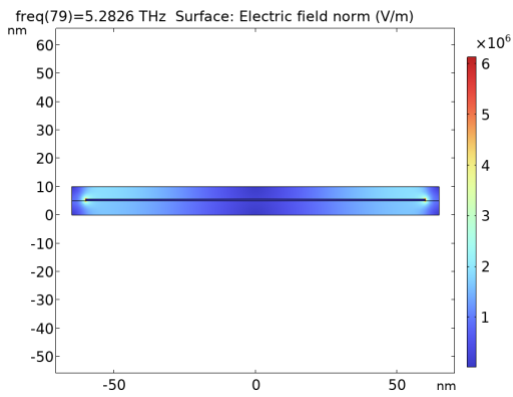


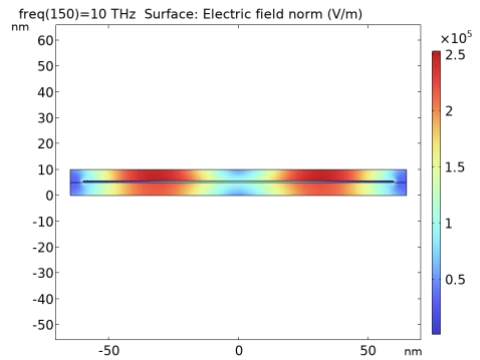
Figure 28: Graphene nanoribbons over  $\text{SiO}_2$ .

(a) A 2D schematic of monolayer nanoribbon  $\text{MoS}_2$  on  $\text{SiO}_2$  (not to scale for clarification); (b) The absorbance of graphene nanoribbons; (c) The transmittance and reflectance of graphene nanoribbons at  $W_n = 120 \text{ nm}$ ,  $V_g = 0.5 \text{ V}$

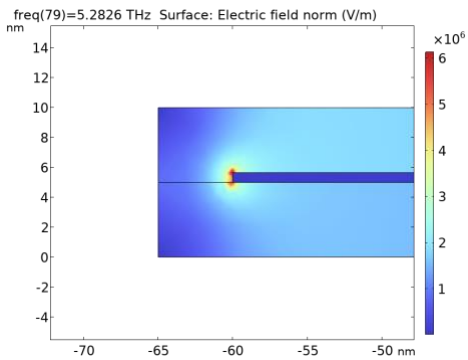
(a)



(b)



(c)



(d)

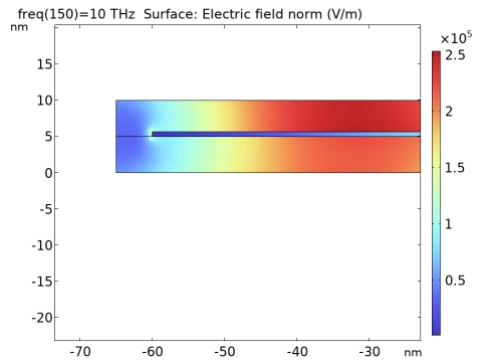
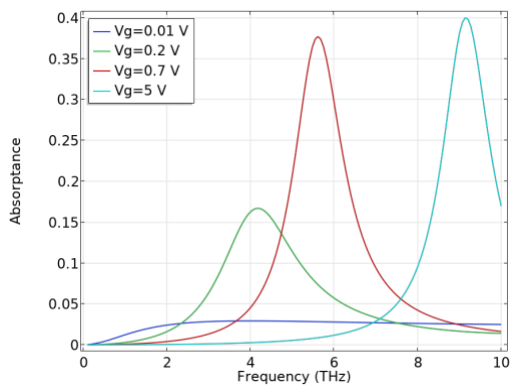


Figure 29: The electric field distribution across graphene nanoribbon at different frequencies (f). (a)  $f=5.28$  THz; (b)  $f=10$  THz; (c) The zoom in at  $f=5.28$  THz; (d) The zoom in at  $f=10$  THz

(a)



(b)

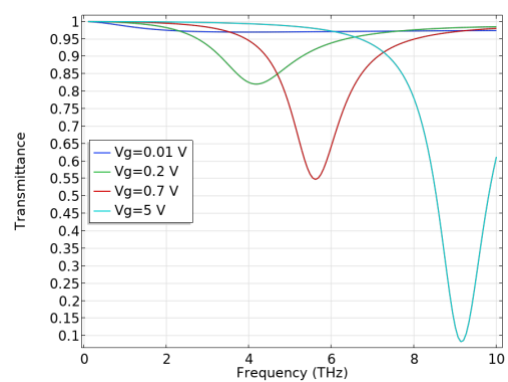


Figure 30: The effect of gate voltage on the absorbance and transmittance of graphene nanoribbons.

(a) The Absorbance of graphene; (b) The transmittance of graphene.  $d_{\text{sub}}=5$  nm  $w_n=120$  nm, at variable gate voltages  $V_g=0.01, 0.2, 0.7, 5$  V

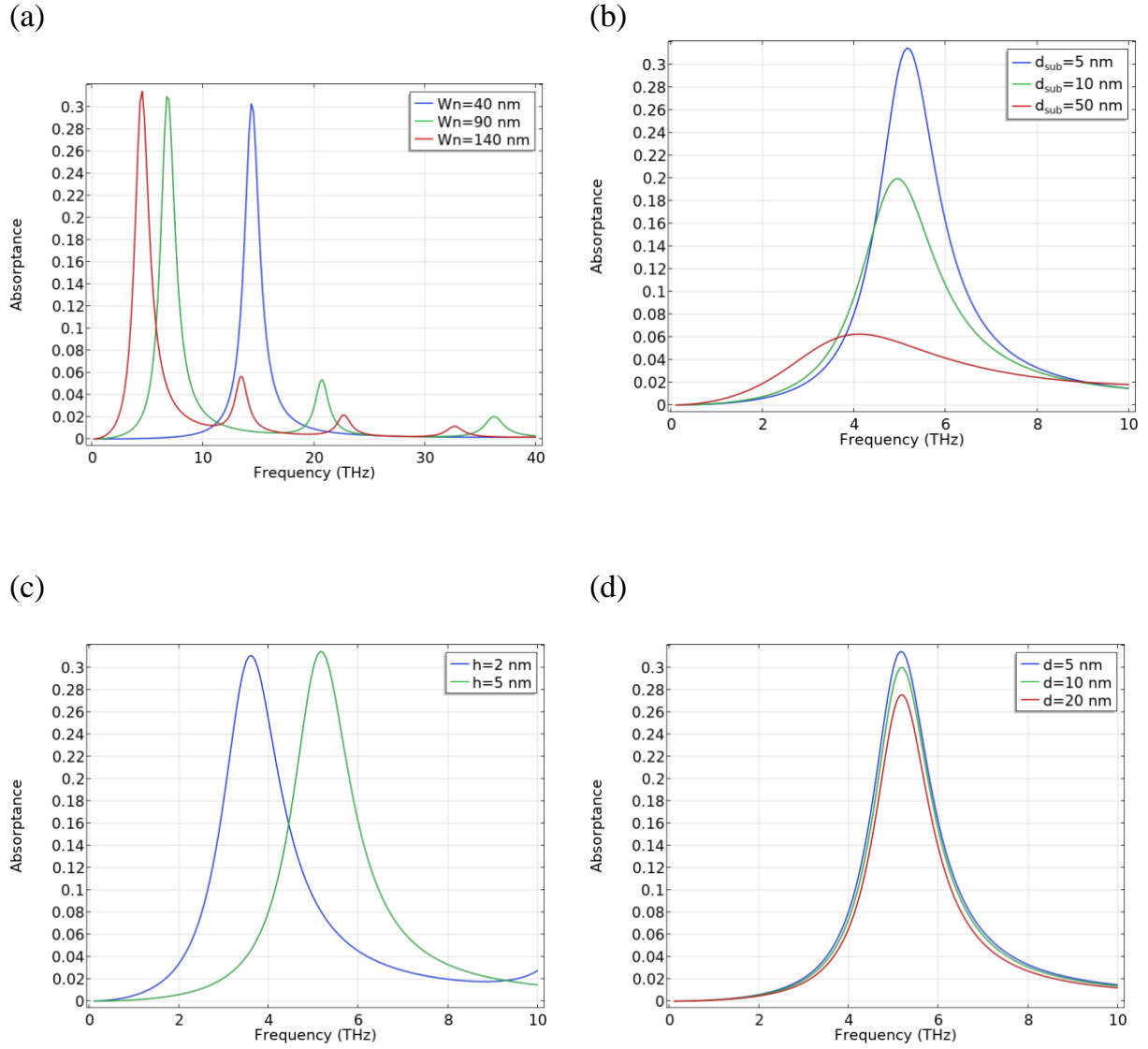


Figure 31: The effect of the structure dimensions on the absorption frequency of graphene nanoribbons.

(a) The nanoribbon width effect  $W_n = 40, 90, 140$  nm; (b) The effect of the substrate thickness  $d_{sub} = 5, 10, 50$  nm; (c) The effect of the h-BN thickness  $h = 2, 5$  nm; (d) The effect of the spacings between nanoribbons  $d = 5, 10, 20$  nm.

### 3.3 MoS<sub>2</sub>/Graphene nanoribbons Heterostructure on SiO<sub>2</sub>

The absorption of graphene nanoribbons at low voltages ( $< 1$  V) couldn't achieve absorption greater than 40%. The absorptance of MoS<sub>2</sub>/graphene heterostructure is discussed in this section (Samy et al., 2023). For a channel length of 120 nm and the same parameters for  $h, d, W_n$  of the graphene only nanoribbon as in the previous section, we have higher absorption especially at low voltages. At  $V_g = 0.2$  V, the absorption rises from less than 20% to  $\sim 35\%$  Figure 32, and saturates at 45%. For a better comparison

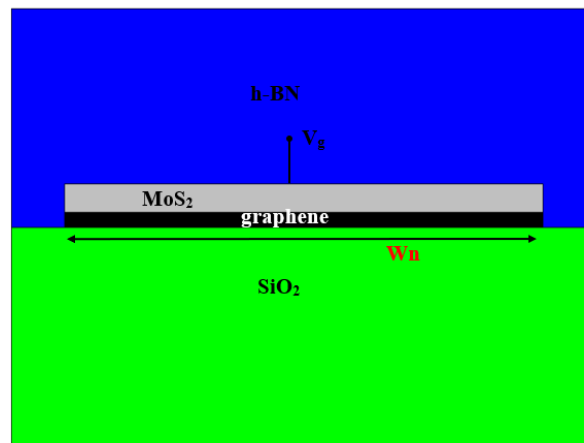
between graphene only and MoS<sub>2</sub>/graphene nanoribbons results. The absorption of both of them is plotted in the same graph in Figure 33. Beside the increase in the absorptance due to the heterostructure, there is a blue shift in the absorptance frequency at the same applied voltage, which means an inter-band transition occurs for the same voltage at higher energy (a larger band gap) which is anticipated to the band gap opening due to the heterostructure. The electric field distribution at a  $V_g = 0.4 V$ , and channel length 90 nm at the absorptance frequency is detected in Figure 34. The effect of varying the channel width  $W_n$  and the substrate thickness  $d_{sub}$  at different voltages are plotted in Figure 35 and Figure 36. Decreasing the channel width blue shifts the frequency of absorptance with a maximum absorption of less than 50% at  $V_g = 0.4 V$ . The shift towards higher frequencies at low widths can be attributed to the increase in the band gap of graphene nanoribbon which is higher than the case of graphene only structure due to the opening in the band gap by the effect of MoS<sub>2</sub>. The blue shift in the absorptance frequency due to the substrate thickness is best described by the argument by Ullah et al. (2020), where larger  $d_{sub}$  indicates low capacitance value and low carrier concentration  $n_g$  as in Equation (2.31) and since the resonance frequency or the absorption peak frequency follows the rule,  $\omega \propto \frac{1}{\sqrt{LC}}$  where L and C are the equivalent inductance and capacitance of the structure respectively, the resonance (absorption) frequency increases or shifts towards higher frequencies when capacitance decreases. In order to have a good voltage tunable absorber for small nanoribbon widths (90 nm) in the THz region, we have to use a small substrate thickness in the range of 5 nm. We need a small  $d_{sub}$  (high equivalent capacitance) to have enough carrier concentration at the THz frequency.

Temperature variations affects the carrier concentrations in graphene nanoribbons, however, this effect will not be obvious for nanoribbons widths greater than 100 nm (Fang et al., 2007b). The increase in carrier concentration due to temperature rises is very low especially in the presence of applied voltage. At the same time, the transmittance of MoS<sub>2</sub> sheets slightly decreases with increasing temperature (Li et al., 2019), that's why we cannot see a great effect of temperature on the structure absorptance, especially at higher voltages. The experimental work conducted by Liu et al. (2020) showed that both the refractive index  $n$  and the extinction coefficient  $\kappa$  curves



of MoS<sub>2</sub> aren't affected when varying the temperature from 4.5 K to 500 K as we go towards the THz region. The nanoribbon structure is stable against temperature variations. Figure 37 shows a slight variation in absorptance above 300 K that vanishes at higher gate voltages as in Figure 38.

(a)



(b)

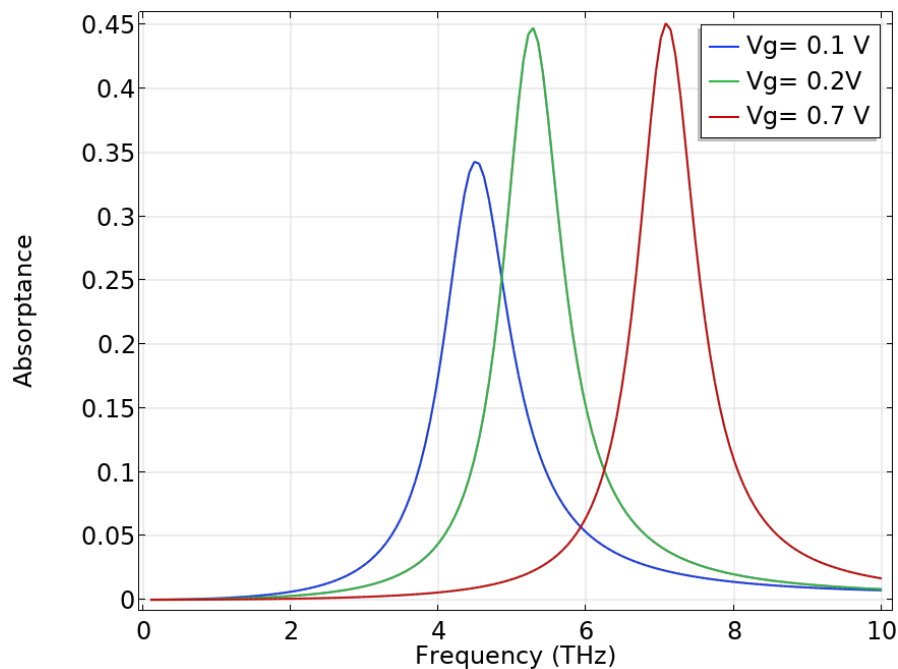


Figure 32: The absorptance of MoS<sub>2</sub>/graphene heterostructure at different gate voltages  $V_g = 0.1, 0.2, 0.7$  V.

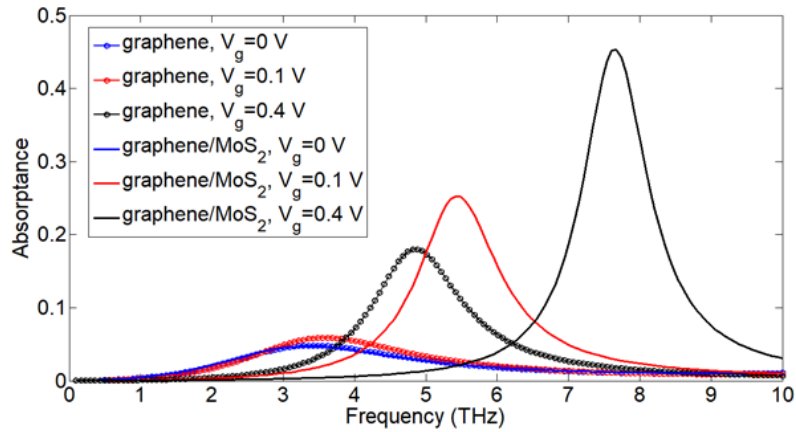
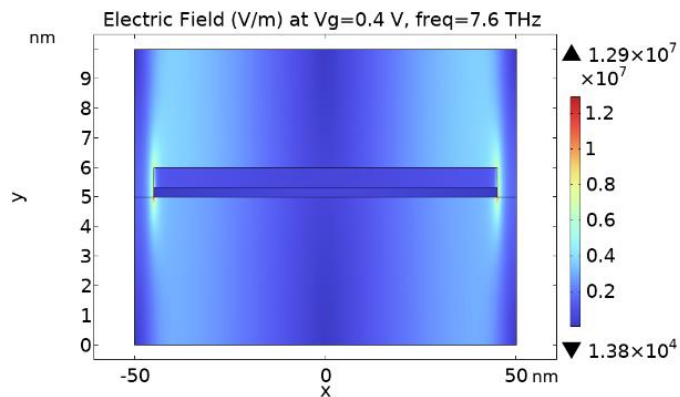


Figure 33: Comparison between the absorption of graphene only and MoS<sub>2</sub>/graphene heterostructure. The nanoribbon structure absorptance in case of graphene only (marked lines) and MoS<sub>2</sub>/graphene heterostructure (solid lines) at different gate voltages  $V_g=0, 0.1, 0.4$

(a)



(b)

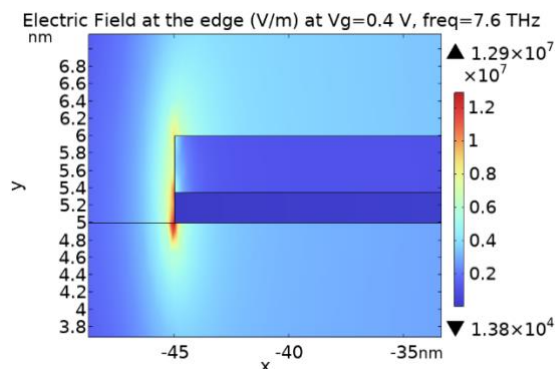
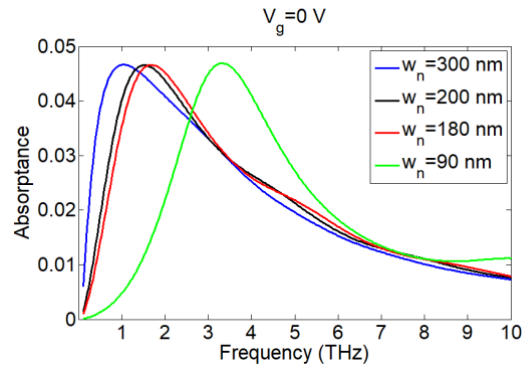
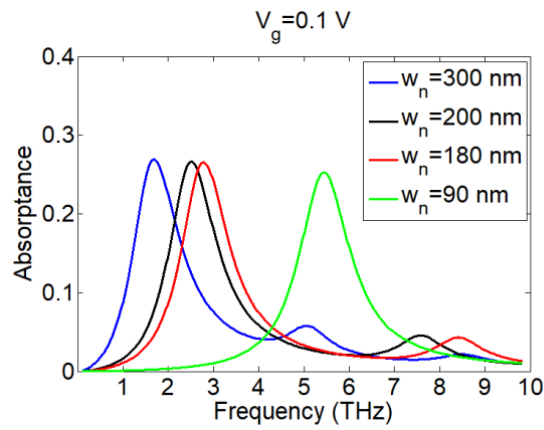


Figure 34: The Electric field amplitude across one nanoribbon : (a) The electric field amplitude of a 90 nm width nanoribbon structure at  $V_g = 0.4$  V; (b) The zoom in of the nanoribbon edges at  $V_g = 0.4$  V.

(a)



(b)



(c)

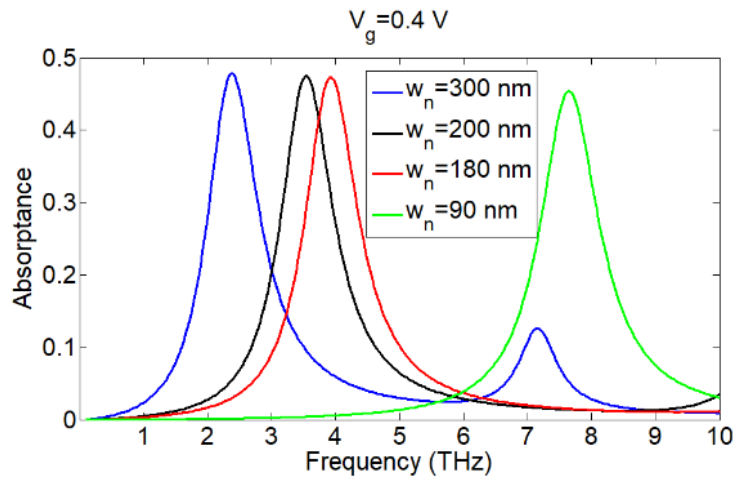


Figure 35: The effect of the nanoribbon width  $w_n$  on the absorbance frequency : (a) at  $V_g=0$  V; (b) at  $V_g=0.1$  V; (c) at  $V_g=0.4$  V.

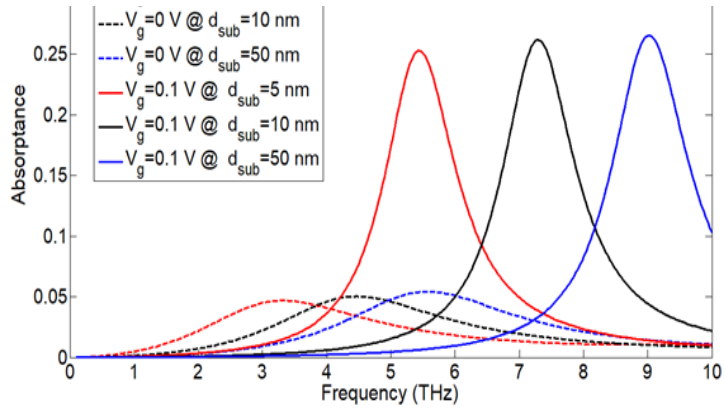


Figure 36: The effect of the substrate thickness  $d_{sub}$  of SiO<sub>2</sub> on the absorptance at  $V_g=0, 0.1$  V and nanoribbon width  $W_n = 90$  nm

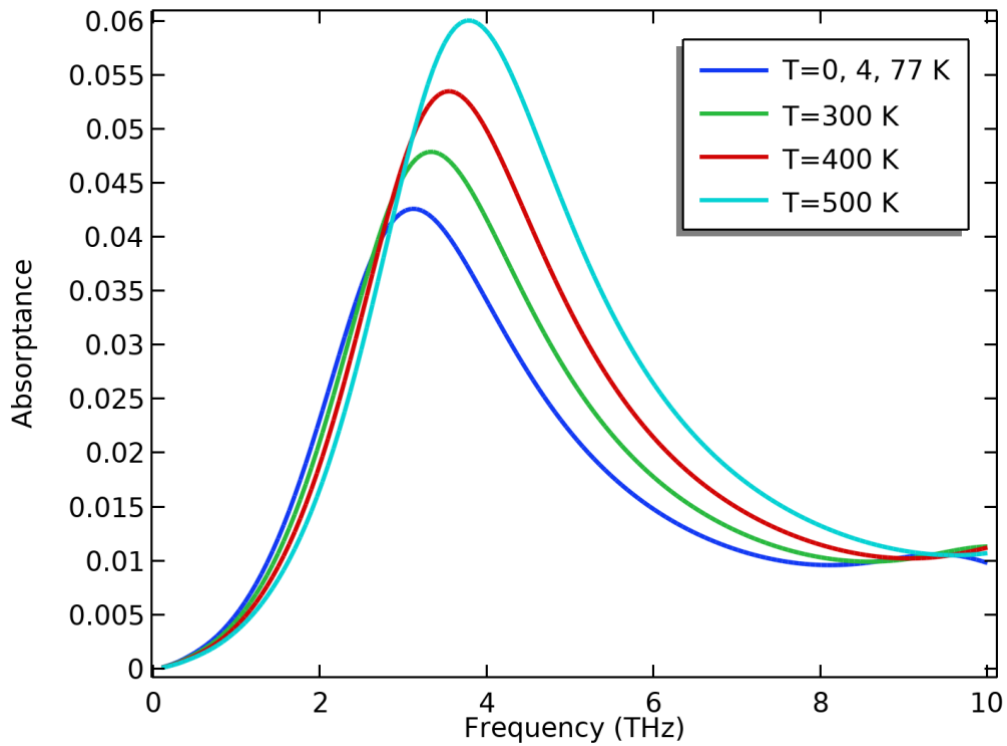


Figure 37: The effect of temperature on the absorptance of the nanoribbon structure at gate voltage  $V_g=0$

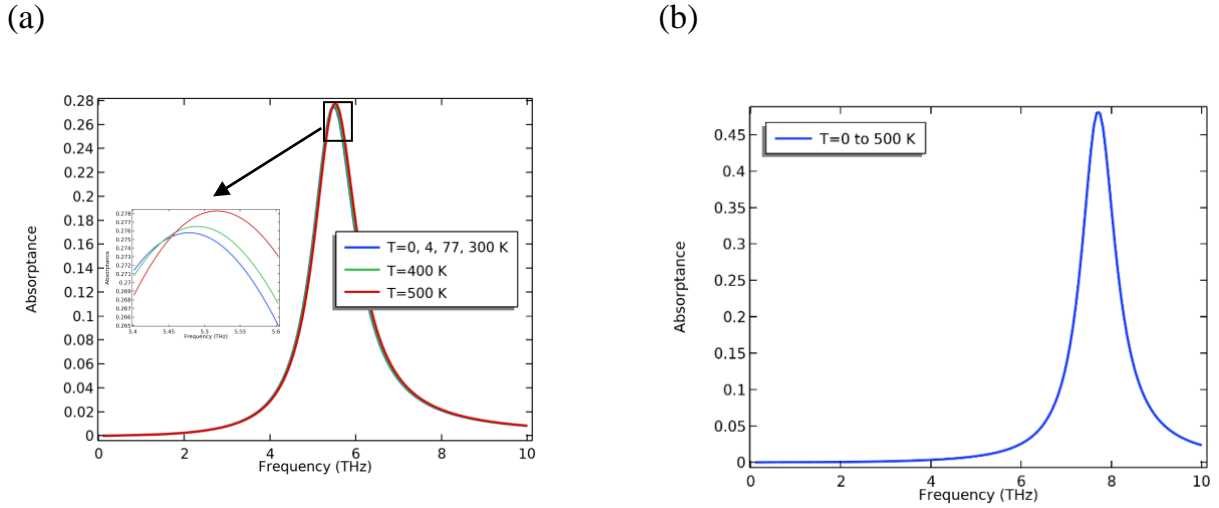


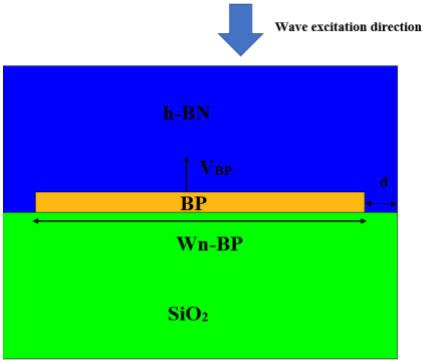
Figure 38: The effect of temperature on the absorptance of the nanoribbon structure; at gate voltage (a)  $V_g=0.1$  V, and (b)  $V_g=0.4$  V.

### 3.4 Phosphorene Nanoribbons on $\text{SiO}_2$

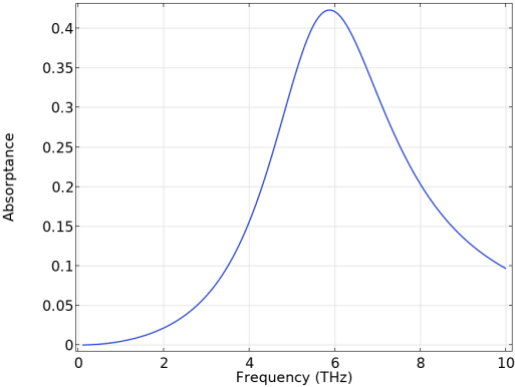
The same structure for graphene and  $\text{MoS}_2$  was repeated for phosphorene nanoribbons represented in Figure 39. The absorptance is tested for nanoribbon width  $W_{n-BP} = 200$  nm, , spacing between the nanoribbons  $d = 10$  nm with a substrate thickness  $d_{sub} = 5$  nm, and h-BN thickness  $h = 5$  nm. With a  $V_{BP} = 0.46$  V. The applied gate voltage on MLBP was tested for several values to reach the required one that achieves the highest absorption. Below this value the absorption is low and above this value we have absorption outside the THz range for our given device dimensions Figure 42. For the structure in Figure 39, a very small portion of the incident wave is reflected, while most of the wave is approximately half absorbed and half transmitted with maximum absorption of approximately 40%. The electric field distribution is plotted in Figure 40, where the electric field has the highest value at the absorption frequency 5.9 THz and most of the electric field is concentrated at the edges. The effect of varying the dimensions on shifting the absorption frequency is shown in Figure 41, the effect of increasing the nanoribbon width  $W_{n-BP}$  red shifts the absorption frequency, the same as in case of  $\text{MoS}_2$  and graphene. The shift in the absorption frequency due to increasing the substrate thickness  $d_{sub}$  is more obvious than in case of  $\text{MoS}_2$ , while the effect of the spacings  $d$  can be neglected. The height of the h-BN has a greater effect on shifting the absorption frequency than  $\text{MoS}_2$ . Figure 42 shows the effect of varying vertical applied

voltage on the absorption frequency, where increasing the applied voltage above a certain limit shifts the absorption frequency outside the THz range and also affects the percentage of absorption. There is a critical applied voltage that verifies the highest absorption, in this case it is 0.5 V.

(a)



(b)



(c)

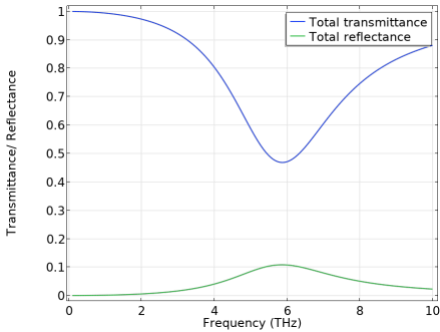
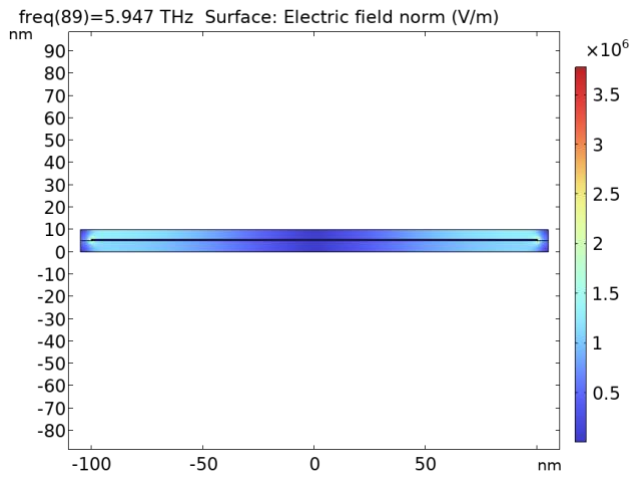
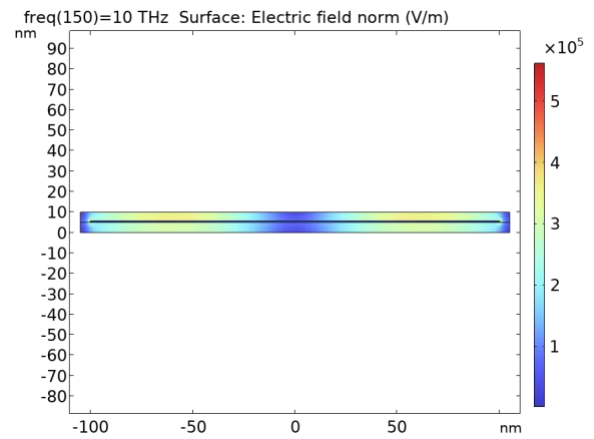


Figure 39 : Phosphorene nanoribbons on SiO<sub>2</sub> : (a) 2D representation of phosphorene nanoribbons on SiO<sub>2</sub> (not to scale for clarification); (b) The absorption of monolayer phosphorene at  $V_{BP} = 0.46$  V, (c) The transmittance and reflectance.

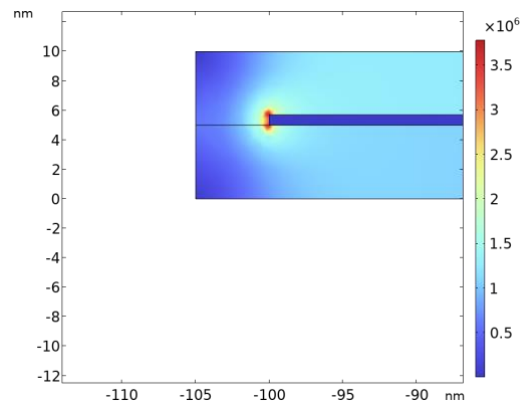
(a)



(b)



(c)



(d)

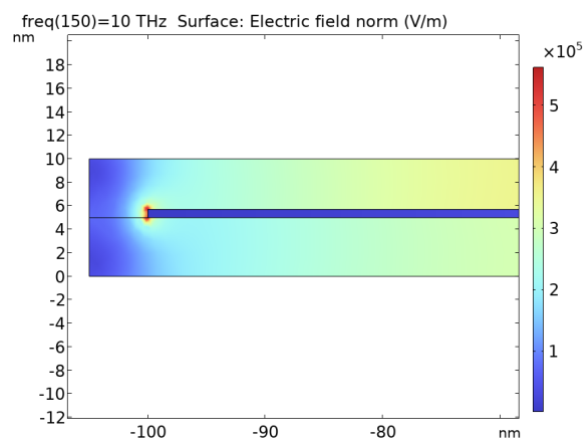


Figure 40: The electric field distribution of phosphorene nanoribbon at different frequencies : (a) at the absorption frequency 5.9 THz; (b) frequency  $f=10$  THz; (c) The zoom in of the edges at  $f=5.9$  THz; (d) The zoom in of the edges at  $f=10$  THz

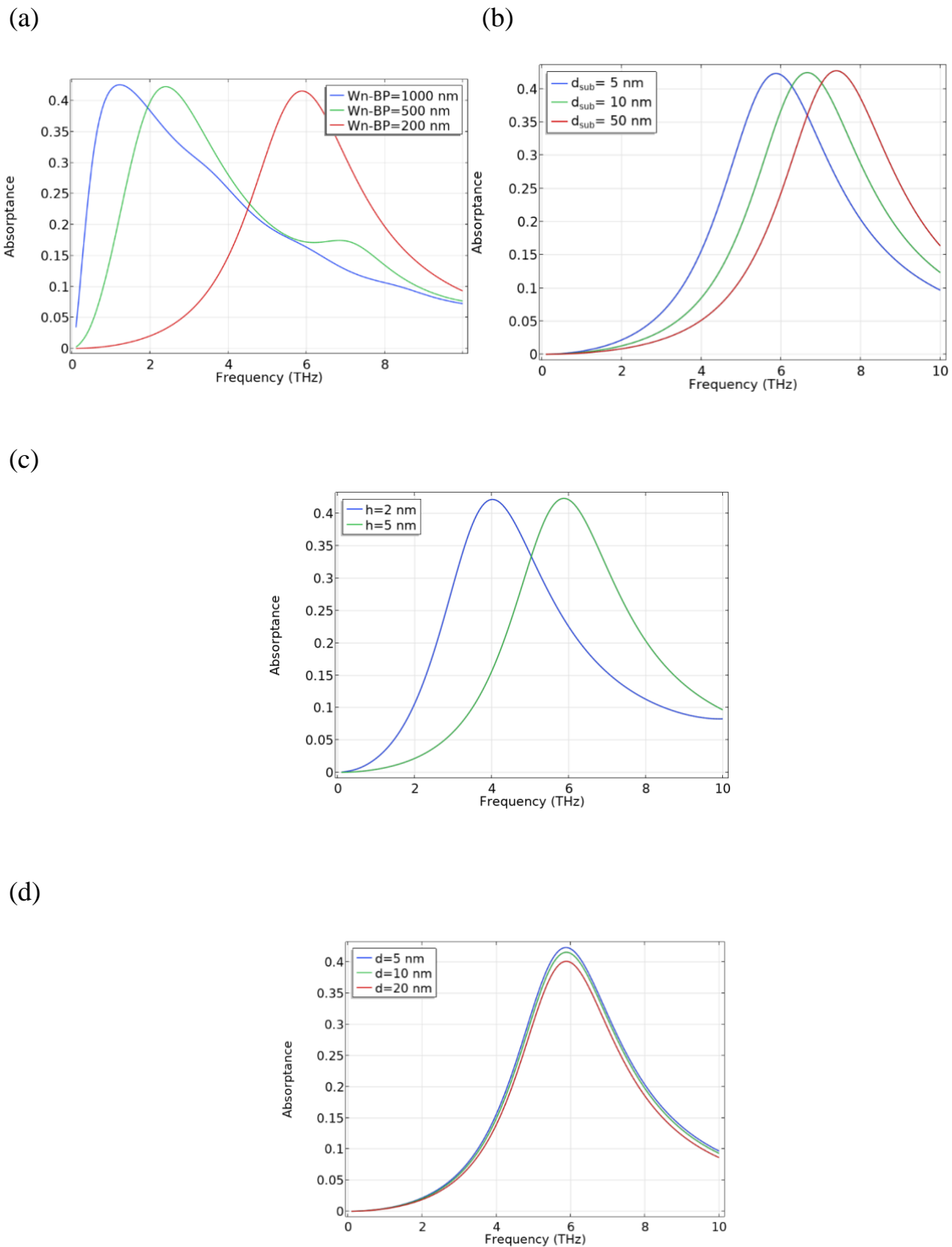


Figure 41: The effect of the structure dimensions on the absorption frequency of phosphorene nanoribbons.

(a) The nanoribbon width effect  $W_n = 40, 90, 140 \text{ nm}$ ; (b) The effect of the substrate thickness  $d_{sub} = 5, 10, 50 \text{ nm}$ ; (c) The effect of the h-BN thickness  $h=2, 5 \text{ nm}$ ; (d) The effect of the spacings between nanoribbons  $d= 5, 10, 20 \text{ nm}$ .



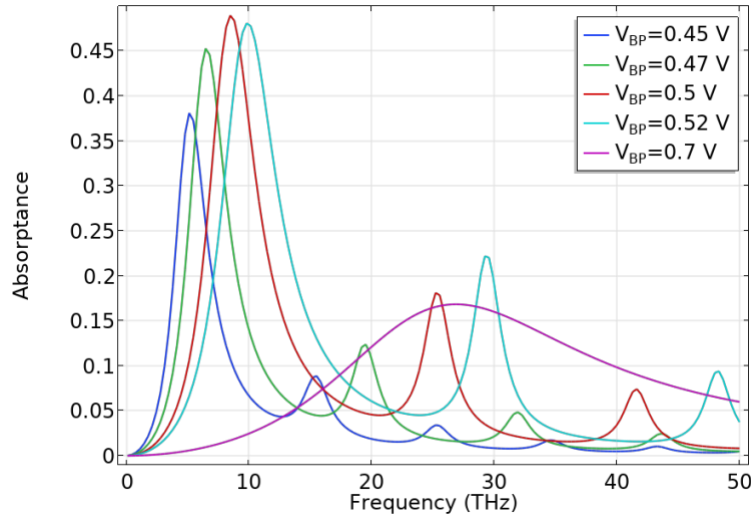


Figure 42: The effect of varying the vertical voltage  $V_{BP}$  on the absorption frequency; at  $V_{BP} = 0.45, 0.47, 0.5, 0.52$  and  $0.7 V$

### 3.5 The Proposed Structure (MoS<sub>2</sub>/Graphene-Phosphorene- MoS<sub>2</sub>/Graphene)

This part discusses the absorption of the final proposed structure and the effect of the applied voltage and varying the dimensions (width and thickness) on the absorption frequency. When MoS<sub>2</sub> is stacked over graphene minigaps are formulated in graphene (Pierucci et al., 2016). These band gaps are due to the hybridization between the  $\pi$  band in graphene with the out of plane orbital in MoS<sub>2</sub>. The study by Pierucci et al. (2016) confirmed no interaction between graphene and MoS<sub>2</sub> interfaces and a possible charge transfer from MoS<sub>2</sub> to graphene. The absorption of infinite nanoribbons of phosphorene or MoS<sub>2</sub>/graphene array structure could not exceed 50% for very thin structures (Debu et al., 2018; Samy et al., 2023). When using a combination of graphene, phosphorene, and MoS<sub>2</sub> to have the proposed structure in Figure 22, the absorption is greatly enhanced to more than 90% and can reach 95% at 10 THz for the stated dimensions as shown in Figure 44. The graphene/phosphorene/graphene structure are connected through strong chemical bonds where the energy barrier at the interface locks the carriers in graphene as discussed earlier. The role of phosphorene between the graphene nanoribbons is to lock carriers to the graphene/MoS<sub>2</sub> heterostructure, that in turn enhances the plasmonic resonance. This interprets the high electric field over the MoS<sub>2</sub>/graphene interface in Figure 43 that reached  $3 \times 10^{10}$  V/m at the edges which is the highest when compared to previous structures in sections 3.1.1 to 3.1.4. The nanoribbon width plays an important

role in varying the band gap of graphene and phosphorene. Increasing the width of the MoS<sub>2</sub>/graphene nanoribbon (20 ~ 120 nm) red shifts the absorption frequency as shown in Figure 44a. The same case happens with increasing the phosphorene nanoribbon width (40 ~ 160 nm) Figure 44b, however, varying the nanoribbon width of MoS<sub>2</sub>/graphene can easily sweep the absorption frequency over the entire THz range. Applying a gate voltage  $V_g$  sweeps the absorption frequency from 6 THz to 10 THz at small nanoribbon widths of  $W_n = 30$  nm for MoS<sub>2</sub>/graphene, and  $W_{n-BP} = 15$  nm for phosphorene Figure 45b. The bandwidth varies from 0.6 THz at 6 THz to 1.9 THz at 10 THz. Sweeping the absorption frequency through varying the applied voltage  $V_g$  at lower frequencies requires larger dimensions, with  $W_n = 140$  nm and  $W_{n-BP} = 120$  nm Figure 45a. In this case, a fine tuning is obtained starting from 1.3 THz at  $V_g = 0.2$  V. The dimensions of the structure can be modified according to the frequency range required to be swept. The effect of the substrate thickness on the absorptance, transmittance and reflectance of the structure is shown in Figure 46, where  $W_n = 30$  nm and  $W_{n-BP} = 15$  nm while fixing  $V_g$  and  $V_{BP}$  at 0.2 V and 0.46 V respectively. Increasing the thickness of the substrate decreases the transmission and the reflection of the structure and increases its absorption. A blue shift in the absorption frequency is also noticed with increasing the substrate thickness which can be attributed to the reduced capacitance of the structure at larger substrate thickness. A thickness of  $d_{sub} = 50$  nm can be regarded as the limit where no more shift in the absorption frequency or the absorptivity is noticed at  $V_g = 0.2$  V. The variation in the absorption frequency is nearly negligible at thicknesses  $> 5$  nm and have absorptivity  $> 90\%$ . It is not recommended to decrease the substrate thickness below 5 nm as this will result in decreased absorptance, besides, it may be impractical in fabrication. Larger thicknesses  $\geq 50$  nm could be used where we obtain near unity absorptance, but the blue shift in frequency could be compensated by an increase in the nanoribbon width (as in Figure 44) to sweep the whole THz frequency range through low applied voltages (0-0.5 V).

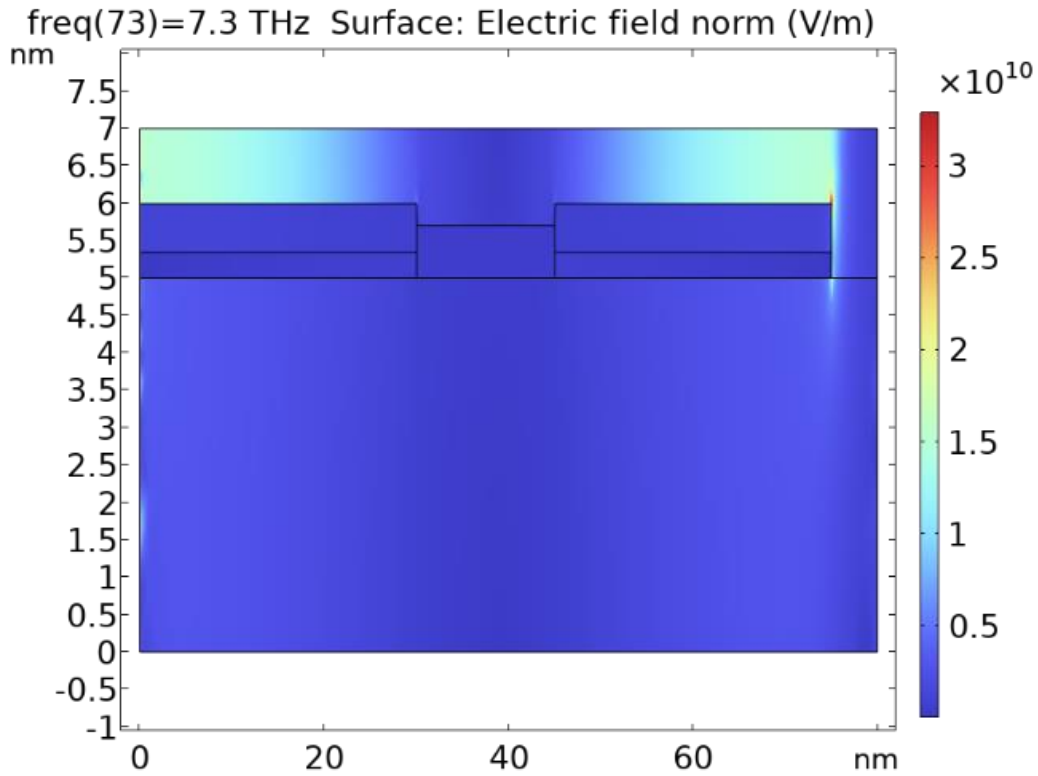
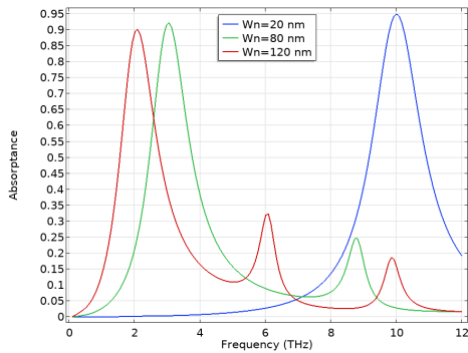


Figure 43: The surface electric field of a unit cell of the proposed structure; at  $W_n = 30 \text{ nm}$  and  $W_{BP} = 15 \text{ nm}$  measured at the frequency of highest absorption 7.3 THz at  $V_g = 0.5 \text{ V}$  and  $V_{BP} = 0.46 \text{ V}$ .

(a)



(b)

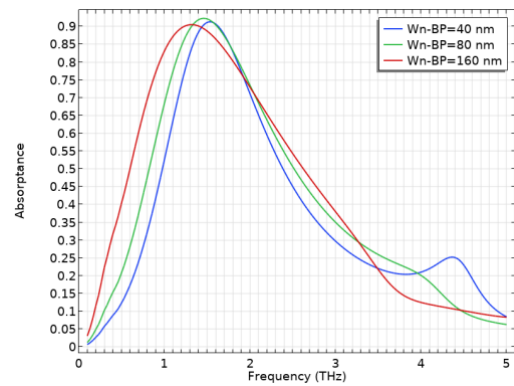


Figure 44: The nanoribbon width effect on sweeping the absorption frequency; at  $V_g = 0.5 \text{ V}$  and  $V_{BP} = 0.46 \text{ V}$

(a) Sweeping the MoS<sub>2</sub>/Gr nanoribbon width with a BP width of 15 nm  $W_{n-BP} = 15 \text{ nm}$  (b) Sweeping the BP nanoribbon width and MoS<sub>2</sub>/Gr nanoribbon width of 160 nm  $W_n = 160 \text{ nm}$

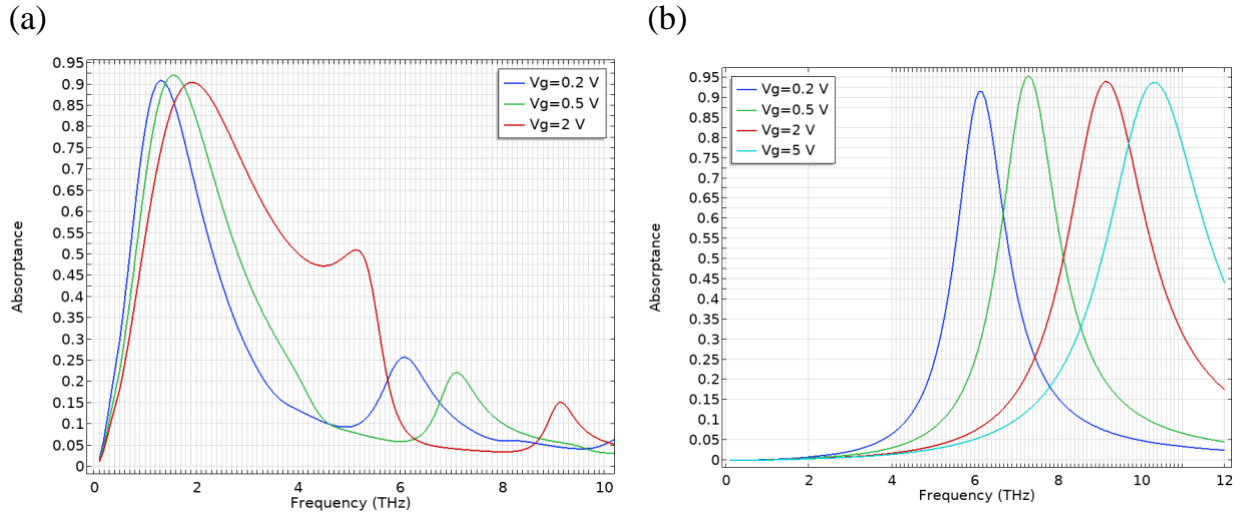


Figure 45: The effect of voltage applied on MoS<sub>2</sub>/Gr heterostructure on shifting the absorbance frequency: (a)  $W_n = 140 \text{ nm}$ ,  $W_{n-BP} = 120 \text{ nm}$  (b)  $W_n = 30 \text{ nm}$ ,  $W_{n-BP} = 15 \text{ nm}$ .

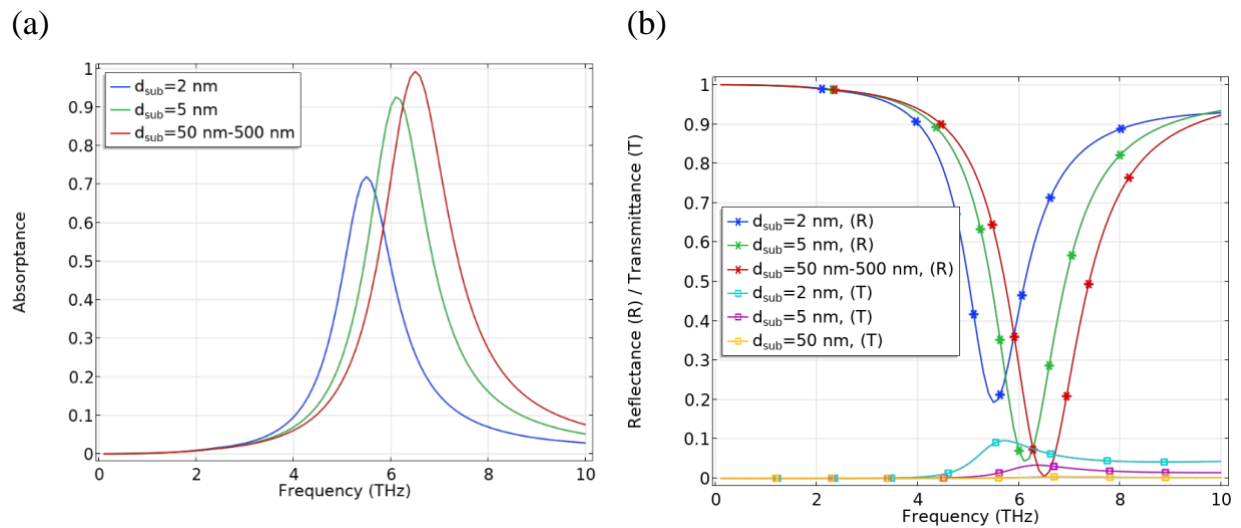


Figure 46: The effect of the substrate thickness  $d_{sub}$  on the absorbance, reflectance (R), transmittance (T) of the structure at  $W_n = 30 \text{ nm}$ ,  $W_{n-BP} = 15 \text{ nm}$ ,  $V_g = 0.2 \text{ V}$ , and  $V_{BP} = 0.46 \text{ V}$ .

(a) The absorbance at different substrate thicknesses  $d_{sub} = 2, 5, 50, \text{ and } 500 \text{ nm}$ ; (b) The reflectance (R), and transmittance (T) at different substrate thicknesses  $d_{sub} = 2, 5, 50, \text{ and } 500 \text{ nm}$ .

## Chapter 4 : Discussion

### 4.1 Validating the Novelty of the Structure

To clarify the novelty of our structure, we compared our work with the previous ones. There are different aspects to evaluate an absorber, like the efficiency, yield, cost, and bandwidth. In other words, how much wave the absorber is able to catch from the incident one, the cost of the materials used in the absorber; are they cheap or expensive; can the structure be easily fabricated and is it easy to have a large yield of it. For broadband absorbers, it is better to achieve the absorption frequency bandwidth as wide as possible. While in selective or narrow band absorbers, the absorber is more efficient when it has a very tight bandwidth. And another aspect that appears in selective absorbers; is the sweeping of the frequency of absorption through the THz spectrum easily without modifying the absorber dimensions (like using an electric field).

In Table 2 we summarized some of the main points that are used to assess an absorber like its bandwidth, absorptance, and design. We discussed some of the main challenges like including noble metals, complexity of the design, thickness and percentage of absorption. The mentioned THz absorbers in Table 2 face at least one or more challenges. The marked column in the table (✖) indicates the failure of this design to face the stated challenge, while this work overcomes those challenges. Including noble metals in the design could raise the cost of the absorber. Complex designs could be fabricated but it may be difficult to achieve on a commercial scale at low costs. A bulky absorber could have good characteristic with affordable materials, but it may be not that good to include in ultra-thin electronics or wearables. Most of the previous broadband and ultra-broadband absorbers lack one of these things. If they were able to achieve high absorptance above 90%, it is in a very small THz range (Baah et al., 2021; Wang et al., 2023; Zhong et al., 2021), and if they achieved high absorptance for a wide range, they are made of expensive materials and have complicated designs (Wu et al., 2023) or they may have limited frequency range over which the absorptivity is high and a complex structure at the same time (Chen et al., 2020). Some broadband absorbers overcome all the previous challenges but with bulk structures (Wang et al., 2020). Sometimes they include metals to increase the absorption like Wang et al. (2023) that has refractory

metals which are known for high cost, brittleness, heaviness, and toxicity. The thickness of the absorber plays an important role nowadays, where they can be used in wearable and ultra-thin electronic devices. Very few absorbers were few nanometers thickness while others are in the micrometer scale. Narrow band absorbers with high absorptivity are bulky, including metals with complex designs (Cheng et al., 2023; Shangguan et al., 2022; Yan et al., 2020).

Table 2: List of previous THz Absorbers

Ref.	Bandwidth	Absorptance	Structure	Challenges			
				1	2	3	4
( Wu et al., 2023)	6.89 THz	> 90% from 3.65 to 10.54 THz	cross-shaped gold resonator	✗			
(Wang et al., 2023)	Switchable wide band 1.60 THz	> 90 % through 1.71–3.31 THz	A metamaterial structure of Ti, TiO <sub>2</sub> & VO <sub>2</sub>	✗	✗	✗	
(Baah et al., 2021)	from few hundreds of GHz to 1.2 THz	~ 100%	“Bubble wrap” polymer nanomembrane covered with multi-layered graphene			✗	
(Gong et al., 2016)	~0.5 THz	>90% from 4.762 to 5.152 THz	Asymmetric square rings of Au over Si <sub>3</sub> N <sub>4</sub> .	✗	✗		
(Zhu et al., 2022)	Dual band	99.5% and 99.9% at 1.01 and 1.86 THz respectively	A graphene ring shape with a cross inside over SiO <sub>2</sub>	✗	✗		
(Islam et al., 2020)	Multiband	99.7% from 0.1–2.0 THz	Graphene meta surface, Au, SiO <sub>2</sub> , and Zeonex	✗	✗	✗	
(Mohsen Daraei et al., 2020)	~5.8 THz	70% from 9 to 7.7 THz	Stacked graphene ribbons on 2 different dielectrics on Au film	✗		✗	
(Chen et al., 2020)	Relative bandwidth of 72.1% at 90% absorptance	>90% from 2 to 5 THz	graphene sheet with a Gammadion-shaped and a dielectric substrate of polydimethylsiloxane placed on a metal film.	✗	✗	✗	
(Yan et al., 2020)	Narrow band 26.4 and 23.5 GHz at 0.2242 and 0.5302 THz respectively	two absorption peaks with 99.6% at 0.2242 and 0.5302 THz	Graphene pattern/Si/Au	✗	✗	✗	

<sup>1</sup> Includes metal

<sup>2</sup> Complex pattern

<sup>3</sup> Bulk structure (Thickness in tens of  $\mu m$  range or thousands of nanometres)

<sup>4</sup> Low absorption

Table 2: List of previous THz Absorbers (continued)

Ref.	Bandwidth	Absorptance	Structure	Challenges			
				1	2	3	4
(Cheng et al., 2023)	Switchable		Square patterned graphene/SiO <sub>2</sub> /Au				
	Broadband	>90% From 1.27 to 2.16 THz		×	×	×	
	narrow band	99% at 1.72 THz					
(Shangguan et al., 2022)	Narrow band 0.0171 and 0.0152 THz at 5.664 and 8.062 THz respectively.	99.41% and 99.22% at 5.664 THz and 8.062 THz respectively	Ring patterned graphene/SiO <sub>2</sub> /Au	×	×	×	
(Zhong et al., 2021)	Broadband 1.2 to 2.67 THz	>90% for frequencies from 1.375 to 2.75 THz	Patterned MoS <sub>2</sub> with a subwavelength ring-cross array, placed over a polymer over Au	×	×	×	
(Wang & Jiang, 2019)	Ultrawideband 3.4–9.6 THz	~ 90% through 4 to 10 THz	A stack of BP nanoribbons over dielectric on a gold base.	×	×		
(Xiao et al., 2019)	A variable bandwidth that increases at higher THz frequencies while absorption decreases	Maximum of 40%	A stack of multilayers of BP/dielectric/gold	×			
(Wang et al., 2020)	Broadband 2.9 & 3.5 THz	>90%	Sandwich structure of BP and dielectric (VO <sub>2</sub> )		×	×	
This work	0.9 - 1.3 THz	> 90% for frequencies from 0.1 to 10 THz	Nanoribbons of Graphene, MoS <sub>2</sub> , and phosphorene				

## 4.2 Interpreting Results using the Transmission Line Circuit Theory

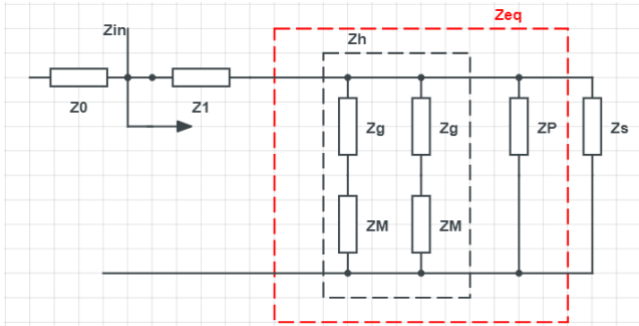
The transmission line model of the unit cell in Figure 22a can be represented by two transmission line impedances  $Z_0$  and  $Z_s$  for the incident medium (free space) and the substrate respectively, and a shunt impedance  $Z = Z_1 + Z_{eq}$  representing the structure impedance.  $Z_0$  is the free space impedance taken as  $120 \pi$  (376.73), and  $Z_s$  is the substrate impedance for SiO<sub>2</sub> calculated as  $Z_0/n_{\text{SiO}_2}$  where  $n_{\text{SiO}_2}=2.15$  is the refractive index of SiO<sub>2</sub>,  $Z_1$  represents the impedance of h-BN calculated as  $Z_0/n_{\text{h-BN}}$ ,  $n_{\text{h-BN}}$  is the refractive index of h-BN substituted as  $\sqrt{3.5}$  (Laturia et al., 2018).  $Z_{eq}$  is the equivalent impedance of the rest of the structure. For the simplicity of calculations, the impedance of the heterostructure MoS<sub>2</sub>/graphene is named  $Z_h$  consisting of two series impedances,

$Z_M$  for MoS<sub>2</sub> and  $Z_g$  for graphene, with each one having its own RLC circuit.  $Z_p$  is the phosphorene impedance and  $Z_{eq}$  is the equivalent impedance of  $Z_h$  and  $Z_p$ . Equations (4.1)-(4.3) describe the impedance calculations of the unit cell. The transmission line model represented by the structure impedances is shown in Figure 47a.

$$Z_h = \frac{Z_g + Z_M}{2} \quad (4.1)$$

$$Z_{eq} = \frac{Z_p \cdot Z_h}{Z_p + Z_h} \quad (4.2)$$

(a)



(b)

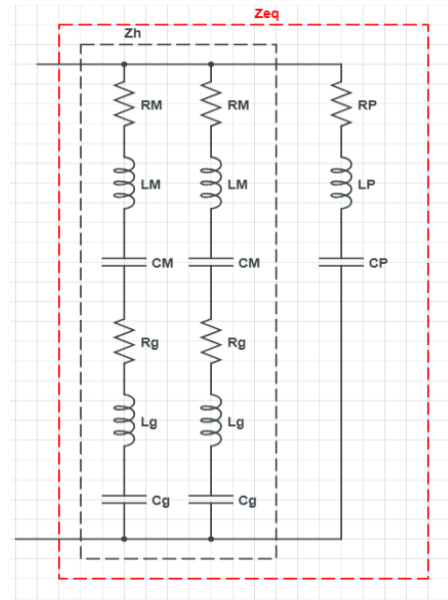


Figure 47 The transmission line model for a unit cell of the proposed structure. (a) The impedance model (b) The RLC model

$$Z_{in} = Z_1 + \frac{Z_h Z_p Z_s}{Z_h Z_p + Z_h Z_s + Z_p Z_s} \quad (4.3)$$

The RLC model of the circuit is shown in Figure 47b, where each material has a resistance, an inductance, and a capacitance represented by  $R_g, L_g, C_g$  for graphene,  $R_M, L_M, C_M$  for MoS<sub>2</sub> and  $R_P, L_P, C_P$  for phosphorene.

The values of the RLC circuit is calculated from the conductivity Equations (2.28), (2.33), and (2.35) for graphene, MoS<sub>2</sub>, and phosphorene respectively (Khavasi, 2015b; Khavasi & Rejaei, 2014), where the resistance and inductance are calculated



from the real and imaginary parts of the conductivity respectively according to Equations (4.6), and (4.7)

$$R = \frac{D}{S_1^2} \operatorname{Re}\{\sigma^{-1}\} \quad (4.4)$$

$$L = \frac{D}{S_1^2} \frac{\operatorname{Im}\{\sigma^{-1}\}}{\omega} \quad (4.5)$$

For MoS<sub>2</sub> and phosphorene, the RLC values are calculated based on the Drude model, as:

$$R_M = \frac{D_p}{S_1^2} \frac{m_{\text{MoS}_2}^*}{q^2 n_{\text{MoS}_2} \tau_{\text{MoS}_2}}, \quad R_P = \frac{D_p}{S_1^2} \frac{m_{\text{AC/ZZ}}^*}{q^2 n_{\text{AC/ZZ}} \frac{\hbar}{\eta}} \quad (4.6)$$

$$L_M = \frac{D_p}{S_1^2} \frac{m_{\text{MoS}_2}^*}{q^2 n_{\text{MoS}_2}}, \quad L_P = \frac{D_p}{S_1^2} \frac{m_{\text{AC/ZZ}}^*}{q^2 n_{\text{AC/ZZ}}} \quad (4.7)$$

$$C_M = \frac{S_1^2 \epsilon_o (\epsilon_{h\text{-BN}} + \epsilon_{\text{Gr}})}{D_p q_1}, \quad C_P = \frac{S_1^2 \epsilon_o (\epsilon_{h\text{-BN}} + \epsilon_{\text{SiO}_2})}{D_p q_1} \quad (4.8)$$

Where  $D_p$  is the period of the structure, taken as  $D_p = 2W_n + W_{n\text{-BP}} + d$  and  $S_1$  is the integration of the eign function for the first eign mode and can be taken as  $S_1^2 \approx \frac{8}{9} W$ , where  $W$  is the nanoribbon width (Khavasi, 2015a; Khavasi & Rejaei, 2014; Daraei et al., 2020).  $q_1$  is the first eigenvalue of the current equation based on the Drude model by Khavasi & Rejaei, (2014) and is calculated from  $q_1 = Q_1 \times \frac{\pi}{W}$  where  $W$  is the nanoribbon width taken as  $W_n$  for graphene and MoS<sub>2</sub> and  $W_{n\text{-BP}}$  for phosphorene.  $Q_1$  has values ranging from 0.4 to 0.7 that differs according to the ratio between the nanoribbon width  $W$  and the period of the structure  $D_p$  (Khavasi, 2015a; Daraei et al., 2020). The capacitance is calculated based on an effective permittivity as an average of the permittivity of the upper and lower materials.

Since we adopted the Kubo formula for the conductivity of graphene (2.28), the RLC values of graphene can be calculated as (see Appendix)

$$R_g = \frac{D_p}{S_1^2} \frac{8\pi\hbar^2(\omega^2 \tau^2 + 1) * X}{X + Y} \quad (4.9)$$

$$L_g = -\frac{D_p}{\omega S_1^2} \frac{8\pi\hbar^2(\omega^2\tau^2 + 1) * Y}{X + Y} \quad (4.10)$$

$$C_g = \frac{S_1^2}{D_p} \frac{\epsilon_o(\epsilon_{MoS_2} + \epsilon_{SiO_2})}{q_1} \quad (4.11)$$

Where X, Y are defined by Equations (4.12), and (4.13)

$$X = 8q^2A\tau - 2q^2\hbar(\omega^2\tau^2 + 1) \times \tan^{-1}\left(\frac{b}{a}\right) \quad (4.12)$$

$$Y = 8\omega q^2A\tau^2 + q^2\hbar(\omega^2\tau^2 + 1) \times \ln(a^2 + b^2) \quad (4.13)$$

And A, a, b are defined as

$$A = \mu_c + 2K_B T \times \ln\left(e^{-\frac{\mu_c}{K_B T}} + 1\right) \quad (4.14)$$

$$a = \frac{(2|\mu_c|\tau)^2 - (\hbar\omega\tau)^2 - \hbar^2}{\tau^2(2|\mu_c| + \hbar\omega)^2 + \hbar^2}, \quad b = \frac{-4|\mu_c|\tau\hbar}{\tau^2(2|\mu_c| + \hbar\omega)^2 + \hbar^2} \quad (4.15)$$

By substituting from (4.6) to (4.11) in (4.1), (4.2), and (4.3) where  $Z_g, Z_p, Z_M$  are as in (4.16) to (4.18), we get the input impedance ( $Z_{in}$ ). The real part of the structure impedance should match that of the free space and the imaginary parts should cancel each other's at a resonance frequency  $\omega_r = \frac{1}{\sqrt{LC}}$ , where L and C are the total equivalent inductance and capacitance of the structure respectively that vary according to the structure dimensions allowing for peak absorption at a resonance frequency  $\omega_r$ . Figure 48 shows the normalized input impedance ( $Z_{in}/Z_o$ ), for the real and imaginary parts of  $Z_{in}$  for two cases; case a: where  $W_n = 140 \text{ nm}$ , and  $W_{n-BP} = 120 \text{ nm}$ , and case b:  $W_n = 30 \text{ nm}$ ,  $W_{BP} = 15 \text{ nm}$ . For case a, the imaginary part crosses zero at a frequency near  $f = 2 \text{ THz}$ , where the real part of the normalized impedance approaches 1 ( $\sim 0.994$ ). For case b, the imaginary part crosses zero at a frequency near  $f = 6 \text{ THz}$ , where the real part of the normalized impedance approached 1 ( $\sim 0.994$ ). From Figure 45 we can see that the peak absorption occurred near  $f = 2 \text{ THz}$  and  $f = 6 \text{ THz}$  for these two cases respectively.

$$Z_g = R_g + j\omega L_g + \frac{1}{j\omega C_g} \quad (4.16)$$

$$Z_p = R_p + j\omega L_p + \frac{1}{j\omega C_p} \quad (4.17)$$

$$Z_M = R_M + j\omega L_M + \frac{1}{j\omega C_M} \quad (4.18)$$

(a)

(b)

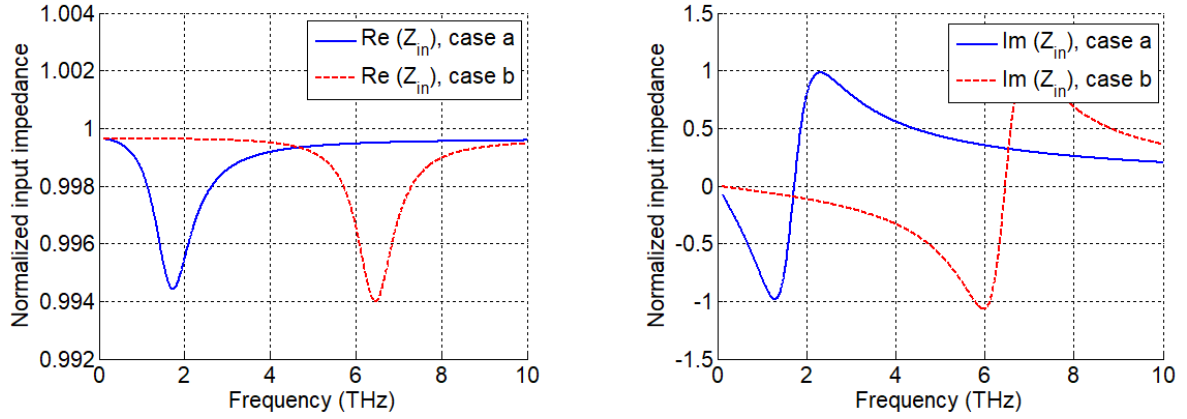


Figure 48: The normalized input impedance  $Z_{in}$  for the proposed structure: (a) The real part, (b) The imaginary part versus frequency for case a:  $W_n = 140 \text{ nm}$ ,  $W_{BP} = 120 \text{ nm}$ , and case b:  $W_n = 30 \text{ nm}$ ,  $W_{BP} = 15 \text{ nm}$

## Chapter 5 : Conclusion and Future Work

### 5.1 Conclusion

This work aimed at studying the properties of graphene heterostructures and their potential applications in the THz range. Since MoS<sub>2</sub> and phosphorene are the most recent and promising 2D materials that showed compatibility of graphene, they were the focus of this study. The optical band gap modulation of these materials (graphene, MoS<sub>2</sub>, and phosphorene) opened the door for their use in optical applications. The hexagonal structure of MoS<sub>2</sub> facilitates a vertical heterostructure integration with graphene that has a hexagonal honeycomb shape. Both graphene and phosphorene have a zigzag and armchair edges which simplifies their in-plane integration. In addition, these materials have favorable electronic, mechanical, and thermal properties.

The direction of the study was towards THz absorbers, as they represent a main building block in communication and electronic THz systems. After studying previous literature, it was found that very few work were done on selective or narrow band THz absorbers that are as much important as broadband and ultra-broad band absorbers that were the focus of most studies. Our study is a theoretical one that takes into consideration the simplicity of structure and possibility of integration to ensure the easiness of fabrication in the future. The models used are selected precisely to ensure a near real structure properties and the finite element method was used to simulate the proposed structure. The structure was modulated to obtain a selective absorber that can be easily tuned through an applied voltage and able to sweep the entire THz range.

The absorption of each 2D material was tested separately, and then combinations of these 2D materials were made to reach the maximum absorption. The fact that the band gap of graphene and phosphorene is greatly affected by the structure and dimensions (nanoribbons, rings, etc.) was exploited to adjust the absorption frequency in the THz range and the electrical optical tuning of graphene was used to ensure easy absorption frequency sweep.

The future fabrication of the proposed structure was highly considered while designing the structure. We focused on the simplicity of the structure where nanoribbons of 2D materials were used to avoid complex designs that were previously used. The

fabrication of graphene and phosphorene are successfully obtained on a wide scale using CVD that allow their stripping into the desired nanoribbon sizes. Numerous studies have documented the successful production of high-quality, thin films of graphene, MoS<sub>2</sub>, and phosphorene on SiO<sub>2</sub>/Si substrates through chemical vapor deposition (CVD) (Liao et al., 2013; Choi et al., 2017; Smith et al., 2016). While the CVD synthesis of phosphorene poses challenges, alternative methods such as pulsed layer deposition have demonstrated success in creating superior ultrathin films (Yang et al., 2015). The fabrication of nanoribbons from 2D materials has been achieved using traditional lithography techniques. In a comparative analysis by Celis et al. (2016), various approaches for synthesizing graphene nanoribbons, including lithography, catalytic cutting, chemical assembly, and epitaxial growth, were explored. An enhanced technique employing light-emitting diode (LED) lithography successfully generated damage-free thin nanoribbons of MoS<sub>2</sub> and graphene (Shi et al., 2023). Other methods are also under development, as evidenced by researchers Deng et al. (2022) who achieved the direct synthesis of single-crystalline MoTe<sub>2</sub> nanoribbon arrays on SiO<sub>2</sub>/Si substrates using a one-step CVD synthesis technique. A comprehensive review by Lee et al. (2017) discussed the assembly and transfer of graphene nanoribbons, comparing wet and dry transfer methods. A damage-free transfer technique, a roll-based transfer method was introduced (Kim et al., 2021), demonstrating effective transfer for graphene and MoS<sub>2</sub> sheets. The synthesis and transfer of high-quality phosphorene nanoribbons were accomplished through ionic scissoring of black phosphorous crystals (Watts et al., 2019). Diverse techniques for transferring black phosphorus, whether through dry or wet methods, were discussed in (Dhanabalan et al., 2017). Ongoing research endeavors aim to achieve a perfect and precise transfer of 2D materials on an industrial scale. Future work could also include modifying the design for better selectivity of the absorption frequency and narrower bandwidth.

## 5.2 Future Work (Synthesis)

As synthesizing is a part of the future work of this thesis, we here include the preparation of MoS<sub>2</sub> monolayer on SiO<sub>2</sub>/Si wafers using CVD as a first step for the whole structure fabrication. We were able to obtain a wide monolayer surface of MoS<sub>2</sub>. The monolayers can then be cut into nanoribbons and assembled with nanoribbons of

graphene and phosphorene. The synthesis was done in the institute of applied physics lab (IAP) at University Mohammed IV polytechnic (UM6P) using chemical vapor deposition (CVD). Synthesizing MoS<sub>2</sub> requires some preparations before starting the synthesis process, like cleaning the wafers, boats and the tubes that are going to be used during the synthesis Figure 49.

### *5.2.1 Cleaning Process before Synthesis*

- Cleaning SiO<sub>2</sub>/Si wafers

The SiO<sub>2</sub>/Si wafers used are of 300 nm thickness and are covered by a Cu layer. The Cu layer is removed through soaking the SiO<sub>2</sub>/Si wafer in HNO<sub>3</sub> for 1 hour then washing it with Deionized (DI) water and leaving it to dry. After that, RCA1 and RCA2 protocols are applied for complete wafer cleaning. RCA1 and RCA2 depends on mixing H<sub>2</sub>O, H<sub>2</sub>O<sub>2</sub>, and NH<sub>4</sub>OH or HCL in ratios 6:1:1 and here is the detailed procedure for each protocol.

#### RCA1

1. Mix the following amounts:
  - a. 90 ml of H<sub>2</sub>O
  - b. 15 ml of H<sub>2</sub>O<sub>2</sub>
  - c. 15 ml of NH<sub>4</sub>OH
2. Put the Silicon wafer in the above mixture and then on hot plate at 70 °C and leave for 15 minutes.
3. Remove the wafer from the mixture and leave to dry
4. Apply RCA2 which includes mixing the below amounts of solutions:
  - a. 90 ml of H<sub>2</sub>O
  - b. 15 ml of H<sub>2</sub>O<sub>2</sub>
  - c. 15 ml of HCL
5. Then repeat number 2 and 3.

6. Put the wafer in DI water and sonicate for 15 minutes
7. Leave the wafer to dry, then cut into pieces

- Cleaning the wafer pieces:

After applying the above protocols, now we have a clean Silicon wafer from Cu. To remove any left portions of Cu or dust the below steps are done before using the wafer pieces in the MoS<sub>2</sub> synthesis.

1. Merge the wafer pieces in acetone and sonicate for 15 minutes
  2. Remove the pieces and merge in Isopropyl alcohol (IP) and sonicate for 15 minutes.
  3. Then remove again and merge in ethanol and sonicate for 15 minutes.
  4. Merge in Deionized (DI) water and sonicate for 15 minutes.
  5. The wafer cleanliness is checked where no water drops stick on the surface.
  6. The wafer is put in oven for drying at 100 °C for 30 minutes.
- Cleaning the boats that will be used to carry Sulfur and Molybdenum oxide (MoO<sub>3</sub>)

The boats are immersed in ethanol and sonicated for 5 minutes then in DI water and sonicated for 5 minutes. Then put in the oven for drying at 100 °C for 30 minutes.

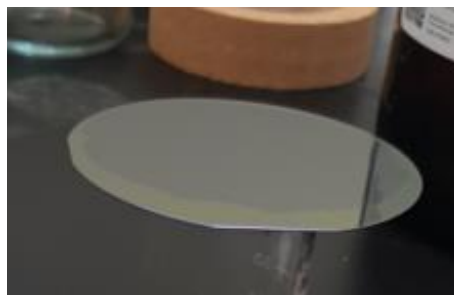
- Cleaning the quartz tube of the CVD

The CVD quartz tube is cleaned using acetone or ethanol with tissues.

(a)



(b)



(c)



(d)



(e)



(f)



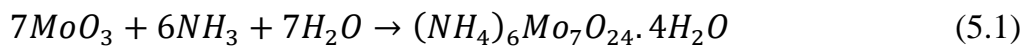
Figure 49: Cleaning process steps

(a) The acid mixture on the hot plate; (b) Leaving the wafer to dry after RCA1 and RCA2 cleaning; (c) The wafer pieces after RCA1 and RCA2 cleaning; (d) A boat that will carry Sulfur and MoO<sub>3</sub>; (e) Wafer piece merged in the solution; (f) Wafer piece and the boat when put in the sonicator at 45KHz frequency, temperature 0°C, and power 100%



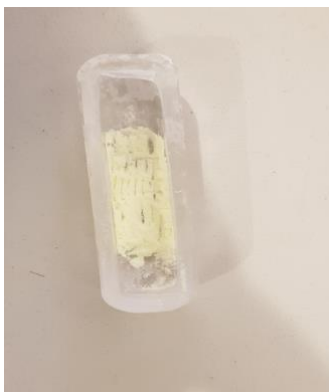
### 5.2.2 MoS<sub>2</sub> Synthesis

The synthesis of MoS<sub>2</sub> was processed using solution-processed precursor deposition using CVD (Seravalli & Bosi, 2021). A solution of 1.042 µl of ammonia 32% (ammonium hydroxide (NH<sub>4</sub>OH)) +50 mg of molybdenum (VI) oxide (MoO<sub>3</sub>) were mixed in a tube and sonicated for 5 minutes Equation (5.1). A 60 µl of the mixture was distributed over the wafer piece equally using a spin coater and left to completely dry then the wafer is put in oven for 20 minutes at 60 °C. After that the wafer chip is put on a clean boat Figure 50b. A 60 mg of Sulfur is put in another boat Figure 50a.



The CVD quartz tube is cleaned using acetone and the two boats are put at distances 62 cm and 32 cm for the wafer piece and the Sulfur boats respectively Figure 51. The temperature setting for the middle zone of the CVD is set as in Figure 52. The CVD tube is vacuumed and cleaned using N<sub>2</sub>, where both the rotary and diffusion pump are used. After reaching the required pressure ( $2.3 \times 10^{-1}$  Pascal). The furnace was operated with the middle zone while introducing N<sub>2</sub> as a carrier to transfer sulfur to Silicon wafer that has Molybdenum dropped solution over it. The N<sub>2</sub> flow is set to 20 SCCM at the beginning and increased to 70 SCCM when the temperature reaches 900 °C (processing time).

(a)



(b)

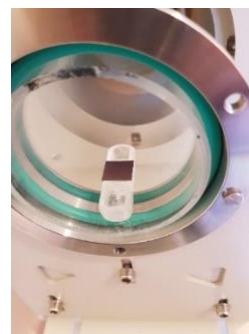


Figure 50: The Sulpher and the MoO<sub>3</sub> on chip

(a) 60 mg of Sulfur weighed in the boat; (b) A 60 µl of the solution (NH<sub>4</sub>OH+MoO<sub>3</sub>) dropped over the chip and put on the boat.

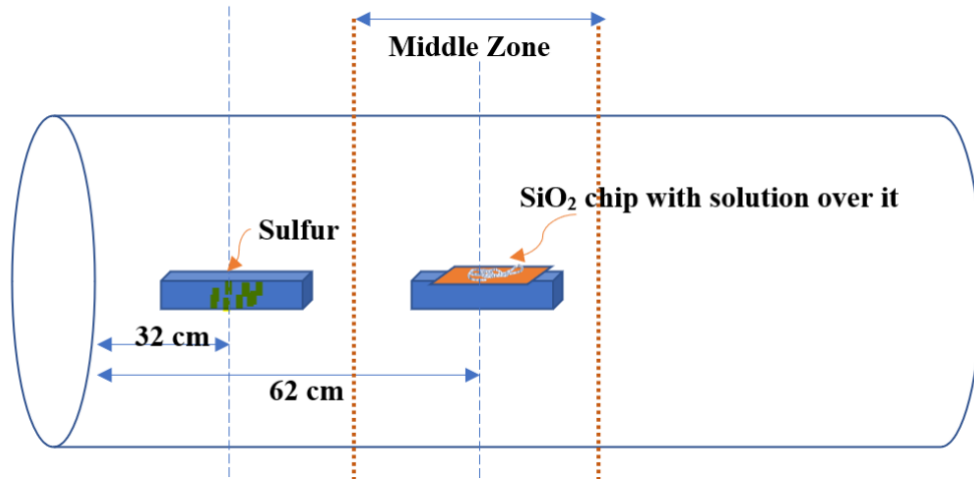


Figure 51: The positions of the boats carrying Sulfur and Silicon wafer in the CVD tube.

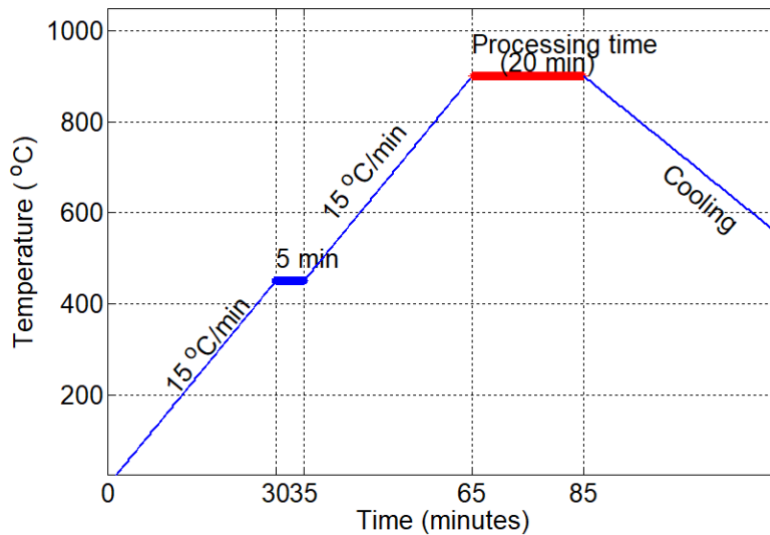


Figure 52: The temperature settings of the CVD middle zone furnace.

### 5.2.3 Experimental Results

The boundary structure of the grown MoS<sub>2</sub> monolayer can be either triangular or hexagonal (Cho et al., 2023; Li et al., 2020; Yang et al., 2022), the mentioned method in chapter 2 provides hexagonal boundary. The grown MoS<sub>2</sub> is shown in Figure 53, where there are a lot of Sulfur residuals. The chip was soaked in Toluene (C<sub>7</sub>H<sub>8</sub>) for 1 day, then sonicated for 15 minutes, then removed and left to dry Figure 54a, Some of the Sulfur was removed however we still have some Sulfur residuals. The last step was emerging

the chip in Ammonia for 3 hours, then sonicated for 15 minutes, and at the end washed by DI water Figure 54(b, c). Now we have a nearly clean MoS<sub>2</sub> monolayers with widths ranging from 18 to 200 μm.

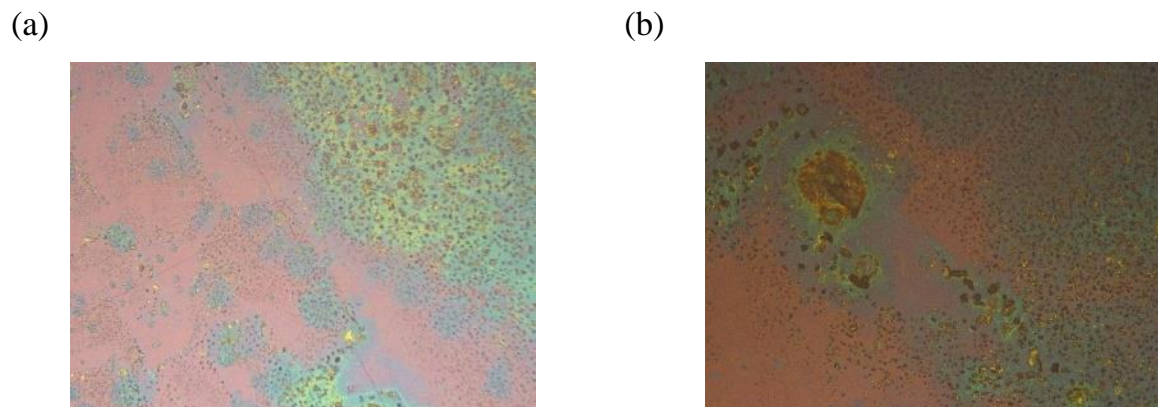


Figure 53: Different parts of the chip after growing MoS<sub>2</sub> using CVD; (a) In the middle; (b) In the corner.

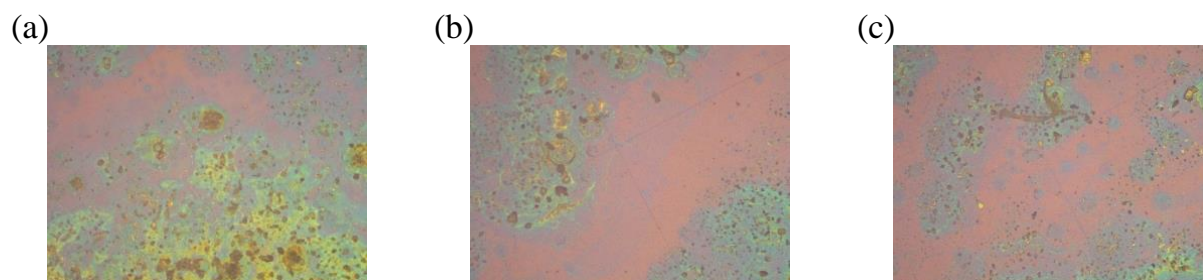


Figure 54: Different parts of the chip after cleaning with Toluene: (a) the Sulfur residuals are still obvious in this part of the chip; (b) and (c) Chip with less Sulfur after Toluene cleaning.

## References

- Ancker-Johnson, B. (1966). Chapter 11 Plasmas in Semiconductors and Semimetals. In R. K. Willardson & A. C. Beer (Eds.), *Semiconductors and Semimetals* (Vol. 1, pp. 379–481). Elsevier. [https://doi.org/10.1016/S0080-8784\(08\)62384-4](https://doi.org/10.1016/S0080-8784(08)62384-4)
- Andersen, K., Jacobsen, K. W., & Thygesen, K. S. (2014). Plasmons on the edge of MoS<sub>2</sub> nanostructures. *Physical Review B*, *90*(16), 161410. <https://doi.org/10.1103/PhysRevB.90.161410>
- Anju, S., Ashtami, J., & Mohanan, P. V. (2019). Black phosphorus, a prospective graphene substitute for biomedical applications. *Materials Science and Engineering: C*, *97*, 978–993. <https://doi.org/10.1016/j.msec.2018.12.146>
- Arsanjani, A., Biabanifard, M., & Abrishamian, M. S. (2019). A novel analytical method for designing a multi-band, polarization-insensitive and wide angle graphene-based THz absorber. *Superlattices and Microstructures*, *128*, 157–169. <https://doi.org/10.1016/j.spmi.2019.01.020>
- Baah, M., Paddubskaya, A., Novitsky, A., Valynets, N., Kumar, M., Itkonen, T., Pekkarinen, M., Soboleva, E., Lahderanta, E., Kafesaki, M., Svirko, Y., & Kuzhir, P. (2021). All-graphene perfect broadband THz absorber. *Carbon*, *185*, 709–716. <https://doi.org/10.1016/j.carbon.2021.09.067>
- Biswas, S., Whitney, W. S., Grajower, M. Y., Watanabe, K., Taniguchi, T., Bechtel, H. A., Rossman, G. R., & Atwater, H. A. (2021). Tunable intraband optical conductivity and polarization-dependent epsilon-near-zero behavior in black phosphorus. *Science Advances*, *7*(2), eabd4623. <https://doi.org/10.1126/sciadv.abd4623>
- Bollinger, M. V., Lauritsen, J. V., Jacobsen, K. W., Nørskov, J. K., Helveg, S., & Besenbacher, F. (2001). One-Dimensional Metallic Edge States in MoS<sub>2</sub>. *Physical Review Letters*, *87*(19), 196803. <https://doi.org/10.1103/PhysRevLett.87.196803>
- Cai, M., Thorpe, D., Adamson, D. H., & Schniepp, H. C. (2012). Methods of graphite exfoliation. *Journal of Materials Chemistry*, *22*(48), 24992. <https://doi.org/10.1039/c2jm34517j>

- Cao, T., Li, X., Liu, L., & Zhao, J. (2016). Electric field and strain tunable electronic structures in monolayer Black Phosphorus. *Computational Materials Science*, *112*, 297–303. <https://doi.org/10.1016/j.commatsci.2015.10.042>
- Cassabois, G., Valvin, P., & Gil, B. (2016). Hexagonal boron nitride is an indirect bandgap semiconductor. *Nature Photonics*, *10*(4), 262–266. <https://doi.org/10.1038/nphoton.2015.277>
- Celis, A., Nair, M. N., Taleb-Ibrahimi, A., Conrad, E. H., Berger, C., De Heer, W. A., & Tejeda, A. (2016). Graphene nanoribbons: Fabrication, properties and devices. *Journal of Physics D: Applied Physics*, *49*(14), 143001. <https://doi.org/10.1088/0022-3727/49/14/143001>
- Chaccour, C., Soorki, M. N., Saad, W., Bennis, M., Popovski, P., & Debbah, M. (2022). Seven Defining Features of Terahertz (THz) Wireless Systems: A Fellowship of Communication and Sensing. *IEEE Communications Surveys & Tutorials*, *24*(2), 967–993. <https://doi.org/10.1109/COMST.2022.3143454>
- Chen, D., Yang, J., Zhang, J., Huang, J., & Zhang, Z. (2017). Section 1 Tunable broadband terahertz absorbers based on multiple layers of graphene ribbons. *Scientific Reports*, *7*(1), 15836. <https://doi.org/10.1038/s41598-017-16220-9>
- Chen, F., Cheng, Y., & Luo, H. (2020). A Broadband Tunable Terahertz Metamaterial Absorber Based on Single-Layer Complementary Gammadion-Shaped Graphene. *Materials*, *13*(4), 860. <https://doi.org/10.3390/ma13040860>
- Chen, S., Fan, F., Miao, Y., He, X., Zhang, K., & Chang, S. (2016). Ultrasensitive terahertz modulation by silicon-grown MoS<sub>2</sub> nanosheets. *Nanoscale*, *8*(8), 4713–4719. <https://doi.org/10.1039/C5NR08101G>
- Cheng, Y., Gong, R., & Zhao, J. (2016). A photoexcited switchable perfect metamaterial absorber/reflector with polarization-independent and wide-angle for terahertz waves. *Optical Materials*, *62*, 28–33. <https://doi.org/10.1016/j.optmat.2016.09.042>
- Cheng, Y., Li, Z., & Cheng, Z. (2021). Terahertz perfect absorber based on InSb metasurface for both temperature and refractive index sensing. *Optical Materials*, *117*, 111129. <https://doi.org/10.1016/j.optmat.2021.111129>

- Cheng, Y., Qian, Y., Luo, H., Chen, F., & Cheng, Z. (2023). Terahertz narrowband perfect metasurface absorber based on micro-ring-shaped GaAs array for enhanced refractive index sensing. *Physica E: Low-Dimensional Systems and Nanostructures*, 146, 115527. <https://doi.org/10.1016/j.physe.2022.115527>
- Cheng, Y.-Y., Meng, D., Xu, M.-Y., Liu, Y., Zhuang, P.-P., Lin, D., Liu, J., & Chen, Y.-S. (2023). Wide-band and narrow-band switchable terahertz absorber based on graphene. *Results in Physics*, 52, 106838. <https://doi.org/10.1016/j.rinp.2023.106838>
- Chi Kao, K. (2004). *Dielectric Phenomena in Solids*. Elsevier. <https://doi.org/10.1016/B978-0-12-396561-5.X5010-5>
- Cho, Y. J., Sim, Y., Lee, J.-H., Hoang, N. T., & Seong, M.-J. (2023). Size and shape control of CVD-grown monolayer MoS<sub>2</sub>. *Current Applied Physics*, 45, 99–104. <https://doi.org/10.1016/j.cap.2022.11.008>
- Choi, S. H., Stephen, B., Park, J.-H., Lee, J. S., Kim, S. M., Yang, W., & Kim, K. K. (2017). Water-Assisted Synthesis of Molybdenum Disulfide Film with Single Organic Liquid Precursor. *Scientific Reports*, 7(1), 1983. <https://doi.org/10.1038/s41598-017-02228-8>
- Comsol. (2017, February 21). *Detailed Explanation of the Finite Element Method (FEM)*. Retrieved Nov. 15, 2023, from <https://www.comsol.com/multiphysics/finite-element-method?parent=physics-pdes-numerical-042-62>
- Cui, L., Wang, J., & Sun, M. (2021). Graphene plasmon for optoelectronics. *Reviews in Physics*, 6, 100054. <https://doi.org/10.1016/j.revip.2021.100054>
- Dagan, R., Vaknin, Y., Henning, A., Shang, J. Y., Lauhon, L. J., & Rosenwaks, Y. (2019). Two-dimensional charge carrier distribution in MoS<sub>2</sub> monolayer and multilayers. *Applied Physics Letters*, 114(10), 101602. <https://doi.org/10.1063/1.5078711>
- Davelou, D., Kopidakis, G., Kioseoglou, G., & Remediakis, I. N. (2014). MoS<sub>2</sub> nanostructures: Semiconductors with metallic edges. *Solid State Communications*, 192, 42–46. <https://doi.org/10.1016/j.ssc.2014.04.023>

- Davies, C. L., Patel, J. B., Xia, C. Q., Herz, L. M., & Johnston, M. B. (2018). Temperature-Dependent Refractive Index of Quartz at Terahertz Frequencies. *Journal of Infrared, Millimeter, and Terahertz Waves*, 39(12), 1236–1248. <https://doi.org/10.1007/s10762-018-0538-7>
- Debu, D. T., Bauman, S. J., French, D., Churchill, H. O. H., & Herzog, J. B. (2018). Tuning Infrared Plasmon Resonance of Black Phosphorene Nanoribbon with a Dielectric Interface. *Scientific Reports*, 8(1), 3224. <https://doi.org/10.1038/s41598-018-21365-2>
- Deng, Y., Zhu, C., Wang, Y., Wang, X., Zhao, X., Wu, Y., Tang, B., Duan, R., Zhou, K., & Liu, Z. (2022). Lithography-free, high-density MoTe<sub>2</sub> nanoribbon arrays. *Materials Today*, 58, 8–17. <https://doi.org/10.1016/j.mattod.2022.06.002>
- Dhanabalan, S. C., Ponraj, J. S., Guo, Z., Li, S., Bao, Q., & Zhang, H. (2017). Emerging Trends in Phosphorene Fabrication towards Next Generation Devices. *Advanced Science*, 4(6), 1600305. <https://doi.org/10.1002/advs.201600305>
- Dhriti, K. M., Kumar Chowdhary, A., Singh Chouhan, B., Sikdar, D., & Kumar, G. (2022). Tunable terahertz absorption modulation in graphene nanoribbon-assisted dielectric metamaterial. *Journal of Physics D: Applied Physics*, 55(28), 285101. <https://doi.org/10.1088/1361-6463/ac6636>
- Dou, X., Ding, K., Jiang, D., & Sun, B. (2014). Tuning and Identification of Interband Transitions in Monolayer and Bilayer Molybdenum Disulfide Using Hydrostatic Pressure. *ACS Nano*, 8(7), 7458–7464. <https://doi.org/10.1021/nn502717d>
- Dyakonov, M., & Shur, M. (1993). Shallow water analogy for a ballistic field effect transistor: New mechanism of plasma wave generation by dc current. *Physical Review Letters*, 71(15), 2465–2468. <https://doi.org/10.1103/PhysRevLett.71.2465>
- Dyakonov, M., & Shur, M. (1996). Detection, mixing, and frequency multiplication of terahertz radiation by two-dimensional electronic fluid. *IEEE Transactions on Electron Devices*, 43(3), 380–387. <https://doi.org/10.1109/16.485650>
- El Moutaouakil, A., Suemitsu, T., Otsuji, T., Videlier, H., Boubanga-Tombet, S.-A., Coquillat, D., & Knap, W. (2011). Device loading effect on nonresonant detection of terahertz radiation in dual grating gate plasmon-resonant structure using InGaP/InGaAs/GaAs material systems. *Physica Status Solidi (c)*, 8(2), 346–348. <https://doi.org/10.1002/pssc.201000569>

- El-Shenawee, M., Vohra, N., Bowman, T., & Bailey, K. (2019). Cancer detection in excised breast tumors using terahertz imaging and spectroscopy. *Biomedical Spectroscopy and Imaging*, 8(1–2), 1–9. <https://doi.org/10.3233/BSI-190187>
- Erande, M. B., Pawar, M. S., & Late, D. J. (2016). Humidity Sensing and Photodetection Behavior of Electrochemically Exfoliated Atomically Thin-Layered Black Phosphorus Nanosheets. *ACS Appl. Mater. Interfaces*.
- Fan, C., Jia, Y., Ren, P., & Jia, W. (2021). Tunable plasmon induced transparency and multispectral transparency with large group delay in graphene metamaterials. *Journal of Physics D: Applied Physics*, 54(3), 035107. <https://doi.org/10.1088/1361-6463/abba5b>
- Fang, T., Konar, A., Xing, H., & Jena, D. (2007a). Carrier Statistics and Quantum Capacitance of Graphene Sheets and Ribbons. *Applied Physics Letters*, 91(9), 092109. <https://doi.org/10.1063/1.2776887>
- Fang, T., Konar, A., Xing, H., & Jena, D. (2007b). Carrier Statistics and Quantum Capacitance of Graphene Sheets and Ribbons. *Applied Physics Letters*, 91(9), 092109. <https://doi.org/10.1063/1.2776887>
- Farooq, S., Rativa, D., Said, Z., & Araujo, R. E. D. (2022). Ultra-sensitive narrow-band plasmonic perfect absorber for sensing applications. *Photonics and Nanostructures - Fundamentals and Applications*, 50, 101018. <https://doi.org/10.1016/j.photonics.2022.101018>
- Garg, R., Dutta, N., & Choudhury, N. (2014). Work Function Engineering of Graphene. *Nanomaterials*, 4(2), 267–300. <https://doi.org/10.3390/nano4020267>
- Geng, X., Sun, W., Wu, W., Chen, B., Al-Hilo, A., Benamara, M., Zhu, H., Watanabe, F., Cui, J., & Chen, T. (2016). Pure and stable metallic phase molybdenum disulfide nanosheets for hydrogen evolution reaction. *Nature Communications*, 7(1), 10672. <https://doi.org/10.1038/ncomms10672>
- Gezimati, M., & Singh, G. (2023). Advances in terahertz technology for cancer detection applications. *Optical and Quantum Electronics*, 55(2), 151. <https://doi.org/10.1007/s11082-022-04340-0>
- Ghosh, B. (2014). *Basic plasma physics*. Alpha Science International.



- Gong, C., Zhan, M., Yang, J., Wang, Z., Liu, H., Zhao, Y., & Liu, W. (2016). Broadband terahertz metamaterial absorber based on sectional asymmetric structures. *Scientific Reports*, 6(1), 32466. <https://doi.org/10.1038/srep32466>
- Gupta, S., Johnston, A., & Khondaker, S. (2022). Optoelectronic Properties of MoS<sub>2</sub>/Graphene Heterostructures Prepared by Dry Transfer for Light-Induced Energy Applications. *Journal of Electronic Materials*, 51(8), 4257–4269. <https://doi.org/10.1007/s11664-022-09672-x>
- Gusakova, J., Wang, X., Shiau, L. L., Krivosheeva, A., Shaposhnikov, V., Borisenko, V., Gusakov, V., & Tay, B. K. (2017). Electronic Properties of Bulk and Monolayer TMDs: Theoretical Study Within DFT Framework (GVJ-2e Method). *Physica Status Solidi (a)*, 214(12), 1700218. <https://doi.org/10.1002/pssa.201700218>
- Hakoda, C., Rose, J., Shokouhi, P., & Lissenden, C. (2018). *Using Floquet periodicity to easily calculate dispersion curves and wave structures of homogeneous waveguides*. 020016. <https://doi.org/10.1063/1.5031513>
- Han, J. T., Jang, J. I., Kim, H., Hwang, J. Y., Yoo, H. K., Woo, J. S., Choi, S., Kim, H. Y., Jeong, H. J., Jeong, S. Y., Baeg, K.-J., Cho, K., & Lee, G.-W. (2015). Extremely Efficient Liquid Exfoliation and Dispersion of Layered Materials by Unusual Acoustic Cavitation. *Scientific Reports*, 4(1), 5133. <https://doi.org/10.1038/srep05133>
- Han, M. Y., Özyilmaz, B., Zhang, Y., & Kim, P. (2007). Energy Band-Gap Engineering of Graphene Nanoribbons. *Physical Review Letters*, 98(20), 206805. <https://doi.org/10.1103/PhysRevLett.98.206805>
- Hanson, G. W. (2008). Dyadic Green's Functions for an Anisotropic, Non-Local Model of Biased Graphene. *IEEE Transactions on Antennas and Propagation*, 56(3), 747–757. <https://doi.org/10.1109/TAP.2008.917005>
- He, Z., & Que, W. (2016). Molybdenum disulfide nanomaterials: Structures, properties, synthesis and recent progress on hydrogen evolution reaction. *Applied Materials Today*, 3, 23–56. <https://doi.org/10.1016/j.apmt.2016.02.001>
- Hijazi, A., & Moutaouakil, A. E. (2019). Graphene and MoS<sub>2</sub> Structures for THz Applications. *2019 44th International Conference on Infrared, Millimeter, and Terahertz Waves (IRMMW-THz)*, 1–2. <https://doi.org/10.1109/IRMMW-THz.2019.8873712>

- Islam, M. S., Sultana, J., Biabanifard, M., Vafapour, Z., Nine, M. J., Dinovitser, A., Cordeiro, C. M. B., Ng, B. W.-H., & Abbott, D. (2020). Tunable localized surface plasmon graphene metasurface for multiband superabsorption and terahertz sensing. *Carbon*, *158*, 559–567. <https://doi.org/10.1016/j.carbon.2019.11.026>
- Jatschka, J., Dathe, A., Csáki, A., Fritzsche, W., & Stranik, O. (2016). Propagating and localized surface plasmon resonance sensing—A critical comparison based on measurements and theory. *Sensing and Bio-Sensing Research*, *7*, 62–70. <https://doi.org/10.1016/j.sbsr.2016.01.003>
- Jin, W., Yeh, P.-C., Zaki, N., Chenet, D., Arefe, G., Hao, Y., Sala, A., Menten, T. O., Dadap, J. I., Locatelli, A., Hone, J., & Osgood, R. M. (2015). Tuning the electronic structure of monolayer graphene/ MoS<sub>2</sub> van der Waals heterostructures via interlayer twist. *Physical Review B*, *92*(20), 201409. <https://doi.org/10.1103/PhysRevB.92.201409>
- Khavasi, A. (2015a). Design of ultra-broadband graphene absorber using circuit theory. *Journal of the Optical Society of America B*, *32*(9), 1941. <https://doi.org/10.1364/JOSAB.32.001941>
- Khavasi, A. (2015b). Design of ultra-broadband graphene absorber using circuit theory. *Journal of the Optical Society of America B*, *32*(9), 1941. <https://doi.org/10.1364/JOSAB.32.001941>
- Khavasi, A., & Rejaei, B. (2014). Analytical Modeling of Graphene Ribbons as Optical Circuit Elements. *IEEE Journal of Quantum Electronics*, *50*(6), 397–403. <https://doi.org/10.1109/JQE.2014.2316133>
- Kim, C., Yoon, M.-A., Jang, B., Kim, H.-D., Kim, J.-H., Hoang, A. T., Ahn, J.-H., Jung, H.-J., Lee, H.-J., & Kim, K.-S. (2021). Damage-free transfer mechanics of 2-dimensional materials: Competition between adhesion instability and tensile strain. *NPG Asia Materials*, *13*(1), 44. <https://doi.org/10.1038/s41427-021-00311-1>
- Kim, H., Bae, H., Chang, T.-Y., & Huffaker, D. L. (2021). III–V nanowires on silicon (100) as plasmonic-photonic hybrid meta-absorber. *Scientific Reports*, *11*(1), 13813. <https://doi.org/10.1038/s41598-021-93398-z>

- Kim, J., Baik, S. S., Ryu, S. H., Sohn, Y., Park, S., Park, B.-G., Denlinger, J., Yi, Y., Choi, H. J., & Kim, K. S. (2015). Observation of tunable band gap and anisotropic Dirac semimetal state in black phosphorus. *Science*, *349*(6249), 723–726. <https://doi.org/10.1126/science.aaa6486>
- Kim, S. J., Kang, M.-A., Kim, S. H., Lee, Y., Song, W., Myung, S., Lee, S. S., Lim, J., & An, K.-S. (2016). Large-scale Growth and Simultaneous Doping of Molybdenum Disulfide Nanosheets. *Scientific Reports*, *6*(1), 24054. <https://doi.org/10.1038/srep24054>
- Korotcenkov, G. (2019). Black Phosphorus-New Nanostructured Material for Humidity Sensors: Achievements and Limitations. *Sensors*, *19*(5), 1010. <https://doi.org/10.3390/s19051010>
- Kumar, P., Bhadoria, B. S., Kumar, S., Bhowmick, S., Chauhan, Y. S., & Agarwal, A. (2016). Thickness and electric field dependent polarizability and dielectric constant in phosphorene. *Physical Review B*, *93*(19), 195428. <https://doi.org/10.1103/PhysRevB.93.195428>
- Laturia, A., Van De Put, M. L., & Vandenberghe, W. G. (2018). Dielectric properties of hexagonal boron nitride and transition metal dichalcogenides: From monolayer to bulk. *Npj 2D Materials and Applications*, *2*(1), 6. <https://doi.org/10.1038/s41699-018-0050-x>
- Lee, H. C., Liu, W.-W., Chai, S.-P., Mohamed, A. R., Aziz, A., Khe, C.-S., Hidayah, N. M. S., & Hashim, U. (2017). Review of the synthesis, transfer, characterization and growth mechanisms of single and multilayer graphene. *RSC Advances*, *7*(26), 15644–15693. <https://doi.org/10.1039/C7RA00392G>
- Li, J., Hu, S., Chen, Z., Liang, Y., Kang, H., Zhang, Y., Sui, Y., Wang, S., Yu, G., Peng, S., Jin, Z., & Liu, X. (2020). Facile and rigorous route to distinguish the boundary structure of monolayer MoS<sub>2</sub> domains by oxygen etching. *Applied Surface Science*, *510*, 145412. <https://doi.org/10.1016/j.apsusc.2020.145412>
- Li, J., Ji, Q., Chu, S., Zhang, Y., Li, Y., Gong, Q., Liu, K., & Shi, K. (2016). Tuning the photo-response in monolayer MoS<sub>2</sub> by plasmonic nano-antenna. *Scientific Reports*, *6*(1), 23626. <https://doi.org/10.1038/srep23626>

- Li, T., Zhou, J., Zheng, Y., Zhu, Z., Zhou, L., Rao, X., & Wang, J. (2019). Temperature Dependent Sheet Conductivity of MoS<sub>2</sub> Measured by Terahertz Time-Domain Spectroscopy. *2019 44th International Conference on Infrared, Millimeter, and Terahertz Waves (IRMMW-THz)*, 1–2. <https://doi.org/10.1109/IRMMW-THz.2019.8873920>
- Liao, C.-D., Lu, Y.-Y., Tamalampudi, S. R., Cheng, H.-C., & Chen, Y.-T. (2013). Chemical Vapor Deposition Synthesis and Raman Spectroscopic Characterization of Large-Area Graphene Sheets. *The Journal of Physical Chemistry A*, *117*(39), 9454–9461. <https://doi.org/10.1021/jp311757r>
- Lin, C., Grassi, R., Low, T., & Helmy, A. S. (2016). Multilayer Black Phosphorus as a Versatile Mid-Infrared Electro-optic Material. *Nano Letters*, *16*(3), 1683–1689. <https://doi.org/10.1021/acs.nanolett.5b04594>
- Lin, Y.-C., Torsi, R., Younas, R., Hinkle, C. L., Rigosi, A. F., Hill, H. M., Zhang, K., Huang, S., Shuck, C. E., Chen, C., Lin, Y.-H., Maldonado-Lopez, D., Mendoza-Cortes, J. L., Ferrier, J., Kar, S., Nayir, N., Rajabpour, S., Van Duin, A. C. T., Liu, X., ... Robinson, J. A. (2023). Recent Advances in 2D Material Theory, Synthesis, Properties, and Applications. *ACS Nano*, *17*(11), 9694–9747. <https://doi.org/10.1021/acsnano.2c12759>
- Liu, H.-L., Yang, T., Chen, J.-H., Chen, H.-W., Guo, H., Saito, R., Li, M.-Y., & Li, L.-J. (2020). Temperature-dependent optical constants of monolayer MoS<sub>2</sub>, MoSe<sub>2</sub>, WS<sub>2</sub>, and WSe<sub>2</sub>: Spectroscopic ellipsometry and first-principles calculations. *Scientific Reports*, *10*(1), 15282. <https://doi.org/10.1038/s41598-020-71808-y>
- Liu, L. (2019, December 30). What Is the Curl Element (and Why Is It Used)? *COMSOL*. Retrieved Nov. 15, 2023, from <https://www.comsol.com/blogs/what-is-the-curl-element-and-why-is-it-used/>
- Liu, Q., Li, L., Li, Y., Gao, Z., Chen, Z., & Lu, J. (2012). Tuning Electronic Structure of Bilayer MoS<sub>2</sub> by Vertical Electric Field: A First-Principles Investigation. *The Journal of Physical Chemistry C*, *116*(40), 21556–21562. <https://doi.org/10.1021/jp307124d>
- Low, T., Rodin, A. S., Carvalho, A., Jiang, Y., Wang, H., Xia, F., & Castro Neto, A. H. (2014). Tunable optical properties of multilayer black phosphorus thin films. *Physical Review B*, *90*(7), 075434. <https://doi.org/10.1103/PhysRevB.90.075434>

- Luo, S., Zhao, J., Zuo, D., & Wang, X. (2016). Perfect narrow band absorber for sensing applications. *Optics Express*, 24(9), 9288. <https://doi.org/10.1364/OE.24.009288>
- Maffucci, A., & Miano, G. (2013). Transmission Line Model of Graphene Nanoribbon Interconnects. *Nanoscience and Nanotechnology Letters*, 5(11), 1207–1216. <https://doi.org/10.1166/nnl.2013.1700>
- Maier, S. A. (2007). *Plasmonics: Fundamentals and Applications*. Springer US. <https://doi.org/10.1007/0-387-37825-1>
- Mansuripur, M., & Zakharian, A. R. (2009). Maxwell's macroscopic equations, the energy-momentum postulates, and the Lorentz law of force. *Physical Review E*, 79(2), 026608. <https://doi.org/10.1103/PhysRevE.79.026608>
- Matthaiakakis, N., Mizuta, H., & Charlton, M. D. B. (2016). Strong modulation of plasmons in Graphene with the use of an Inverted pyramid array diffraction grating. *Scientific Reports*, 6(1), 27550. <https://doi.org/10.1038/srep27550>
- Mohd Halim, S. N., Ahmad, F., Lokman, M. Q., Sapingi, H. H. J., Mohamad Taib, M. F., Wan Nawawi, W. M. F., Yahaya, H., Abdul Rahman, M. A., Shafie, S., & Harun, S. W. (2022). First Principles Study and Experimental Investigation of Graphene-Molybdenum Disulphide Nanocomposites Based Passive Saturable Absorber. *Photonics*, 9(10), 704. <https://doi.org/10.3390/photonics9100704>
- Mohsen Daraei, O., Goudarzi, K., & Bemani, M. (2020). A tunable ultra-broadband terahertz absorber based on two layers of graphene ribbons. *Optics & Laser Technology*, 122, 105853. <https://doi.org/10.1016/j.optlastec.2019.105853>
- Molaei, M. J., Younas, M., & Rezakazemi, M. (2021). A Comprehensive Review on Recent Advances in Two-Dimensional (2D) Hexagonal Boron Nitride. *ACS Applied Electronic Materials*, 3(12), 5165–5187. <https://doi.org/10.1021/acsaelm.1c00720>
- Moutaouakil, A. E. (2018). Two-Dimensional Electronic Materials for Terahertz Applications: Linking the Physical Properties with Engineering Expertise. *2018 6th International Renewable and Sustainable Energy Conference (IRSEC)*, 1–4. <https://doi.org/10.1109/IRSEC.2018.8702954>

- Moutaouakil, A. E., Fukidome, H., & Otsuji, T. (2020). Investigation of Terahertz properties in Graphene ribbons. *2020 45th International Conference on Infrared, Millimeter, and Terahertz Waves (IRMMW-THz)*, 1–2. <https://doi.org/10.1109/IRMMW-THz46771.2020.9370592>
- Moutaouakil, A. E., Komori, T., Horiike, K., Suemitsu, T., & Otsuji, T. (2010). Room Temperature Intense Terahertz Emission from a Dual Grating Gate Plasmon-Resonant Emitter Using InAlAs/InGaAs/InP Material Systems. *IEICE Transactions on Electronics, E93.C(8)*, 1286–1289. <https://doi.org/10.1587/transele.E93.C.1286>
- Moutaouakil, A. E., Suemitsu, T., Otsuji, T., Coquillat, D., & Knap, W. (2010). Room temperature terahertz detection in high-electron-mobility transistor structure using InAlAs/InGaAs/InP material systems. *35th International Conference on Infrared, Millimeter, and Terahertz Waves*, 1–2. <https://doi.org/10.1109/ICIMW.2010.5612598>
- Moutaouakil, A. E., Suemitsu, T., Otsuji, T., Coquillat, D., & Knap, W. (2012). Nonresonant Detection of Terahertz Radiation in High-Electron-Mobility Transistor Structure Using InAlAs/InGaAs/InP Material Systems at Room Temperature. *Journal of Nanoscience and Nanotechnology*, *12(8)*, 6737–6740. <https://doi.org/10.1166/jnn.2012.4575>
- Moutaouakil, A. E., Watanabe, T., Haibo, C., Komori, T., Nishimura, T., Suemitsu, T., & Otsuji, T. (2009). Spectral narrowing of terahertz emission from super-grating dual-gate plasmon-resonant high-electron mobility transistors. *Journal of Physics: Conference Series*, *193*, 012068. <https://doi.org/10.1088/1742-6596/193/1/012068>
- Mu, X., Wang, J., & Sun, M. (2019). Two-dimensional black phosphorus: Physical properties and applications. *Materials Today Physics*, *8*, 92–111. <https://doi.org/10.1016/j.mtphys.2019.02.003>
- Muñoz, R., López-Elvira, E., Munuera, C., Frisenda, R., Sánchez-Sánchez, C., Martín-Gago, J. Á., & García-Hernández, M. (2022). Direct growth of graphene-MoS<sub>2</sub> heterostructure: Tailored interface for advanced devices. *Applied Surface Science*, *581*, 151858. <https://doi.org/10.1016/j.apsusc.2021.151858>
- Naftaly, M., Leist, J., & Dudley, R. (2011). Hexagonal boron nitride studied by terahertz time-domain spectroscopy. *Journal of Physics: Conference Series*, *310*, 012006. <https://doi.org/10.1088/1742-6596/310/1/012006>

- Naikoo, G. A., Arshad, F., Almas, M., Hassan, I. U., Pedram, M. Z., Aljabali, A. A. A., Mishra, V., Serrano-Aroca, Á., Birkett, M., Charbe, N. B., Goyal, R., Negi, P., El-Tanani, M., & Tambuwala, M. M. (2022). 2D materials, synthesis, characterization and toxicity: A critical review. *Chemico-Biological Interactions*, 365, 110081. <https://doi.org/10.1016/j.cbi.2022.110081>
- Newaz, A. K. M., Prasai, D., Ziegler, J. I., Caudel, D., Robinson, S., Haglund Jr, R. F., & Bolotin, K. I. (2013). Electrical Control of Optical Properties of Monolayer MoS<sub>2</sub>. *Solid State Communications*, 155, 49–52. <https://doi.org/10.1016/j.ssc.2012.11.010>
- Novoselov, K. S., Geim, A. K., Morozov, S. V., Jiang, D., Zhang, Y., Dubonos, S. V., Grigorieva, I. V., & Firsov, A. A. (2004). Electric Field Effect in Atomically Thin Carbon Films. *Science*, 306(5696), 666–669. <https://doi.org/10.1126/science.1102896>
- Ouda, Muhammad. (2007.). Review of recent studies of mobile phones' health effects /Gaza, Palestine : Islamic University of Gaza, Faculty of Engineering.
- Gollapalli, R., Wei, T., & Reid, J. (2022). Application of Electric Bias to Enhance the Sensitivity of Graphene-Based Surface Plasmon Resonance Sensors. In *Graphene—Recent Advances, Future Perspective and Applied Applications [Working Title]*. IntechOpen. <https://doi.org/10.5772/intechopen.106556>
- Pham, T., Ramnani, P., Villarreal, C. C., Lopez, J., Das, P., Lee, I., Neupane, M. R., Rheem, Y., & Mulchandani, A. (2019). MoS<sub>2</sub>-graphene heterostructures as efficient organic compounds sensing 2D materials. *Carbon*, 142, 504–512. <https://doi.org/10.1016/j.carbon.2018.10.079>
- Phuong, L. T. T., Phong, T. C., & Yarmohammadi, M. (2020). Spin-splitting effects on the interband optical conductivity and activity of phosphorene. *Scientific Reports*, 10(1), 9201. <https://doi.org/10.1038/s41598-020-65951-9>
- Pierucci, D., Henck, H., Avila, J., Balan, A., Naylor, C. H., Patriarche, G., Dappe, Y. J., Silly, M. G., Sirotti, F., Johnson, A. T. C., Asensio, M. C., & Ouerghi, A. (2016). Band Alignment and Minigaps in Monolayer MoS<sub>2</sub> -Graphene van der Waals Heterostructures. *Nano Letters*, 16(7), 4054–4061. <https://doi.org/10.1021/acs.nanolett.6b00609>

- Popov, V. V., Bagaeva, T. Yu., Otsuji, T., & Ryzhii, V. (2010a). Oblique terahertz plasmons in graphene nanoribbon arrays. *Physical Review B*, *81*(7), 073404. <https://doi.org/10.1103/PhysRevB.81.073404>
- Popov, V. V., Bagaeva, T. Yu., Otsuji, T., & Ryzhii, V. (2010b). Oblique terahertz plasmons in graphene nanoribbon arrays. *Physical Review B*, *81*(7), 073404. <https://doi.org/10.1103/PhysRevB.81.073404>
- Qiao, J., Kong, X., Hu, Z.-X., Yang, F., & Ji, W. (2014). High-mobility transport anisotropy and linear dichroism in few-layer black phosphorus. *Nature Communications*, *5*(1), 4475. <https://doi.org/10.1038/ncomms5475>
- Reshetnyak, V. Yu., Zadorozhnii, V. I., Pinkevych, I. P., Bunning, T. J., & Evans, D. R. (2018). Surface plasmon absorption in MoS<sub>2</sub> and graphene-MoS<sub>2</sub> micro-gratings and the impact of a liquid crystal substrate. *AIP Advances*, *8*(4), 045024. <https://doi.org/10.1063/1.5032297>
- Rossi, T. P., Winther, K. T., Jacobsen, K. W., Nieminen, R. M., Puska, M. J., & Thygesen, K. S. (2017). Effect of edge plasmons on the optical properties of MoS<sub>2</sub> monolayer flakes. *Physical Review B*, *96*(15), 155407. <https://doi.org/10.1103/PhysRevB.96.155407>
- Samy, O., Belmoubarik, M., Otsuji, T., & El Moutaouakil, A. (2023). A Voltage-Tuned Terahertz Absorber Based on MoS<sub>2</sub>/Graphene Nanoribbon Structure. *Nanomaterials*, *13*(11), 1716. <https://doi.org/10.3390/nano13111716>
- Samy, O., Birowosuto, D., & El Moutaouakil, A. (2021). A short review on Molybdenum disulfide (MoS<sub>2</sub>) applications and challenges. *2021 6th International Conference on Renewable Energy: Generation and Applications (ICREGA)*, 220–222. <https://doi.org/10.1109/ICREGA50506.2021.9388220>
- Samy, O., & El Moutaouakil, A. (2021). A Review on MoS<sub>2</sub> Energy Applications: Recent Developments and Challenges. *Energies*, *14*(15), 4586. <https://doi.org/10.3390/en14154586>
- Samy, O., Otsuji, T., & El Moutaouakil, A. (2023). Terahertz Absorptance in MoS<sub>2</sub> /Graphene Nanoribbon Heterostructures. *2023 Photonics & Electromagnetics Research Symposium (PIERS)*, 2031–2036. <https://doi.org/10.1109/PIERS59004.2023.10221462>



- Samy, O., Otsuji, T., & Moutaouakil, A. E. (2023). Near-Perfect THz Absorber with Wide Range Tunability. *2023 48th International Conference on Infrared, Millimeter, and Terahertz Waves (IRMMW-THz)*, 1–2. <https://doi.org/10.1109/IRMMW-THz57677.2023.10298957>
- Samy, O., Zeng, S., Birowosuto, M. D., & El Moutaouakil, A. (2021). A Review on MoS<sub>2</sub> Properties, Synthesis, Sensing Applications and Challenges. *Crystals*, *11*(4), 355. <https://doi.org/10.3390/cryst11040355>
- Satawara, A. M., Shaikh, G. A., Gupta, S. K., & Gajjar, P. N. (2021). Structural, electronic and optical properties of hexagonal boron-nitride (h-BN) monolayer: An Ab-initio study. *Materials Today: Proceedings*, *47*, 529–532. <https://doi.org/10.1016/j.matpr.2020.10.589>
- Seravalli, L., & Bosi, M. (2021). A Review on Chemical Vapour Deposition of Two-Dimensional MoS<sub>2</sub> Flakes. *Materials*, *14*(24), 7590. <https://doi.org/10.3390/ma14247590>
- Shangguan, Q., Chen, Z., Yang, H., Cheng, S., Yang, W., Yi, Z., Wu, X., Wang, S., Yi, Y., & Wu, P. (2022). Design of Ultra-Narrow Band Graphene Refractive Index Sensor. *Sensors*, *22*(17), 6483. <https://doi.org/10.3390/s22176483>
- Shi, Y., Taniguchi, T., Byun, K.-N., Kurimoto, D., Yamamoto, E., Kobayashi, M., Tsukagoshi, K., & Osada, M. (2023). Damage-free LED lithography for atomically thin 2D material devices. *Scientific Reports*, *13*(1), 2583. <https://doi.org/10.1038/s41598-023-29281-w>
- Smith, J. B., Hagaman, D., & Ji, H.-F. (2016). Growth of 2D black phosphorus film from chemical vapor deposition. *Nanotechnology*, *27*(21), 215602. <https://doi.org/10.1088/0957-4484/27/21/215602>
- Solis, D. M., Taboada, J. M., Landesa, L., Rodriguez, J. L., & Obelleiro, F. (2015). Squeezing Maxwell's Equations into the Nanoscale. *Progress In Electromagnetics Research*, *154*.
- Son, Y.-W., Cohen, M. L., & Louie, S. G. (2006). Energy Gaps in Graphene Nanoribbons. *Physical Review Letters*, *97*(21), 216803. <https://doi.org/10.1103/PhysRevLett.97.216803>

- Song, B., Gu, H., Fang, M., Chen, X., Jiang, H., Wang, R., Zhai, T., Ho, Y.-T., & Liu, S. (2019). Layer-Dependent Dielectric Function of Wafer-Scale 2D MoS<sub>2</sub>. *Advanced Optical Materials*, 7(2), 1801250. <https://doi.org/10.1002/adom.201801250>
- Tao, Z. H., Dong, H. M., Duan, Y. F., Huang, F., & Liu, J. L. (2019). Four Terahertz Plasmon Modes of Hole Gas in Monolayer MoS<sub>2</sub>. *Plasmonics*, 14(4), 839–843. <https://doi.org/10.1007/s11468-018-0864-6>
- Thongrattanasiri, S., Manjavacas, A., & García De Abajo, F. J. (2012). Quantum Finite-Size Effects in Graphene Plasmons. *ACS Nano*, 6(2), 1766–1775. <https://doi.org/10.1021/nn204780e>
- Tian, X., Liu, L., Du, Y., Gu, J., Xu, J., & Yakobson, B. I. (2015). Variable electronic properties of lateral phosphorene–graphene heterostructures. *Physical Chemistry Chemical Physics*, 17(47), 31685–31692. <https://doi.org/10.1039/C5CP05443E>
- Tinoco, M., Maduro, L., & Conesa-Boj, S. (2019). Metallic edge states in zig-zag vertically-oriented MoS<sub>2</sub> nanowalls. *Scientific Reports*, 9(1), 15602. <https://doi.org/10.1038/s41598-019-52119-3>
- Ullah, Z., Nawi, I., Witjaksono, G., Tansu, N., Khattak, M. I., Junaid, M., Siddiqui, M. A., & Magsi, S. A. (2020). Dynamic Absorption Enhancement and Equivalent Resonant Circuit Modeling of Tunable Graphene-Metal Hybrid Antenna. *Sensors*, 20(11), 3187. <https://doi.org/10.3390/s20113187>
- Urade, A. R., Lahiri, I., & Suresh, K. S. (2022). Graphene Properties, Synthesis and Applications: A Review. *JOM*. <https://doi.org/10.1007/s11837-022-05505-8>
- Viji, J., & Anujan, T. (2023). A Review on Electromagnetic Metamaterial Absorbers. *2023 International Conference on Control, Communication and Computing (ICCC)*, 1–4. <https://doi.org/10.1109/ICCC57789.2023.10165509>
- Wang, H., Liang, H., & Qian, Z. (2020). Tunable Conductivity and Dielectric Constant of Graphene in Microwave, Millimeter wave and Terahertz Band. *2020 13th UK-Europe-China Workshop on Millimetre-Waves and Terahertz Technologies (UCMMT)*, 1–3. <https://doi.org/10.1109/UCMMT49983.2020.9296081>
- Wang, J., & Jiang, Y. (2019). A phosphorene-based metasurface absorber operating in ultra-wideband terahertz regime. *The European Physical Journal D*, 73(12), 255. <https://doi.org/10.1140/epjd/e2019-100352-8>

- Wang, J., Yao, Y., Liu, X., Liu, G., & Liu, Z. (2023). Switchable Wideband Terahertz Absorber Based on Refractory and Vanadium Dioxide Metamaterials. *IEEE Photonics Journal*, 15(1), 1–6. <https://doi.org/10.1109/JPHOT.2023.3234535>
- Wang, T., Qu, L., Qu, L., Zhang, Y., Zhang, H., & Cao, M. (2020). Tunable broadband terahertz metamaterial absorber using multi-layer black phosphorus and vanadium dioxide. *Journal of Physics D: Applied Physics*, 53(14), 145105. <https://doi.org/10.1088/1361-6463/ab6af4>
- Watts, M. C., Picco, L., Russell-Pavier, F. S., Cullen, P. L., Miller, T. S., Bartuś, S. P., Payton, O. D., Skipper, N. T., Tileli, V., & Howard, C. A. (2019). Production of phosphorene nanoribbons. *Nature*, 568(7751), 216–220. <https://doi.org/10.1038/s41586-019-1074-x>
- Wen, Q.-Y., Xie, Y.-S., Zhang, H.-W., Yang, Q.-H., Li, Y.-X., & Liu, Y.-L. (2009). Transmission line model and fields analysis of metamaterial absorber in the terahertz band. *Optics Express*, 17(22), 20256. <https://doi.org/10.1364/OE.17.020256>
- Wu, D., Li, R., Liu, Y., Yu, Z., Yu, L., Chen, L., Liu, C., Ma, R., & Ye, H. (2017). Ultra-narrow Band Perfect Absorber and Its Application as Plasmonic Sensor in the Visible Region. *Nanoscale Research Letters*, 12(1), 427. <https://doi.org/10.1186/s11671-017-2203-9>
- Wu, Q., Ling, F., Zhang, C., Zhong, Z., & Zhang, B. (2023). Water-based metamaterials absorber with broadband absorption in terahertz region. *Optics Communications*, 526, 128874. <https://doi.org/10.1016/j.optcom.2022.128874>
- Xiao, S., Liu, T., Cheng, L., Zhou, C., Jiang, X., Li, Z., & Xu, C. (2019). Tunable anisotropic perfect absorption in hyperbolic metamaterials based on black phosphorous/dielectric multilayer structures. *Journal of Lightwave Technology*, 37(13), 3290–3297. <https://doi.org/10.1109/JLT.2019.2914183>
- Xu, B., Gu, C., Li, Z., & Niu, Z. (2013). A novel structure for tunable terahertz absorber based on graphene. *Optics Express*, 21(20), 23803. <https://doi.org/10.1364/OE.21.023803>

- Xu, Q., Ma, T., Danesh, M., Shivananju, B. N., Gan, S., Song, J., Qiu, C.-W., Cheng, H.-M., Ren, W., & Bao, Q. (2016). Effects of edge on graphene plasmons as revealed by infrared nanoimaging. *Light: Science & Applications*, 6(2), e16204–e16204. <https://doi.org/10.1038/lsa.2016.204>
- Yan, D., Meng, M., Li, J., & Li, X. (2020). Graphene-Assisted Narrow Bandwidth Dual-Band Tunable Terahertz Metamaterial Absorber. *Frontiers in Physics*, 8, 306. <https://doi.org/10.3389/fphy.2020.00306>
- Yang, H., Wang, Y., Tiu, Z. C., Tan, S. J., Yuan, L., & Zhang, H. (2022). All-Optical Modulation Technology Based on 2D Layered Materials. *Micromachines*, 13(1), 92. <https://doi.org/10.3390/mi13010092>
- Yang, P., Wang, D., Zhao, X., Quan, W., Jiang, Q., Li, X., Tang, B., Hu, J., Zhu, L., Pan, S., Shi, Y., Huan, Y., Cui, F., Qiao, S., Chen, Q., Liu, Z., Zou, X., & Zhang, Y. (2022). Epitaxial growth of inch-scale single-crystal transition metal dichalcogenides through the patching of unidirectionally orientated ribbons. *Nature Communications*, 13(1), 3238. <https://doi.org/10.1038/s41467-022-30900-9>
- Yang, Z., Hao, J., Yuan, S., Lin, S., Yau, H. M., Dai, J., & Lau, S. P. (2015). Field-Effect Transistors Based on Amorphous Black Phosphorus Ultrathin Films by Pulsed Laser Deposition. *Advanced Materials*, 27(25), 3748–3754. <https://doi.org/10.1002/adma.201500990>
- Yong, Z., Zhang, S., Gong, C., & He, S. (2016). Narrow band perfect absorber for maximum localized magnetic and electric field enhancement and sensing applications. *Scientific Reports*, 6(1), 24063. <https://doi.org/10.1038/srep24063>
- Yu, L., Hao, L., Meiqiong, T., Jiaoqi, H., Wei, L., Jinying, D., Xueping, C., Weiling, F., & Yang, Z. (2019). The medical application of terahertz technology in non-invasive detection of cells and tissues: Opportunities and challenges. *RSC Advances*, 9(17), 9354–9363. <https://doi.org/10.1039/C8RA10605C>
- Yu, X., Zhao, G., Gong, S., Liu, C., Wu, C., Lyu, P., Maurin, G., & Zhang, N. (2020). Design of MoS<sub>2</sub>/Graphene van der Waals Heterostructure as Highly Efficient and Stable Electrocatalyst for Hydrogen Evolution in Acidic and Alkaline Media. *ACS Applied Materials & Interfaces*, 12(22), 24777–24785. <https://doi.org/10.1021/acsami.0c04838>

- Zheng, S., Zhao, Q., Peng, L., & Jiang, X. (2021). Tunable plasmon induced transparency with high transmittance in a two-layer graphene structure. *Results in Physics*, 23, 104040. <https://doi.org/10.1016/j.rinp.2021.104040>
- Zhong, Y., Huang, Y., Zhong, S., Lin, T., Luo, M., Shen, Y., & Ding, J. (2021). Tunable terahertz broadband absorber based on MoS<sub>2</sub> ring-cross array structure. *Optical Materials*, 114, 110996. <https://doi.org/10.1016/j.optmat.2021.110996>
- Zhou, R., Peng, J., Yang, S., Liu, D., Xiao, Y., & Cao, G. (2018). Lifetime and nonlinearity of modulated surface plasmon for black phosphorus sensing application. *Nanoscale*, 10(39), 18878–18891. <https://doi.org/10.1039/C8NR06796A>
- Zhu, J., Yin, J., & Wu, C. (2022). Tunable Perfect Absorber of Graphene Metamaterial in the Terahertz Band and Its Sensing Properties. *Advanced Photonics Research*, 3(4), 2100291. <https://doi.org/10.1002/adpr.202100291>

## List of Publications

### Journal Publications

- Samy, O., & El Moutaouakil, A. (2024). A graphene-based THz selective absorber with absorptivity 95% and wide-range electrical tunability. *Results in Physics*, 58, 107490. <https://doi.org/10.1016/j.rinp.2024.107490>
- Samy, O., Belmoubarik, M., Otsuji, T., & El Moutaouakil, A. (2023). A Voltage-Tuned Terahertz Absorber Based on MoS<sub>2</sub>/Graphene Nanoribbon Structure. *Nanomaterials*, 13(11), 1716. <https://doi.org/10.3390/nano13111716>
- Jonathan, L., Diguna, L. J., Samy, O., Muqoyyanah, M., Abu Bakar, S., Birowosuto, M. D., & El Moutaouakil, A. (2022). Hybrid Organic–Inorganic Perovskite Halide Materials for Photovoltaics towards Their Commercialization. *Polymers*, 14(5). <https://doi.org/10.3390/polym14051059>
- Samy, O., Zeng, S., Birowosuto, M. D., & El Moutaouakil, A. (2021). A Review on MoS<sub>2</sub> Properties, Synthesis, Sensing Applications and Challenges. *Crystals*, 11(4), 355. <https://doi.org/10.3390/cryst11040355>
- Samy, O., & El Moutaouakil, A. (2021). A Review on MoS<sub>2</sub> Energy Applications: Recent Developments and Challenges. *Energies*, 14(15), 4586. <https://doi.org/10.3390/en14154586>

### Conferences' Proceedings

- Samy, O., Otsuji, T., & Moutaouakil, A. E. (2023). Near-Perfect THz Absorber with Wide Range Tunability. *2023 48th International Conference on Infrared, Millimeter, and Terahertz Waves (IRMMW-THz)*, 1–2. <https://doi.org/10.1109/IRMMW-THz57677.2023.10298957>
- Samy, O., Otsuji, T., & El Moutaouakil, A. (2023). Terahertz Absorptance in MoS<sub>2</sub>/Graphene Nanoribbon Heterostructures. *2023 Photonics & Electromagnetics Research Symposium (PIERS)*, 2031–2036. <https://doi.org/10.1109/PIERS59004.2023.10221462>
- Samy, O., Birowosuto, D., & El Moutaouakil, A. (2021). A short review on Molybdenum disulfide (MoS<sub>2</sub>) applications and challenges. *2021 6th International Conference on Renewable Energy: Generation and Applications (ICREGA)*, 220–222. <https://doi.org/10.1109/ICREGA50506.2021.9388220>
- Samy, O., & El Moutaouakil. Comparing the plasmon dispersion in graphene and MoS<sub>2</sub> nanoribbons array under electromagnetic excitation. *Sharjah International Conference on Physics of Advanced materials (SICPAM)*, 25-27 April 2023

## Appendix

*Detailed derivation of the refractive index  $n$  from permittivity  $\epsilon(\omega)$*

$$\tilde{n}(\omega) = \sqrt{\epsilon(\omega)} \quad (1)$$

$$\tilde{n}^2(\omega) = \epsilon_r(\omega) + i\epsilon_i(\omega) \quad (2)$$

$$(n(\omega) + i\kappa(\omega))^2 = \epsilon_r(\omega) + i\epsilon_i(\omega) \quad (3)$$

$$n^2(\omega) - \kappa^2(\omega) + i2n(\omega)\kappa(\omega) = \epsilon_r(\omega) + i\epsilon_i(\omega) \quad (4)$$

Equating the real and imaginary parts in (4) we get (5) and (6)

$$\epsilon_r = n^2(\omega) - \kappa^2(\omega) \quad (5)$$

$$\epsilon_i = 2n(\omega)\kappa(\omega) \rightarrow \kappa(\omega) = \frac{\epsilon_i(\omega)}{2n(\omega)} \quad (6)$$

Substituting (6) in (5) to solve for  $n(\omega)$  as a function of permittivity

$$\epsilon_r(\omega) = n^2(\omega) - \left(\frac{\epsilon_i(\omega)}{2n(\omega)}\right)^2 \quad (7)$$

$$4n^2\epsilon_r(\omega) = 4n^4(\omega) - \epsilon_i^2(\omega) \rightarrow 4n^4(\omega) - 4n^2\epsilon_r(\omega) - \epsilon_i^2(\omega) \quad (8)$$

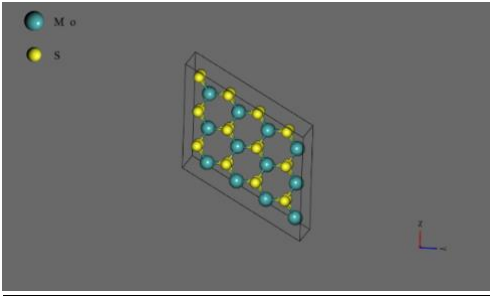
$$n(\omega) = \frac{(4\epsilon_r(\omega) \pm \sqrt{16\epsilon_r^2(\omega) + 16\epsilon_i^2(\omega)})}{8} = \frac{\epsilon_r(\omega)}{2} \pm \frac{1}{2}\sqrt{\epsilon_r^2(\omega) + \epsilon_i^2(\omega)} \quad (9)$$

*The effect of applying vertical electric field on the band gap of monolayer MoS<sub>2</sub>*

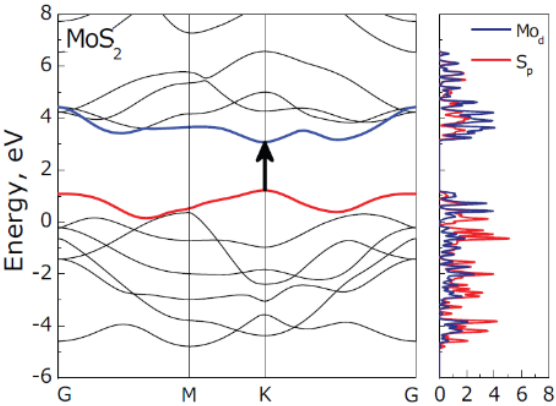
The effect of applying vertical electric field on monolayer MoS<sub>2</sub> was checked using Quantum Espresso. There is a noticeable decrease in the band gap when applying 1 V/Å which is equivalent to 6.5 V for a monolayer of thickness 0.65 nm. And the band gap vanishes at 10 V/Å (65 V). Since we are applying very small voltages compared to these ones the change in band gap will be very small and it will not affect the band gap and so inter-band transitions doesn't exist. That emphasizes the role of intra-band transitions and the correctness of the Drude model in our case. The calculation was done using Burai a graphical user interface for quantum espresso based on density functional theory (DFT) and with a structure of 48 atoms as in Figure 1.Aa. The band gap

calculations in Figure 1.Ac showed an identical band gap structure with that proposed in (Gusakova et al., 2017) Figure 1Ab that used DFT with local density approximation (LDA) and generalized gradient approximation (GGA). The study showed a band gap for MoS<sub>2</sub> of 1.88 eV, while the one in our structure is 1.65 eV which is quite near. Figure 1Ad shows a decrease in the band gap to 1.02 eV when increasing the applied voltage to 1V/Å with slight variation in the conduction band structure (bands are getting nearer at some positions) that may facilitate the intra-band transitions. This is also similar to the band gap calculations of bilayer MoS<sub>2</sub> in (Liu et al., 2012).

(a)



(b)



(c)

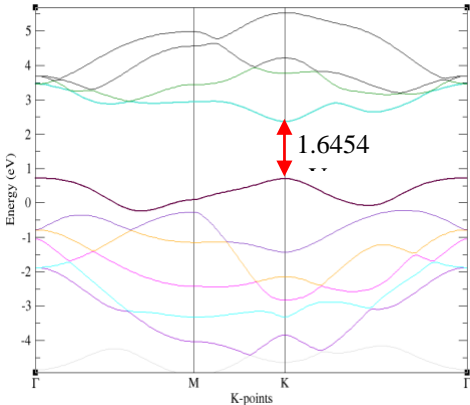


Figure A.1: The effect of adding vertical electric field on monolayer MoS<sub>2</sub>: (a) The MoS<sub>2</sub> structure used; (b) The band gap structure as proposed by (Gusakova et al., 2017) (c) The band gap structure at no applied vertical electric field; (d), (e) the band gap structure at 1 V/Å; (c) at 10 V/Å



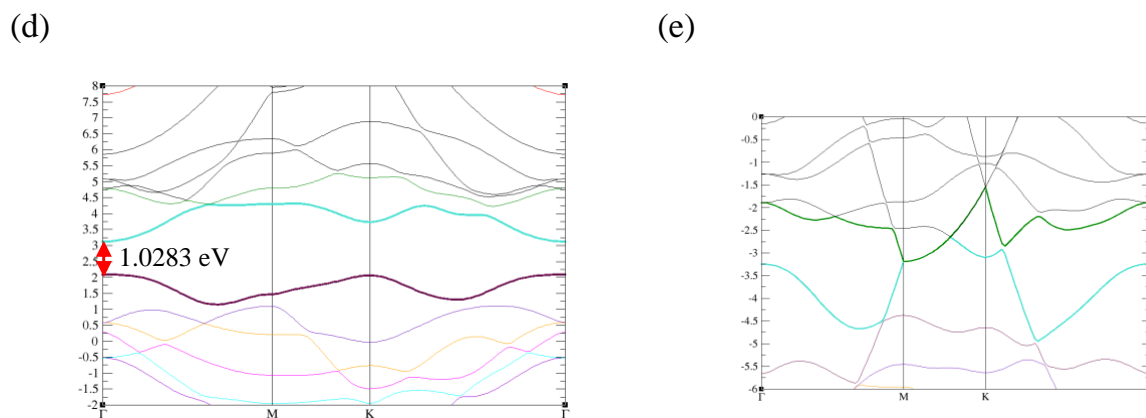


Figure A.1 (continued): The effect of adding vertical electric field on monolayer MoS<sub>2</sub>: (a) The MoS<sub>2</sub> structure used; (b) The band gap structure as proposed by (Gusakova et al., 2017) (c) The band gap structure at no applied vertical electric field; (d), (e) the band gap structure at 1 V/Å; (c) at 10 V/Å

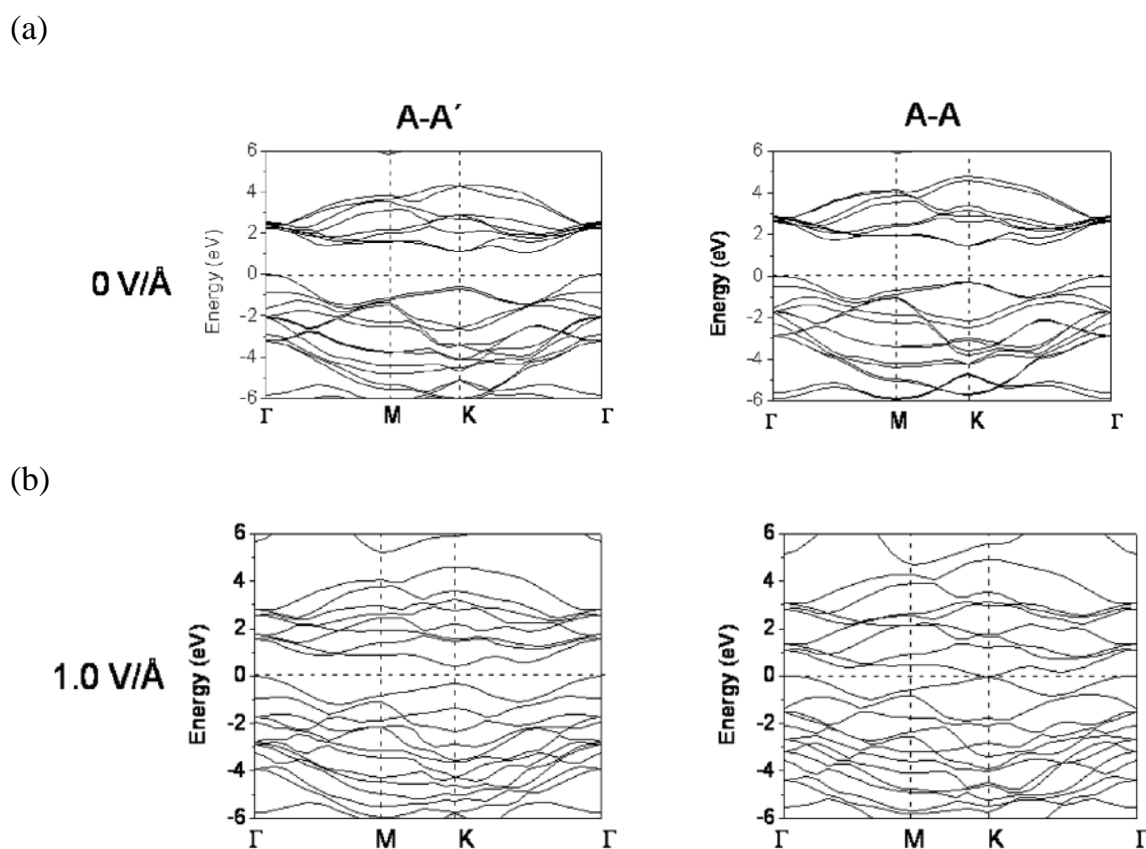


Figure A.2: Band gap structure for bilayer MoS<sub>2</sub> for A-A' and A-A stacking: (a) At 0 V/Å (b) 1 V/Å (c) Electron density (isovalue, 0.1 au) at the Γ point of the valence band under vertical electric field of 0 V/Å (Liu et al., 2012). Reproduced with permission. Journal of physical chemistry, ACS 2012.

(c)

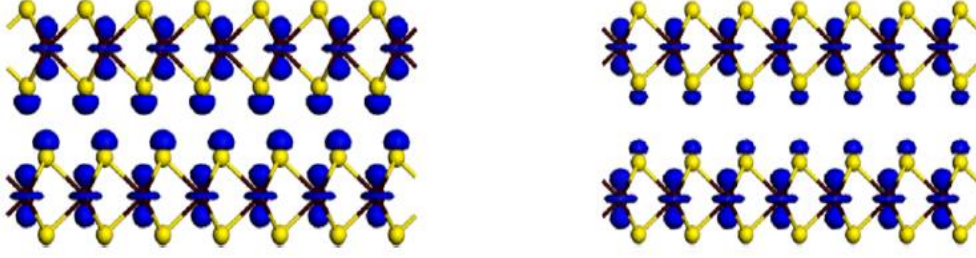


Figure A.2 (continued): Band gap structure for bilayer MoS<sub>2</sub> for A-A' and A-A stacking: (a) At 0 V/Å (b) 1 V/Å (c) Electron density (isovalue, 0.1 au) at the  $\Gamma$  point of the valence band under vertical electric field of 0 V/Å (Liu et al., 2012). Reproduced with permission. Journal of physical chemistry, ACS 2012.

#### *Comparing the dispersion frequency of MoS<sub>2</sub> and graphene nanoribbons*

The plasmon dispersion of MoS<sub>2</sub> and graphene nanoribbons is compared according to the work in (Popov et al., 2010a), where vertical incident wave is used to excite the nanoribbons with an angle  $\theta$  between the normal to the nanoribbon's plane and the nanoribbons. The dispersion frequency is defined according to

$$\omega = \sqrt{2\pi \frac{\vec{k} q^2 N_{2D}}{\epsilon m^*} \cos^2 \theta - \frac{v^2}{4} - \frac{iv}{2}}$$

Where  $N_{2D}$  is the 2D electron concentration,  $v$  is the electron relaxation rate, and  $m^*$  is the electron effective mass. For graphene  $N_{2D} = 10^{12} \text{cm}^{-2}$  and  $v = 1.32 \times 10^{13} \text{s}^{-1}$  and  $m^* = 0.002 \times m_e$  where  $m_e$  is the electronic mass taken as  $9.1 \times 10^{-31}$  and for MoS<sub>2</sub>,  $N_{2D} = 2.5 \times 10^{13} \text{cm}^{-2}$  as n-doped,  $v = 5.88 \times 10^{12} \text{s}^{-1}$  and  $m^* = 0.53m_o$  (Reshetnyak et al., 2018),  $q$  is the electronic charge. The external wave has a propagation vector  $\vec{k}$  and an angle  $\theta$  between the nanoribbon array direction and the wave vector  $\vec{k}$ . The plasmon dispersion of MoS<sub>2</sub> nanoribbons is very low compared to graphene even at high carrier concentrations  $N_{2D} = 2.5 \times 10^{13} \text{cm}^{-2}$  (n-doped). This assures the transmission property of MoS<sub>2</sub> in the THz range.

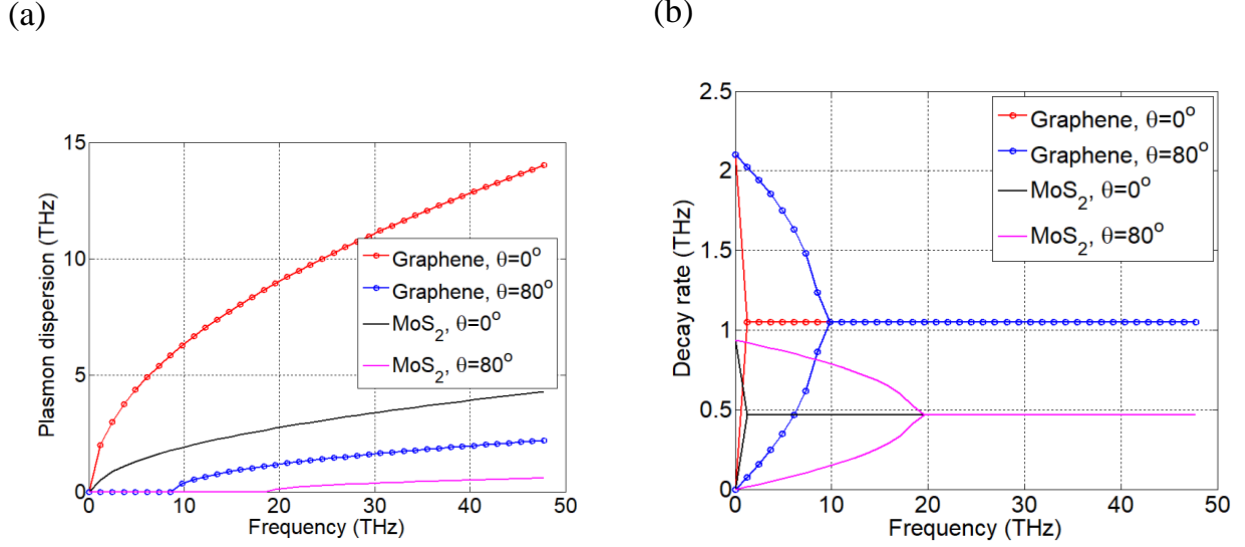


Figure A.3: Comparison between graphene (circle markers) and MoS<sub>2</sub> (solid lines); (a) Plasmon dispersion; (b) decay rate. For MoS<sub>2</sub>  $v = 5.88235 \times 10^{12} \text{ s}^{-1}$ ,  $m^* = 0.53 \times m_0$ ,  $N_{2D} = 2.5 \times 10^{13} \text{ cm}^{-2}$ , for graphene  $v = 1.32 \times 10^{13} \text{ s}^{-1}$ ,  $m^* = 0.002 \times m_0$ ,  $N_{2D} = 10^{12} \text{ cm}^{-2}$  (Popov et al., 2010b; Reshetnyak et al., 2018)

*Calculating the resistance and capacitance of the RLC circuit of graphene from optical conductivity*

The intra-band and inter-band transitions in Equations (2.26) and (2.27) can be re-represented in real and imaginary parts as (3), and (6) where

$$\sigma_{intra}(\omega) = \frac{iq^2A}{\pi\hbar^2(\omega + i\tau^{-1})} \quad (1)$$

Where A is defined as (2)

$$A = \mu_c + 2K_B T \times \ln\left(e^{-\frac{\mu_c}{K_B T}} + 1\right) \quad (2)$$

multiplying (1) by its conjugate we have  $\sigma_{intra}(\omega)$  as real and imaginary parts

$$\sigma_{intra}(\omega) = \frac{q^2 A \tau}{\pi\hbar^2(\omega^2 \tau^2 + 1)} + i \frac{\omega q^2 A \tau^2}{\pi\hbar^2(\omega^2 \tau^2 + 1)} \quad (3)$$

$\sigma_{inter}$  can be represented as

$$\sigma_{inter}(\omega) = i \frac{q^2}{4\pi\hbar} \times \ln(a + ib) \quad (4)$$

Where a, and b are

$$a = \frac{(2|\mu_c|\tau)^2 - (\hbar\omega\tau)^2 - \hbar^2}{\tau^2(2|\mu_c| + \hbar\omega)^2 + \hbar^2}, \quad b = \frac{-4|\mu_c|\tau\hbar}{\tau^2(2|\mu_c| + \hbar\omega)^2 + \hbar^2} \quad (5)$$

The equation in (4) can be represented as

$$\begin{aligned} \sigma_{inter}(\omega) &= i \frac{q^2}{4\pi\hbar} * \left( \frac{1}{2} \ln(a^2 + b^2) + i \tan^{-1} \left( \frac{b}{a} \right) \right) \\ &= -\frac{q^2}{4\pi\hbar} \tan^{-1} \left( \frac{b}{a} \right) + i \frac{q^2}{8\pi\hbar} \ln(a^2 + b^2) \end{aligned} \quad (6)$$

The total conductivity of graphene  $\sigma_{total}(\omega)$  is then represented in real and imaginary parts as

$$\begin{aligned} \sigma_{total} &= \frac{q^2 A \tau}{\pi \hbar^2 (\omega^2 \tau^2 + 1)} - \frac{q^2}{4\pi\hbar} \tan^{-1} \left( \frac{b}{a} \right) \\ &+ i \left( \frac{\omega q^2 A \tau^2}{\pi \hbar^2 (\omega^2 \tau^2 + 1)} + \frac{q^2}{8\pi\hbar} \ln(a^2 + b^2) \right) \end{aligned} \quad (7)$$

$$\begin{aligned} \sigma_{total} &= \frac{8q^2 A \tau - 2q^2 \hbar (\omega^2 \tau^2 + 1) \tan^{-1} \left( \frac{b}{a} \right)}{8\pi \hbar^2 (\omega^2 \tau^2 + 1)} \\ &+ \frac{i(8\omega q^2 A \tau^2 + q^2 \hbar (\omega^2 \tau^2 + 1) \ln(a^2 + b^2))}{8\pi \hbar^2 (\omega^2 \tau^2 + 1)} \end{aligned} \quad (8)$$

The inverse of the conductivity  $\sigma_{total}^{-1}$  is as follows:

$$\sigma_{total}^{-1} = \frac{8\pi \hbar^2 (\omega^2 \tau^2 + 1)}{X + iY} \quad (9)$$

Where X and Y are defined as:

$$X = 8q^2 A \tau - 2q^2 \hbar (\omega^2 \tau^2 + 1) \times \tan^{-1} \left( \frac{b}{a} \right) \quad (10)$$

$$Y = 8\omega q^2 A \tau^2 + q^2 \hbar (\omega^2 \tau^2 + 1) \times \ln(a^2 + b^2) \quad (11)$$

The real and imaginary parts of  $\sigma_{total}^{-1}$  are then calculated as follows:

$$Re\{\sigma_{tot}^{-1}\} = \frac{8\pi \hbar^2 (\omega^2 \tau^2 + 1) \times \left( 8q^2 A \tau - 2q^2 \hbar (\omega^2 \tau^2 + 1) \tan^{-1} \left( \frac{b}{a} \right) \right)}{X^2 + Y^2} \quad (12)$$

$$Im\{\sigma_{tot}^{-1}\} = -\frac{8\pi \hbar^2 (\omega^2 \tau^2 + 1) \times (8\omega q^2 A \tau^2 + q^2 \hbar (\omega^2 \tau^2 + 1) \ln(a^2 + b^2))}{X^2 + Y^2} \quad (13)$$

UAEU

جامعة الإمارات العربية المتحدة  
United Arab Emirates University



## UAEU DOCTORATE DISSERTATION NO. 2024: 28

THz technology is a promising technology that is going to completely change our lives, starting from the high speed and resolution communications through our daily life to the most sophisticated electronics. This thesis proposes suitable electronic and optical structures and materials that can catch up with this technology.

**Omnia Darwish** received her PhD in Electrical Engineering from the Department of Electrical and Communication Engineering, College of Engineering at UAEU, UAE. She received her Master of Science in Engineering from the College of Engineering, Ain Shams University, Egypt.

[www.uaeu.ac.ae](http://www.uaeu.ac.ae)

Online publication of dissertation:  
<https://scholarworks.uaeu.ac.ae/etds/>

UAEU عمادة المكتبات  
Libraries Deanship

جامعة الإمارات العربية المتحدة  
United Arab Emirates University

